High Fidelity Quantum Networking of Trapped Atomic Ions

by

Sagnik Saha

Department of Physics
Duke University

Defense Date: July 15, 2025

Approved:

Christopher Monroe, Supervisor

Kenneth Brown

Marko Cetina

Iman Marvian

David Smith

Dissertation submitted in partial fulfillment of the requirements for the degree of
Doctor of Philosophy in the Department of Physics
in the Graduate School of Duke University
2025

Abstract

High Fidelity Quantum Networking of Trapped Atomic Ions

by

Sagnik Saha

Department of Physics
Duke University

Defense Date: July 15, 2025

Approved:

Christopher Monroe, Supervisor

Kenneth Brown

Marko Cetina

Iman Marvian

David Smith

An abstract of a dissertation submitted in partial fulfillment of the requirements for the degree of Doctor of Philosophy in the Department of Physics in the Graduate School of Duke University
2025

Abstract

Trapped-ion processors constitute a leading platform for quantum computing and quantum networking because of qubits that exhibit exceptional coherence and high-fidelity logic. Scaling these systems to larger registers, however, remains non-trivial. A scalable architecture can be realized by linking smaller computing modules with photonic interconnects, forming a modular network that is agnostic to the underlying hardware design. In an earlier work, we remotely heralded ion–ion entanglement at 250 s^{-1} using the photon's polarization degree of freedom. This was the fastest entanglement rate in two quantum memories mediated by photons [1]. However, uncontrolled birefringence in optical elements imposed fidelity limits on the entangled states.

Here we replace polarization with time-bin encoding, where we distribute entanglement via time-binned photons that are immune to polarization rotations. This strategy enables heralding of Bell states with a fidelity of 97%, the highest reported for photon-mediated ion-ion entanglement. During these experiments, we identified and quantitatively characterized an unexpected decoherence channel arising from recoil of the emitting ion, marking the first direct observation of this effect. Finally, we generalize this protocol by using higher-dimensional time-bin photons to distribute entanglement across the levels of an atomic qudit.

Dedication

To my grandparents, Biswanath Mondal and Parul Rani Mondal.

Contents

Abstract iv

List of Tables ix

List of Figures x

Acknowledgements xiii

1 Thesis Outline 1

1.1 Thesis Outline 1

2 Introduction 4

2.1 Applications and the Promise of Quantum Advantage 6

2.1.1 The Qubit 6

2.1.2 Quantum Gates 8

2.1.3 Quantum Simulation 8

2.1.4 Quantum Algorithms 10

2.2 A Proposed Path Forward: Scaling with Atoms and Photons 10

3 The Qubit: Ions 13

3.1 Atoms as good qubits 15

3.1.1 The barium qubit 17

3.1.2 The ytterbium qubit 21

3.1.3 Possible encoding of states in an ion 22

3.2 Photonic qubit 23

3.2.1 Possible encoding of states in a photon 26

4 Qubit Confinement: Ion Trapping 28

4.1 Ion Trap Construction 35

4.2 Ion Loading 40

5 Qubit Control: Atom Light Interaction 44
5.1 System Hamiltonian 44
5.2 Dipole coupling 50
5.2.1 Applications: Doppler Cooling 54
5.2.2 Applications: Optical Pumping 57
5.3 Quadrupole Transitions 58
5.3.1 Applications: Single optical qubit gates 63
5.3.2 Applications: Resolving sidebands 65
5.3.3 Applications: State detection by electron shelving 69
5.4 Two photon Raman coupling 70
6 Remote entanglement of trapped atomic ions 72
6.1 Polarization encoding: The Good and the Bad 75
6.1.1 Entanglement rate: The Good 79
6.1.2 Entanglement fidelity: The Bad 81
7 Time-bin mediated remote entanglement 87
7.1 Atomic level structure for time-bins 88
7.2 Entanglement protocol 90
7.3 Entangled phase state stability 94
7.4 Experimental parameters 102
7.4.1 1762 nm laser system 103
7.4.2 493 nm pulsed laser system 103
7.5 Experimental results 104
7.5.1 Correction of Erasure Errors 108
7.5.2 Entanglement rate calculation 109
7.5.3 Error budget 110

7.6 Discussion . . . 111
7.6.1 Optimizing Rate and Fidelity . . . 112
8 Higher dimensional quantum networking of atoms 114
8.1 The Atom-Photon Interface: Creating a Flying Qudit . . . 116
8.1.1 Qudit Levels . . . 116
8.1.2 Qudit-HD photon entanglement . . . 117
8.2 Networking Qudit Memories . . . 121
8.2.1 The Experimental Setup and Protocol . . . 121
8.2.2 Entanglement results . . . 124
8.2.3 Experimental error sources . . . 129
8.2.4 Entanglement Rate and the Trade-off of Higher Dimensions Rate and Success Probability . . . 134
8.3 Outlook . . . 138
9 Conclusion 139
9.1 Improving Fidelity: Frequency-Mediated Entanglement . . . 140
9.2 Improving Rate: Cavity-Enhanced Repeater Nodes . . . 141
9.3 Future Work: GHZ State Preparation . . . 142
Bibliography 144

List of Tables

3.1 S to P transition wavelengths 17

3.2 Zeeman splittings for barium 19

4.1 Oven angles for different chambers 43

6.1 Heralding click pattern 78

7.1 Measured harmonic motional frequencies 101

7.2 Source of error for time-bin 111

8.1 Photon collection and detection efficiencies 121

8.2 Qudit state results 127

8.3 Bell state phase sensitivities 130

8.4 Error budget. 134

8.5 Qudit entanglement rates 137

List of Figures

2.1 Bloch sphere representation of a qubit 7

3.1 Ion trap periodic table 18

3.2 Energy level diagram of $^{138}Ba^{+}$ 20

3.3 Energy level diagram of $^{171}Yb^{+}$ 22

3.4 Wavelength dependence of fiber attenuation 24

4.1 Oscillating Paul trap potential 29

4.2 Electrode configuration for ion trapping 30

4.3 Atomic ion position in a trap 33

4.4 4-rod trap dimensions 36

4.5 Electrochemical etching setup 37

4.6 Cleo trap needle 37

4.7 Trap construction 38

5.1 Barium dipole transitions 53

5.2 Optical pumping 58

5.3 Optical pumping in $^{138}Ba^{+}$ 59

5.4 Definition of angles for quadrupole transition 61

5.5 Quadrupole transition strengths 62

5.6 Quadrupole transitions of $^{138}Ba^{+}$ 63

5.7 Rabi oscillations 65

5.8 Sideband transitions with 1762 nm light 66

5.9 Raman based 1Q gates 71

6.1 Polarization encoding 76

6.2 Cleo experimental setup 77

6.3 Atom photon fidelity measurements 79

6.4 Entanglement state fidelity analysis 83
6.5 Window birefringence measurement 85
7.1 Energy levels in $^{138}Ba^{+}$ 89
7.2 Levels for time-bin photon generation 90
7.3 Time bin experimental setup 91
7.4 Time bin experimental protocol 92
7.5 State detection histogram 93
7.6 Histogram of arrival times 94
7.7 Parity scan for time bin experiment 105
7.8 Time bin fidelity with varying excitation times 106
7.9 Effect of spontaneous emission on fidelity 107
7.10 Differential qubit coherence 108
7.11 Erasure levels 109
8.1 Representative diagram of quantum memory 115
8.2 Scheme for qudit-photon entanglement generation 117
8.3 Qudit time-bin generation 118
8.4 High dimensional photons in time 120
8.5 Qudit remote entanglement diagram 122
8.6 Qudit state analysis pulse sequence 124
8.7 Qudit entangled state analysis 126
8.8 Qudit states after heralding 128
8.9 Qudit states after analysis pulse 129
8.10 Differential magnetic field drift and phase feed-forward 131
8.11 Bell-state measurement (BSM) success fractions 135
8.12 Qudit entanglement rates and total entanglement success probabilities 137

9.1 Level diagram of $^{133}Ba^{+}$ 140
9.2 Setup for GHZ state generation 142

Acknowledgements

This thesis marks the culmination of an intense and rewarding journey, and it would not have been possible without the support, guidance, and encouragement of many individuals to whom I owe my sincerest gratitude.

First and foremost, I would like to thank my advisor, Prof. Christopher Monroe. When I first met him at the University of Maryland, I had little experience with ion traps or lasers. Despite this, he welcomed me into his group and entrusted me with one of the more hardware-intensive experiments—a gesture for which I remain deeply grateful. Much of what I know about ion trapping and quantum computing I have learned under his guidance. Beyond technical knowledge, one of the most valuable lessons I have taken from Chris is the importance of taking bold risks. I've often heard him say, "We're young—we should be taking risks," and that mindset has shaped how I approach both science and life.

I am also thankful to my committee members, Prof. Kenneth Brown, Prof. Marko Cetina, Prof. Iman Marvian, and Prof. David Smith, for their time, and guidance throughout my graduate career. I am grateful to Marko from whom I have learned not only a lot of physics but also world and Serbian history as well as global geopolitics.

To my lab-mates, past and present, George, Isabella, Ashish, Misha, Harriet, Jameson, Allison, and many others, thank you for creating a collaborative and socially cohesive group. Whether it was debugging a setup at midnight, sharing coffee-fueled discussions, or celebrating small experimental wins (at various restaurants), your camaraderie made this journey not only possible but joyful. A special thanks to George, whose mentorship during my early years in the lab was invaluable and whose approach to experiments I have tried to emulate. I also want to thank Isabella, Debo, Jameson, Arinjoy and many others at the Duke Quantum Center whose com-

panionship I have greatly enjoyed.

Outside the lab, I am grateful to the friends who kept me grounded. To my fellow graduate students at Duke, thank you for your companionship, conversations and for being a reminder that no one walks this path alone. To my close friends from college and high school, thank you for reminding me of who I was before I became a physicist and supporting who I am becoming now.

To my family, I owe more than I can put into words. To my parents and grandparents, thank you for your belief in me, your sacrifices, and your constant encouragement.

Lastly, to my girlfriend, Anvita, thank you for being a constant source of love, patience, and understanding. Your support has been my anchor through the many highs and lows of this journey, and I am grateful for your presence in my life.

This thesis is as much a product of the people who supported me as it is of my own effort. To all of you, thank you.

1

Thesis Outline

This thesis is organized to follow the progression of ideas and experiments that led to the results presented here. It begins with an overview of quantum computing and the motivation for using atomic ions as qubits. The following chapters cover how we trap and control these ions, how we use light to manipulate them, and how we generate entanglement between distant ions using photons. The final chapters focus on our work with time-bin–encoded photons and how we use high-dimensional entangled states to herald entanglement. A brief outline of each chapter is given below.

1.1 Thesis Outline

1. Introduction: This chapter introduces the foundations of quantum computing, including its historical context, key algorithmic breakthroughs, and various physical platforms under exploration. It discusses the resource requirements for quantum advantage and motivates the use of atomic systems as a scalable platform. The chapter concludes by introducing photonic interconnects as a pathway toward scaling atomic qubit systems to the utility level.
2. The Qubit: Ions This chapter motivates the use of atomic ions as qubits and compares different encoding schemes in both atomic and photonic systems. It highlights the complementary roles of atoms (as memory and processing units) and photons (as communication carriers), and explores how atom–photon in-

terfaces form the basis for implementing photonic interconnects.

3. Qubit Confinement: Ion Trapping This chapter covers the principles of ion trapping, focusing on radiofrequency (Paul) traps. It describes the design, implementation, and operational parameters of the linear four-rod traps used in this work and discusses practical aspects such as ion loading, and micromotion minimization.
4. Qubit Control: Light-atom interaction This chapter presents the methods for coherent and dissipative control of trapped-ion qubits through light–matter interactions. It focuses on laser-based techniques required for state preparation, manipulation, and readout.
5. Remote entanglement of trapped atomic ions: This chapter details remote entanglement protocols and their relevance to scalable quantum computing. It reviews our past work on polarization-based entanglement schemes and highlights some of it's drawbacks.
6. Time-bin mediated remote entanglement: This chapter presents time-bin encoding as an alternative to polarization encoding. It covers the theory behind time-bin schemes, describes the experimental setup in detail, and reports results—including the highest heralded-entanglement fidelity achieved to date.
7. Higher dimensional quantum networking of atoms: This chapter describes the extension of time-bin encoding to higher-dimensional entangled states. It presents our protocol for heralding bipartite entanglement in a larger Hilbert space and discusses how this approach can surpass the traditional Bell-state heralding limit of 1/2. Experimental methods and implications for quantum networking are also discussed.
8. Conclusion: The final chapter looks ahead to future directions. We briefly discuss an upcoming experiment in our lab to generate a three-node GHZ state using photonic links, which would be a step towards building small quantum

networks. We also consider other possible approaches to improve the fidelity and rate of remote entanglement, with the goal of developing better photonic connections for scalable, networked quantum computing.

2

Introduction

The theory of computation, due to the foundational work of Alan Turing and Alonzo Church, has traditionally been built on deterministic and discrete logic [2, 3]. A bit, the fundamental unit of information, exists in one of two definite states: 0 or 1. Classical computing has powered a technological revolution, leading to supercomputers of today that can perform trillions of operations per second. Interestingly, the underlying transistors that power these computers are based on quantum mechanical effects [4].

Whereas classical mechanics and conventional intuition are, in some sense, based on the notion of deterministic evolution, the laws of quantum mechanics are described by the precise evolution of probabilities. Quantum mechanics allows, somewhat nonintuitive phenomena such as superposition, interference, and entanglement [5, 6]. This leads to the question: Could a new type of computation, one that directly harnesses these quantum phenomena, solve problems which are otherwise intractable?

The most influential early proposal came from the physicist Richard Feynman. In a seminal 1982 paper, "Simulating Physics with Computers," Feynman observed that simulating a quantum system with a classical computer appeared to be an exponentially difficult task [7]. The number of variables required to describe a system of N interacting quantum particles grows as 2^N, a computational cost that quickly becomes prohibitive. He argued that to simulate a quantum system efficiently, one should build a computer that itself operates on quantum mechanical principles.

Independently and slightly earlier, in 1980, the mathematician Yuri Manin had outlined a similar idea in his book “Computable and Uncomputable” [8]. Manin was one of the first to suggest the use of quantum systems for computation and to speculate on their potential advantages over classical machines. Both Manin and Feynman independently came to the conclusion that as quantum systems grow in size, they quickly become intractable under classical simulation techniques. The concept of a quantum computer did not emerge from a single breakthrough but was a gradual realization by physicists.

In the early 1980s, these ideas began to solidify into a concrete theory of quantum computation over the following decade. In 1985, David Deutsch at the University of Oxford published a pivotal paper that formally defined a universal quantum computer, or a "quantum Turing machine" [9]. He proved that such a machine could efficiently simulate any other physical system, thereby establishing the theoretical bedrock for the entire field. The field of quantum computing gained a lot of interest in 1994. Peter Shor, from Bell Labs, had developed a quantum algorithm capable of finding the prime factors of a large integer exponentially faster than any known classical algorithm [10]. The security of modern cryptography, including the widely used RSA encryption standard, relies on the classical difficulty of this exact problem. Shor’s algorithm demonstrated that a functional quantum computer could, in principle, break much of the world’s current digital security infrastructure.

This was the first “killer application” for a quantum computer. The focus of the field rapidly shifted from purely theoretical explorations to experiments: how could one actually build such a device? One step towards this came in 1995 when Ignacio Cirac and Peter Zoller proposed a physical implementation. Their scheme detailed how a set of trapped ions, cooled to near absolute zero and manipulated by lasers, could realize a fundamental two-qubit quantum logic gate (the controlled-NOT gate) [11]. Immediately following this, David Wineland and Chris Monroe from

NIST demonstrated the first implementation of a two-qubit gate based on trapped ions [12].

Since then, a variety of platforms have been demonstrated as suitable for quantum computing. This includes the phase, charge, flux, or some combination of them in superconducting circuits [13, 14], spin states of neutral atoms held in optical tweezers [15–17], spin states in quantum dots [18–20], photonic states in an integrated photonic chip [21, 22], anyonic excitations in topological states of matter [23], and of course electronic spin states of trapped atomic ions [24, 25].

2.1 Applications and the Promise of Quantum Advantage

Quantum computing may provide "quantum advantage" i.e. speedup over classical computers for certain classes of problems. These problems are typically those whose complexity scales exponentially with size, rendering them intractable for classical machines. Before we look at some use cases, we quickly go over how a qubit and operations on it are defined.

2.1.1 The Qubit

In quantum computing, the classical bit is replaced by the quantum bit, or qubit. A qubit is a two-level quantum mechanical system which can exist in a superposition of both the two states or levels [26]. We can represent the state of a qubit $|\psi\rangle$ using Dirac notation:

$$|\psi\rangle = \alpha|0\rangle + \beta|1\rangle$$

Here, $|0\rangle$ and $|1\rangle$ are the basis states (analogous to classical 0 and 1), and α and β are complex numbers called probability amplitudes. The condition $|\alpha|^2 + |\beta|^2 = 1$ must be met, where $|\alpha|^2$ is the probability of finding the qubit in the state $|0\rangle$ upon measurement, and $|\beta|^2$ is the probability of finding it in the state $|1\rangle$. One can also represent the qubit as a point on a unit complex sphere 2.1. A pure, normalized

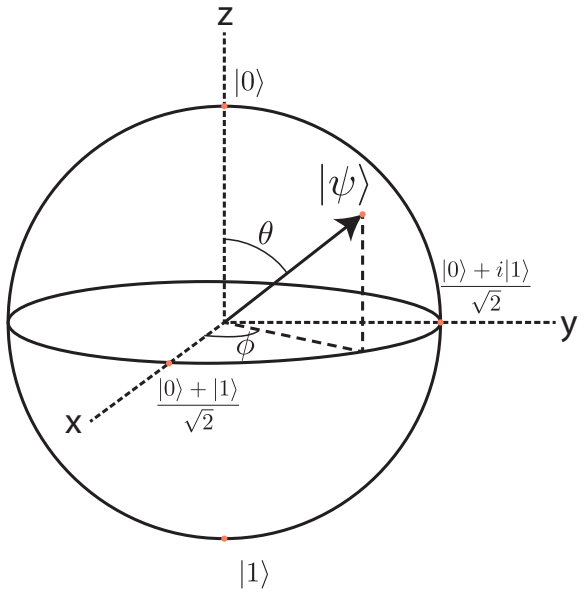

FIGURE 2.1: Bloch sphere representation of a single qubit. A general qubit state can be written as $|\psi\rangle = \cos(\theta/2)\,|0\rangle + e^{i\phi}\sin(\theta/2)\,|1\rangle$, corresponding to a point on the unit sphere. The north and south poles represent the computational basis states $|0\rangle$ and $|1\rangle$, respectively, while the equator consists of equal superpositions with varying phase.

state of the qubit can then be parameterized by two angles denoting the point. We can write

$$|\psi\rangle = \cos(\theta/2)\,|0\rangle + e^{i\phi}\sin(\theta/2)\,|1\rangle$$

In an ideal quantum computer, the state angles θ and ϕ evolve predictably under applied quantum gates (see next section), allowing us to track them precisely. Loss of this predictability leads to decoherence, which we quantify by the qubit's T_1 and T_2 times—the timescales over which θ and ϕ remain reliable, respectively. Quantum algorithms then manipulate these angles across many qubits, using interference of their complex amplitudes to maximize the probability of obtaining the desired outcome. Finally, projective measurements collapse each qubit into one of its basis states, destroying its superposition.

2.1.2 Quantum Gates

Quantum algorithms are implemented by applying a sequence of quantum gates to one or more qubits [26]. They can operate on any number of qubits; however, the frequently used ones are single and two-qubit gates.

- Single-Qubit Gates: These manipulate the state of a single qubit, which can be visualized as rotations on the surface of a Bloch sphere. Examples include the X-gate (a bit-flip), the Z-gate (a phase-flip), and the Hadamard (H) gate.
- Two-Qubit Gates: To perform useful computation, qubits must interact. This is achieved through two-qubit gates, which can create entanglement across qubits. An entangled state is one where the quantum state of each qubit is not seperable as a tensor product of each states in their own Hilbert space. The most common two-qubit gate is the Controlled-NOT (CNOT) gate. It flips the state of a target qubit if and only if a control qubit is in the state $|1\rangle$.

A universal set of quantum gates (e.g., arbitrary rotations on the Bloch sphere plus the CNOT gate) is sufficient to construct any possible quantum algorithm.

2.1.3 Quantum Simulation

Returning to Feynman's original motivation, quantum simulation remains one of the most promising applications. Quantum simulation is emerging as a crucial approach for tackling complex quantum many-body problems in quantum chemistry, condensed matter physics, and high-energy physics. Analog quantum simulators (e.g. ultracold atoms in optical lattices, trapped ions, Rydberg atom arrays) currently achieve hundreds of qubits with specific Hamiltonians [27–30], while digital gate-based quantum computers offer universal programmability on tens to low-hundreds of qubits [31–33].

- Quantum chemistry simulation: Current quantum computers are limited in size and noise. So far, only small molecules have been simulated on quantum

hardware; for example, proof-of-concept studies have computed the ground-state energies of H_2, LiH, BeH_2 and H_2O in minimal basis sets [34]. The resource demands for useful chemistry simulations are formidable. For instance, obtaining the exact ground-state energy of the FeMoco enzyme active site (for nitrogen fixation and a benchmark problem beyond classical computing) has been estimated to require on the order of 900 logical qubits with $\sim 10^5$ single qubit rotations and a cricuit depth of $\sim 10^3$ [35]. In practice, depending upon the error correction code, this can translate to hundreds of thousands of qubits with physical error rates $<10^{-3}$.

- Condensed matter physics simulations:Quantum simulation of strongly correlated quantum materials and models is another promising domain – and one where quantum advantage may emerge sooner. Rydberg-atom arrays have realized 2D spin-1/2 Ising models with up to 256 atoms [36], allowing studies of different phase transitions. A plethora of experiments using both analog and digital simulators, have already been used to study condensed matter phenomena [31, 32]. The resource requirements for quantum advantage problems (2d Fermi-Hubbard models for superconductivity), are arguably the lowest among all classes of problems a quantum computer can attack, but still require several hundred thousand qubits (assuming a surface code) with 10^{-3} error rates [37].
- Fundamental Physics: There are ongoing experiments about simulating different aspects of high-energy physics, for example, scattering phenomena, string breaking, quenching etc [29, 38, 39]. Interestingly, it may be possible to show quantum advantage in terms of specific calculations of quantum dynamics with a 100s of qubits and reasonable error rates (several thousand two qubit gates, error $\sim 10^{-4}$) [38].

2.1.4 Quantum Algorithms

Beyond quantum simulation, a suite of quantum algorithms has been developed that offer significant speedups. The most prominent among all of them, till date, is Shor's algorithm.

- Shor's Algorithm: Indisputablely, this has the most impact in the real world, and also shows quantum advantage very clearly. To factor an N bit integer a quantum computer would take $\mathcal{O}(N^3)$ gates with $5N + 1$ qubits [40], assuming perfect qubits with error free gates. Current state of the art resource estimates say that to factor a 2048-bit RSA integer, it would require less than a million noisy qubits, assuming an error rate of 10^{-3} in a superconducing qubit archictecture running surface code [41], or 19 million qubits for a neutral atom system with similar error rates and surface code error correction scheme [42].

From the above numbers, it is very clear that we will need to have qubits at least on the order of $>10^6$, with physical error rates of 10^{-3} or better. Current state of the art quantum computers have qubit counts in the (100s-1000s), with error rates of 10^{-3} [42–44]. Clearly, there is a big gap, and we need to scale up these quantum systems by several orders of magnitudes.

Several physical platforms are being pursued to have a scalable architecture, including superconducting circuits, trapped atomic ions, neutral atoms, silicon quantum dots, and photons.

2.2 A Proposed Path Forward: Scaling with Atoms and Photons

To bridge the gap between current day devices and fault-tolerant quantum computers (>1000 logical qubits), a leading strategy is to pursue a modular architecture. The idea is to build a large-scale processor by networking many smaller, high-performance quantum modules together. This approach breaks down a monolithic engineering challenge into a more manageable one, allowing individual modules to

be built, characterized, and replaced independently. In the case of trapped atomic ions, each module may contain hundreds to thousands of qubits shuttled between multiple zones [25, 45].

The ideal carrier for transmitting quantum information between these modules is the photon. Photons travel at the speed of light, interact weakly with the environment (making them robust against decoherence during transit), and can be routed using existing fiber-optic technologies. Therefore, the development of high-fidelity and fast photonic interconnects between good quantum memories is crucial for large-scale modular quantum computers and networks [46]. Such photonic interconnects collect photons from different qubits and interfere them in an entanglement-swapping procedure [47] that leaves these qubits entangled [48–50].

This thesis focuses on the platform that is best suited to interface with these photonic interconnects: trapped atoms/ions [1, 51–53]. Atomic systems are promising candidates for quantum computing nodes for several reasons:

- Identical Qubits: Every atom of a given isotope is a perfect, identical qubit, eliminating manufacturing variations.
- Long Coherence Times: Atoms in a vacuum are well isolated from environmental noise, leading to some of the longest coherence times of any platform.
- Natural Light-Matter Interface: Most importantly, atoms possess strong natural electronic transitions that allow them to efficiently emit and absorb single photons. This provides a built-in high-fidelity mechanism for converting the stationary qubit state within an atomic module into a "flying" photonic qubit for communication.

By combining the stability and coherence of atomic qubits with the speed and robustness of photons, a modular architecture offers a scalable path toward building a utility-scale quantum computer. The research presented in this thesis aims to address key challenges in the development of such atom-photon interfaces, which

will play a critical role in scaling up quantum computers.

3

The Qubit: Ions

Atoms, once they are isolated from their environment, are ideal qubits, since in quantum mechanics, they are *indistinguishable*. If someone prepares two atoms in the exact same quantum state, then no measurement that the laws of physics permit can reveal which atom is which. Exchanging the particles only multiplies the many-body wavefunction by an overall phase. That uniformity makes atomic hardware fundamentally different from solid-state qubits, whose Josephson junction areas [54], barrier thicknesses [55], or color-center strain's drift from device to device [56, 57] must be individually characterized and taken into consideration while operating them.

We quickly look back at the developments in quantum mechanics that postulate atoms to be *indistinguishable*. John Dalton, in the early nineteenth century, stated that matter is built from discrete, indivisible particles that combine in fixed ratios [58]. Although J. J. Thomson's 1897 discovery of the electron [59] and Ernest Rutherford's 1911 discovery of the nucleus [60] did not go well with Dalton's indivisible atoms, they produced a classical paradox: a charged electron orbiting a nucleus will radiate energy, and fall into the nucleus. Niels Bohr fixed the atomic stability problem by postulating quantized orbits [61], Max Planck explained the black-body spectra [62] and Einstein's photoelectric-effect implied that light can be thought of as particles [63]. Louis de Broglie extended quantization to matter waves [64]; Erwin Schrödinger and Werner Heisenberg then supplied wave mechanics and matrix

mechanics, completing the first quantum revolution [65, 66]. In the 1950s, quantum electrodynamics, the weak interaction theory, and quantum chromodynamics combined into the Standard Model, demonstrating that atoms are actually divisible and made of quarks, leptons, and gauge bosons whose properties depend only on their quantum numbers [67–71]. Consequently, any two atoms of the same isotope (made up in the same way from leptons, quarks and gluons), in identical electronic and motional states, are governed by identical Hamiltonians and respond identically to external control fields.

However, to get to a working quantum computer, we must localize, cool, and address individual atoms with precision. For charged particles, Wolfgang Paul and Hans Dehmelt devised the radio-frequency quadrupole trap—the four-rod "Paul trap" or quadrupole mass filter—for which they shared one-half of the 1989 Nobel Prize in Physics [72]. A single ion can be confined for days, with megahertz motional frequencies, and ion escape rates low enough to permit thousands of logic operations between re-cooling cycles. Neutral atoms can be held in optical potentials created either by crossed laser beams that form three-dimensional optical lattices or by tightly focused beams that act as optical tweezers, pioneered by Arthur Ashkin, Steven Chu, William D. Phillips, and many others [73, 74]. Both atoms and ions can be cooled via various laser cooling techniques [75–77].

In both platforms, narrow-linewidth lasers and microwaves initialize internal states, engineer spin-dependent interactions via state-dependent forces or Rydeberg interactions or phase shifts from cold collisions, and drive Raman or direct transitions that realize single-qubit rotations with errors well below one part in 10^4 [78, 79]. Multiqubit entanglement arises via shared phonon modes in ions or Rydberg-mediated dipole interactions in neutrals, with two qubit entanglement fidelities exceeding 99.5% [80, 81]. Because every qubit is the same and of pristine quality, the workload for scaling a quantum computer, transfers to the control system. Studies

have already shown ways to control a large array of qubits [82, 83]. Moreover, the identical optical transitions that simplify local gates also standardize remote links: photons emitted from independent ions are automatically frequency matched, enabling high-visibility two-photon interference for heralded entanglement across meters or, with cavities and frequency conversion, across kilometers of fiber [1, 53, 84, 85]. The ability to copy-and-paste control recipes across an array of modularly connected qubits while using the same stabilized laser frequencies, microwave tones, and error-mitigation protocols makes atoms the right choice for making fault-tolerant quantum computers. This chapter examines the specific level structures, clock transitions, and metastable manifolds of the atomic ion species central to this thesis—$^{171}Yb^{+}$ and $^{138}Ba^{+}$, and explains how their native properties align with the demands of scalable quantum logic and photonic networking. Subsequent chapters delve into the mechanics of trapping, cooling, coherent manipulation, and interconnects that translate such perfect atoms into operational qubits.

3.1 Atoms as good qubits

Now we go into details about why an atom is a good qubit. An ideal qubit should have the following characteristics:

1. Identical to each other.
2. Long quantum information storage time.
3. Predictable qubit state evolution.
4. High quality and fast quantum state preparation.
5. Easy qubit state discrimination and measurement.
6. Easy, fast and high quality single and two qubit gates.

Atomic systems satisfy these key characteristics for scalable quantum hardware almost by construction. First, atoms of the same isotope are quantum-mechanically indistinguishable: once loaded into a Paul trap or optical tweezer, each qubit experi-

ences almost the same internal Hamiltonian, so device variability is negligible. Second, the qubit can be stored in a pair of hyperfine "clock" states whose energy splitting is first-order insensitive to magnetic-field noise, resulting in minutes of coherence times which can be pushed to hours with magnetic shielding and dynamical decoupling [86]. Third, because the environment is an ultra-high-vacuum chamber (minimizing interactions with the environment) with actively stabilized radio-frequency (resulting in predictable motional evolution) and laser fields, phase evolution follows the lab clock predictably, enabling precise qubit phase tracking [87]. Fourth, optical pumping prepares the ion in a well-defined electronic ground state with $> 99.9\%$ fidelity in a few microseconds, and laser/microwave pulses or stimulated-Raman transfers create arbitrary superpositions just as quickly. Fifth, the same cycling transition used for Doppler cooling can provide state-dependent fluorescence. In a 100–1000 μs detection window the $|0\rangle$ state scatters thousands of photons while the $|1\rangle$ state, either due to being shelved to a long-lived metastable state or being spectrally distant from the detection light, remains nearly silent, allowing single-shot discrimination fidelities above 99.9 % [79, 88]. Single-qubit gates driven by resonant microwaves or narrow-band Raman beams achieve error rates below 10^{-6} in ~ 10 μs [78]. Two-qubit entangling gates exploiting geometric phases which are mediated either by Rydberg or Coulomb interactions can now routinely deliver Bell-state fidelities above 99.5% in 20–1000 μs [80]. Together, these attributes make trapped ions a clean and versatile platform that offers identical qubits, long-lived memories, deterministic state control, high-contrast readout, and fast, high-quality logic operations.

Typically, the trapped ion community uses Group 2 and 2b elements by singly ionizing them. Such an element, after losing an electron, has only a single electron in its S valence shell.

Table 3.1: S to P transition wavelengths for all Group II atomic ions. $^{138}Ba^{+}$ has the longest wavelength among all of them, making it suitable for quantum communication since longer wavelengths have lower fiber attenuation. Data taken from the NIST atomic spectra database [89].

Species	S ↔ P wavelength (nm)
$^{9}Be^{+}$	313
$^{24}Mg^{+}$	280
$^{40}Ca^{+}$	397
$^{88}Sr^{+}$	422
$^{138}Ba^{+}$	493
$^{226}Ra^{+}$	468
$^{171}Yb^{+}$	370

3.1.1 The barium qubit

As seen in Table 3.1, barium-138 has the longest wavelength $S_{1/2}$ to $P_{1/2}$ transition among the Group 2 elements. This is good since visible lasers are easier to maintain and operate than ultraviolet ones. Moreover, longer wavelengths have lower attenuation rates in fiber, can be used with integrated photonics, and can be detected with a greater quantum efficiency. These make barium a good choice for quantum communication. The level structure of singly-ionized barium is shown in Fig. 3.2. The term symbols which characterize the angular momentum state of the atom are written as $^{2S+1}L_J$, where S is spin angular momentum, L is the orbital angular momentum, and J is the total angular momentum given as $|L - S| < J < |L + S|$. Note that these are the momentum states of the single electron bound to the atomic barium nuclei. Since this is the even isotope of barium, it does not have a nuclear spin ($I = 0$) and hence the total spin angular momentum of the system $S = \frac{1}{2}$. For the ground state manifold we will have $S = \frac{1}{2}, L = 0, J = \frac{1}{2}$. The spin multiplicity of the ground state is $2s + 1 = 2$, meaning that under the application of a magnetic field, it splits into two states with good quantum numbers given as $|J, m_J\rangle = |\frac{1}{2}, \pm\frac{1}{2}\rangle$. The energy

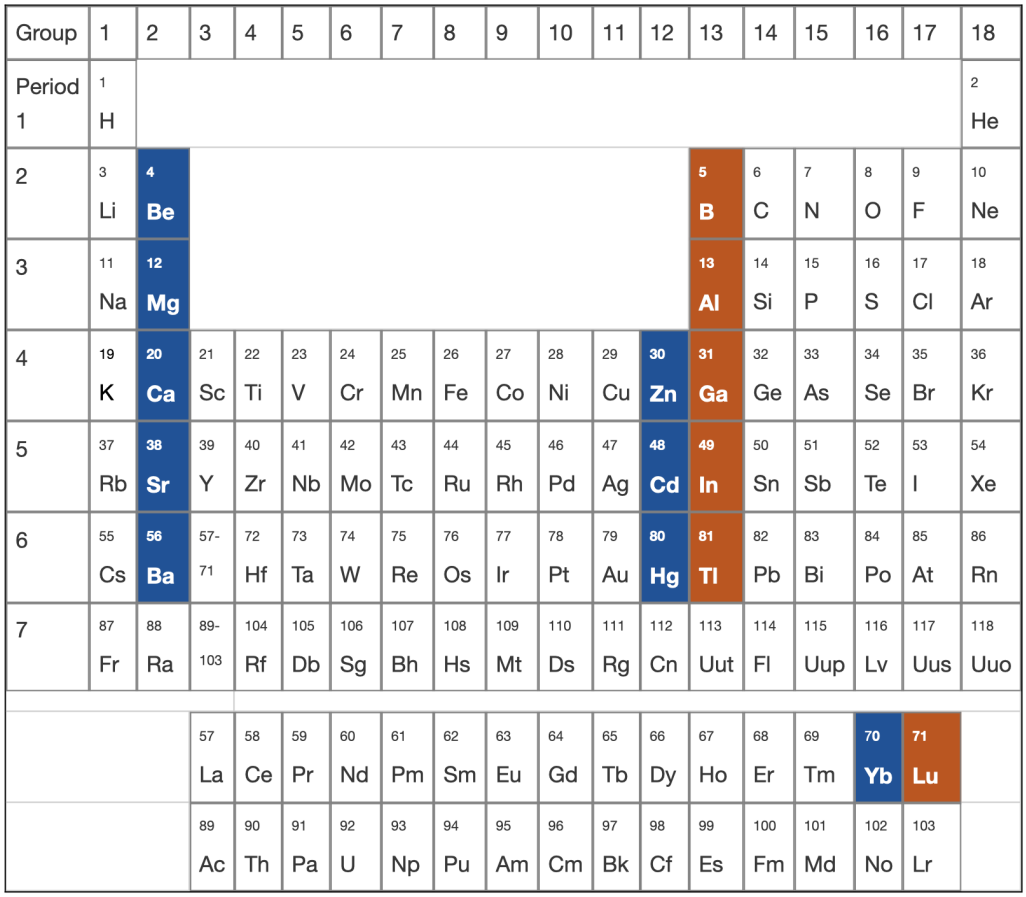

FIGURE 3.1: **Periodic table highlighting the atoms which are typically used in trapped ion experiments.** The blue colors represent alkali-like ions and the orange colors represent alkaline-earth like ions. *Adapted from the Duke Ion Trapping website* [90].

splitting between these two states is given by

$$\Delta E = \Delta m_J \mu_B g_J B \tag{3.1}$$

where

$$g_J = 1 + \frac{J(J+1) - L(L+1) + S(S+1)}{2J(J+1)} = 2 \tag{3.2}$$

and $\mu_B = 9.27 \times 10^{-28} J/G$ is the Bohr Magneton. With these, we get a magnetic field splitting of 2.8 MHz/G between the two states in the ground state. All the other splittings and angular momentum numbers are given in Table 3.2 (assuming

$\Delta m_J = 1$).

Table 3.2: Zeeman splittings for different angular momentum states of barium. g_J is calculated from Eqn. 3.2, and the angular momentum quantum numbers are retrieved from the term symbols. Zeeman splittings are calculated from Eqn. 3.1

Levels	**J**	**L**	**S**	g_J	**Zeeman splitting** MHz/G
$^2S_{1/2}$	1/2	0	1/2	2.00	2.799
$^2P_{1/2}$	1/2	1	1/2	0.67	0.933
$^2P_{3/2}$	3/2	1	1/2	1.33	1.866
$^2D_{3/2}$	3/2	2	1/2	0.80	1.119
$^2D_{5/2}$	5/2	2	1/2	1.20	1.679

The ground state couples to the excited $^2P_{1/2}$ state via a 493 nm dipole transition. This state has a lifetime of 7.9 ns, decaying to both the S level and a low lying D (J=3/2) level via dipole coupling [91]. To pump out of the $D_{3/2}$ levels, one needs to use 650 nm light. There also exists a long-lived D level (J=5/2, $\tau = 30s$) which can be used as a metastable state for various purposes, as will be explained in the rest of the thesis. The level diagram of such a barium ion is given in Figure 3.2.

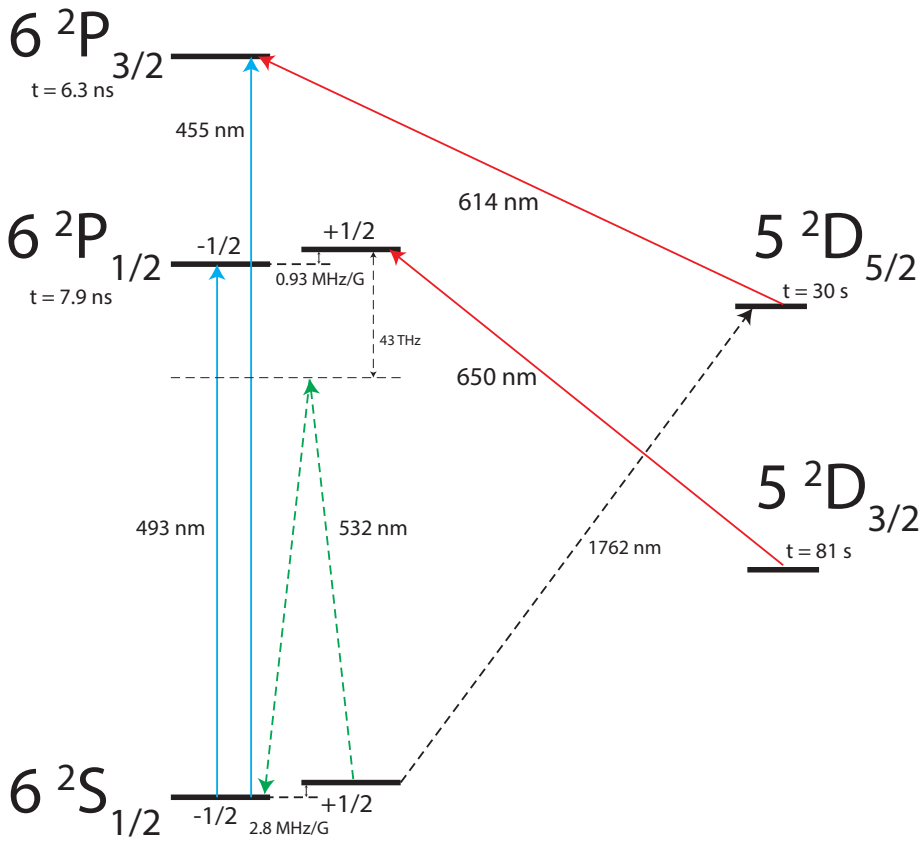

FIGURE 3.2: **Energy level diagram of $^{138}Ba^{+}$**: Relevant energy levels which shows typical requirements in terms of laser wavelengths, to trap and use this atom as a qubit. The Zeeman splitting is only shown for the levels of $S_{1/2}$ and $P_{1/2}$, such states are labeled as $\pm 1/2$. t represents the lifetimes of each of these levels. The arrows show the respective transition frequencies, with their colors chosen approximately to depict what they look like. 493 nm, 455 nm, 650 nm and 614 nm drive dipole transitions; 1762 nm drives a quadrupole transition. 532 nm light which is very far detuned from the $P_{1/2}$, are used for driving Raman transitions. The wavelengths and lifetimes have been sourced from [89], [91] and [92]

The transition between $^2S_{1/2}$ and $^2D_{5/2}$ is a 1762 nm quadrupole transition with a linewidth of 6.1 mHz. The $^2D_{5/2}$ level can be cleared out since this state couples in a dipolar fashion to $^2P_{3/2}$.

3.1.2 The ytterbium qubit

The $^{171}Yb^{+}$ ion is an appealing platform because it is a naturally abundant, stable isotope with a nuclear spin of I= $\frac{1}{2}$. This nuclear spin I= $\frac{1}{2}$ now gets added to the total angular momentum compared to barium-138 from before, F = I+J resulting in hyperfine split states corresponding to different F numbers for a given term symbol J_{L+S}. For example, in $^{171}Yb^{+}$the ground $S_{1/2}$ levels are split into two hyperfine levels corresponding to F=0 and F=1, each of which is further split into Zeeman levels based on the projection of F into the quantization axis. Its primary Doppler–cooling transition, $^2S_{1/2} \leftrightarrow {}^2P_{1/2}$, occurs at 369 nm—in the ultraviolet and accessible with commercial diode-laser systems and transmissible through optical fibers over short distances. Coherent qubit rotations are typically implemented with Raman beams near 355 nm. As illustrated in Fig. 3.3, the qubit is encoded in the magnetic-field-insensitive "clock" states of the $^2S_{1/2}$ ground manifold,

$$|0\rangle \equiv |F = 0,\, m_F = 0\rangle\,, \qquad |1\rangle \equiv |F = 1,\, m_F = 0\rangle\,.$$

Since these states have $m_F = 0$, they enjoy long coherence times [93]. To keep the electron in the $S_{1/2}$ and $P_{1/2}$ levels, it is also required to use a repumping light. In the the first laser cooling implementation of Yb^{+}, a 2.4 μm transition [94] was used for repumping. However, nowadays it is common to use 935 nm light for repumping [95].

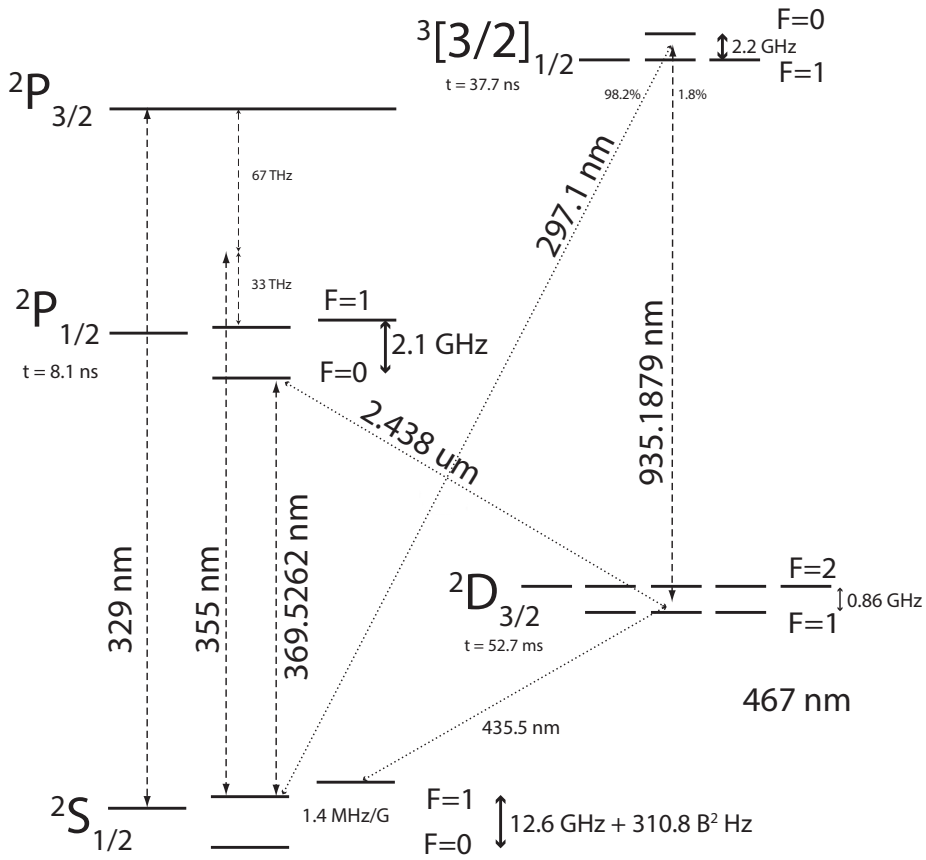

FIGURE 3.3: **Energy level diagram of $^{171}Yb^+$.** We only show the levels that we use in our experiment. $^{171}Yb^+$is has a nuclear spin of one-half resulting in hyperfine splitting of the energy levels, which is typically in the GHz frequency range. 99.5% of light decays to the $S_{1/2}$ manifold after decaying from $P_{1/2}$, the remaining decay to the $D_{3/2}$ manifold is cleared out using 935 nm light. Doppler cooling is done on the 369 nm line, while qubit rotations between $|0\rangle \equiv |S_{1/2}, F = 0\rangle$ and $|1\rangle \equiv |S_{1/2}, F = 1, m_F = 0\rangle$ is driven by Raman transitions with pulsed 355 nm light. Microwaves have also been used for the same. t denotes the lifetimes of the state. The displayed wavelengths, branching ratios and lifetimes have been sourced from [96], [89] and [97]

3.1.3 Possible encoding of states in an ion

Given the rich structure of the atomic ions, there are various ways to encode a qubit. The most obvious choice is to encode them in the Zeeman states of the ground S manifold [98]. The splitting between such states is on the order of several MHz and such transitions are easy to address using either a radio-frequency antenna or

a two-photon Raman process with the frequency difference between the two arms calibrated as the qubit frequency difference [99]. For atoms with a nuclear spin in stable, odd mass-number isotopes, there also exist hyperfine levels in the ground manifolds, which are typically split in the GHz frequency range. They are extremely good as memory qubits due to the long coherence times, which come from their first-order magnetic field insensitivity [100].

One can also store the qubits in two different manifolds, with a quadrupole coupling to ensure a long T_1 time for the qubit. For example, a specific Zeeman level in $^2S_{1/2}$ and another specific Zeeman level in $^2D_{5/2}$ can serve as the two basis states [101]. In this case, the energy splitting between the two would be an optical frequency difference spanning hundreds of THz. Driving transitions between such states would be possible by a narrow linewidth laser to keep track of the phase precisely. Such optical qubits are usually more difficult to control due to the need to obtain and lock a narrow linewidth laser to a high finesse cavity.

The third option would be to store qubits in a metastable state, for example the D manifold. The qubit states would still be Zeeman states (or hyperfine states depending on the nuclear spin), the only difference is that the qubits would need to be initialized to the metastable state via an optical transition, and then coherent operations can be performed either by radio-frequency fields or two-photon Raman transitions. These three schemes are what are known as the omg (optical, metastable and ground) architecture for encoding qubits [102].

3.2 Photonic qubit

A photon is a quantized excitation of the electromagnetic field: a mass-less, spin-1 boson that always propagates at the speed of light in vacuum, carries an angular-momentum projection of $\pm\hbar$ along its direction of motion, and couples to charged matter through the elementary electric charge. Because it lacks rest mass

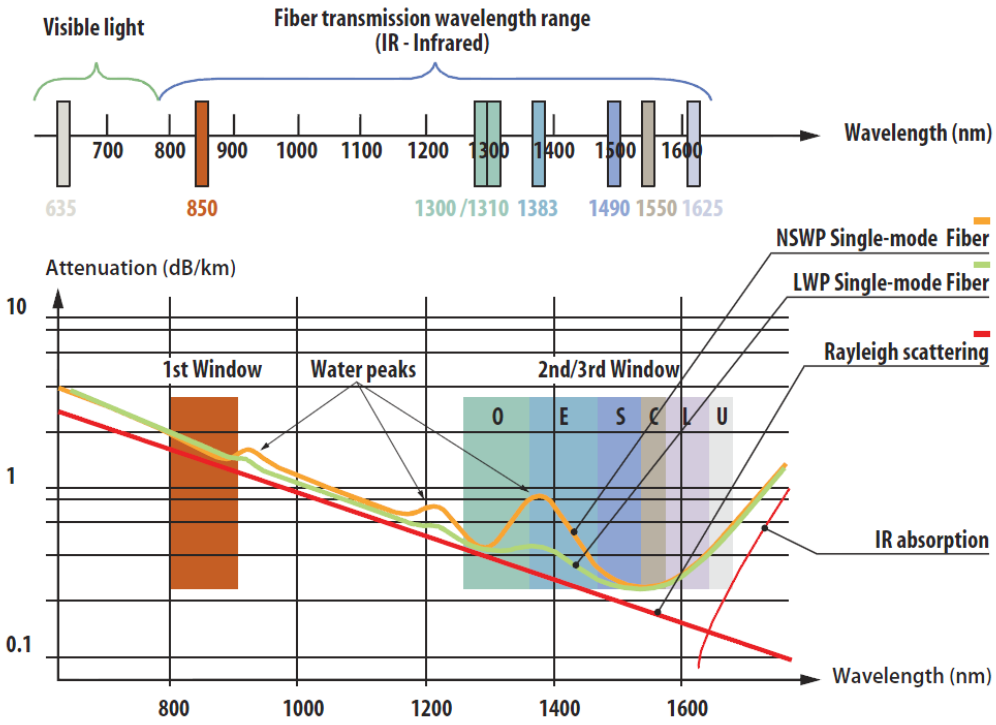

FIGURE 3.4: **Wavelength dependence of fiber attenuation:** Unless there are any absorption peaks at a given wavelength, the fiber attenuation usually goes down with increasing wavelength. At 493 nm, the attenuation is 30 dB/km. Over 10 meters, this corresponds to a 7% loss in transmitted power.

and interacts only via weak electric–dipole couplings, a single photon is remarkably resistant to environmental perturbations. These properties hint at why light can be a good qubit. Photons can manifest themselves as a variety of orthogonal solutions of Maxwell's equations which may be distinguished by polarization, spatial profile, arrival time, or frequency. A two-dimensional sub-space of any of these modes can then define a photonic qubit. In *single-rail* encoding the occupation number of one mode represents $|0\rangle$ (vacuum) or $|1\rangle$ (one photon) [103]. In *dual-rail* encoding the presence of a single photon in either of two orthogonal modes (e.g. horizontal, $|1_H 0_V\rangle$, or vertical, $|0_H 1_V\rangle$, polarization) spans the qubit [104]. Polarizing beam splitters along with wave plates and retarders can distinguish these basis states with very low error probabilities, below 10^{-5}.

Photons also have no intrinsic relaxation time. Initializing a register to $|0\rangle^{\otimes n}$ is as simple as leaving the optical modes empty; putting a heralded single photon in a chosen mode defines $|1\rangle$.

Because photons interact weakly with both the environment and one another, decoherence is dominated by classical channel imperfections such as fiber attenuation ($\sim 0.2\,\mathrm{dB\,km^{-1}}$ at 1550 nm), chromatic dispersion, and thermally driven phase drift. Even so, kilometer- scale coherence lengths are routine, and the absence of photon–photon coupling eliminates correlated noise between neighboring qubits. Any single-qubit unitary $U \in \mathrm{SU}(2)$ decomposes into a few beam-splitters and phase shifters [104]. Two-qubit gates are harder. Optical Kerr nonlinearities are currently too weak and lossy for fault-tolerant thresholds, so photonic platforms rely on linear-optical, measurement-based schemes (KLM, fusion, parity checks) which are probabilistic in nature [22, 104]. State read-out of photonic qubits is easy due to the high quantum efficiency of superconducting nanowire single photon detectors and avalanche photo-diodes. All of these suggest why photons can serve as a good qubit [105]. However, the same weak interaction that preserves coherence hampers deterministic two-qubit logic and fiber loss limits passive storage to microsecond delay lines [106]. Current optical memories in atomic ensembles or cavity-coupled emitters add complexity and are not yet universal or error-corrected [107]. Consequently, most scalable quantum computing platforms pair stationary matter qubits (for computation and storage) with photonic "flying" qubits (for communication), exploiting each platform's comparative advantages while respecting its limitations. Room-temperature operation, negligible dephasing in flight, and compatibility with existing fiber networks allow photons to distribute entanglement over metropolitan or even satellite-to-ground links [108, 109]. In modular architectures, they shuttle quantum states between trapped-ion, neutral-atom, or superconducting *memory* qubits [1, 53, 85, 110]. For quantum networking purposes, they have already been

leading the way from early on when the first quantum key distribution schemes like BB84 were based on polarized photons [111].

3.2.1 Possible encoding of states in a photon

As stated earlier, there are various possible ways to encode quantum states in a photon. Usually, single or dual rail encoding schemes use different modes of the photons to encode the information in. For example, in the dual rail encoding scheme, one can use two orthogonal polarizations to encode two quantum states:

$$|0\rangle = |1\rangle_H \otimes |0\rangle_V \tag{3.3}$$

$$|1\rangle = |0\rangle_H \otimes |1\rangle_V \tag{3.4}$$

Polarization is especially easy to control via passive birefringent devices, thereby constituting a popular choice. Another option would be to use two distinct frequencies of these photons. They can be controlled by the use of active electro-optic devices [112]. Unlike polarization, which can get scrambled when traveling over long distances, the frequency of a photon is comparatively robust when traveling longer distances. Orbital angular momentum (OAM) can also act as a carrier of quantum information [113]. It is manipulated with phase plates that imprint a helical phase onto the beam's transverse profile: the resulting azimuthal phase variation breaks cylindrical symmetry, so the orbital contribution

$$\mathbf{L} = \mathbf{r} \times \mathbf{p}$$

becomes nonzero. For classical light, the momentum density $d\mathbf{p}/dV$, is given by $(\vec{E} \times \vec{B})/c^2$. A mode carrying a single quantum of total angular momentum merely rotates about its propagation axis and contains only spin angular momentum (SAM), not OAM. Genuine OAM arises in higher-order modes, i.e. when $\Delta m \geqslant 2$.

Photon arrival times provide another encoding option. In time-bin qubits, the qubit states correspond to distinct temporal windows, typically generated with an

unbalanced interferometer or through successive excitations of a single photon emitter [114]. Time-bin states propagate over long distances with high robustness, but their analysis can require path-stabilized delay interferometers.

4

Qubit Confinement: Ion Trapping

To be able to use atoms as qubits, the first step is to localize them in space to ease the control requirements of the electromagnetic fields interacting with them. One can imagine having a lattice of atoms fixed in space and using directed laser fields interacting on an individual level with the atoms to coherently control them. Indeed, this has become one of the prominent ways to make a large qubit array quantum computer: by making a grid of focused laser beams to trap atoms which are called optical tweezers [115–117].

One can also ionize an atom and use its charge as a degree of freedom to exert a confining force via electric fields. However, in free space, Gauss's law states $\nabla \cdot \mathbf{E} = 0$, which physically means that free particles cannot be maintained in a stable equilibrium configuration by inverse square forces. This is also known as Earnshaw's theorem [118]. Intuitively, one can understand this as follows. Since the field is divergenceless, there are no points in space where all the electric field vectors face inward, which is essential for confinement. If there are electric field vectors pointing inward along a specific direction, there are necessarily other directions where the field directs outward. However, a dynamic potential with specific geometries can generate a time-averaged trapping force. The first implementation of this was by Wolfgang Paul and his discovery of the Paul trap, for which he was awarded a share of the Nobel Prize in 1989 [119, 120]. Since the introduction of radio-frequency Paul traps, they have found an enormous number of use cases in atomic clocks, mass and

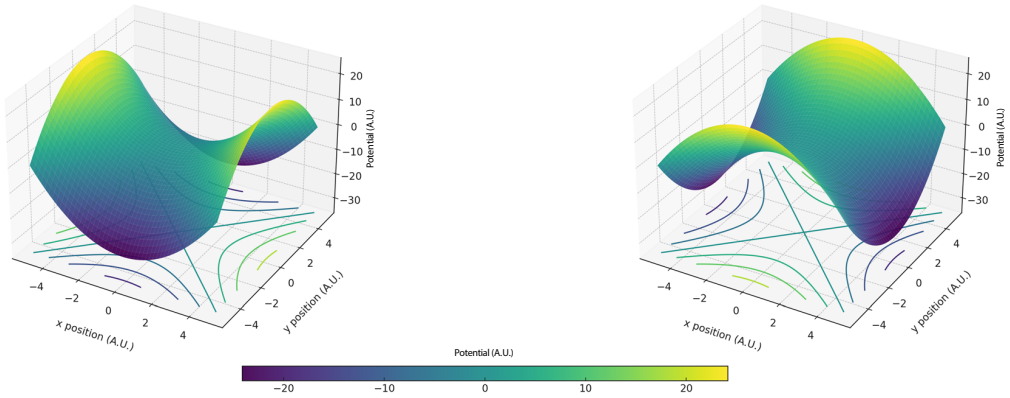

FIGURE 4.1: **Oscillating Paul trap potential:** The potential in arbitrary voltage units (A.U.) are plotted as a function of position at two different times. The left figure shows the potential due to the four rods which is confining in the y direction and anti-confining along the x direction. However, within half a cycle of the supplied radio-frequency on the rods, this orientation flips.

frequency spectroscopies, quantum computing, etc. [121, 122] Now, there exists a variety of ion trap geometries and a nice collection of them exists on the Maciej Malinowski website [123].

To motivate the geometry of a Paul trap, we start with a general parabolic potential that we wish to trap ions in. We can write such a field upto a constant C as [124]:

$$U(r) = \frac{V_0}{2r_0^2}(\alpha x^2 + \beta y^2 + \gamma z^2) + C \tag{4.1}$$

But we know that $\nabla \cdot \mathbf{E} = 0 \implies \nabla^2 U = 0 \implies \alpha + \beta + \gamma = 0$. This can be satisfied in different ways. Let us focus on the case where $\alpha = -\beta$ and $\gamma = 0$. The desired potential, up to some constant factor, then becomes:

$$U(r) = \frac{V_0}{2r_0^2}(x^2 - y^2) + C \tag{4.2}$$

However, it is still clear that the force for this is confining in the x direction and anti-confining in the y direction. This suggests that we should apply an oscillating

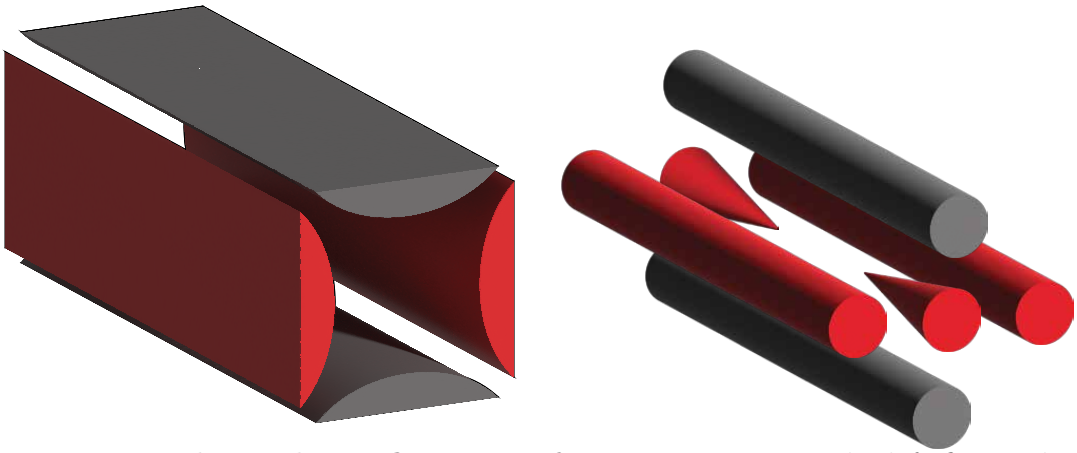

FIGURE 4.2: **Electrode configuration for ion trapping:** The left figure shows what an ideal hyperbolic configuration would look like. The right figure shows how a 4-rod Paul trap looks like in the experiments that we have. The four cylindrical rods provide radial confinement only. We use two cylindrical pointed needles along the axis with a static voltage for axial confinement. The atomic ions which get trapped in the center of the needles, are made to line up axially by making the axial confinement the weakest and the radial confinement non-degenerate in their frequencies.

field that rapidly switches directions. This potential can be generated by hyperbolic electrodes, as is evident from the hyperbolic potential. Suppose we switch their polarity at a very high frequency (>10 MHz). In such a case, the total potential would look like:

$$U(r) = \frac{V_0}{2}\cos(\Omega_T t)\left(1 + \frac{x^2 - y^2}{r_0^2}\right) \tag{4.3}$$

This does not generate any field along the z direction. For that purpose, we can put a pair of end-caps held at a fixed potential at each end in the z direction. This would create confinement in the z direction and anti-confinement in the x-y plane.

$$U_{cap} = \frac{U_0}{z_0^2}\left(z^2 - \frac{x^2 + y^2}{2}\right) \tag{4.4}$$

For ideal hyperbolic electrodes with perfect point end caps, one can expect to get a sum of the potentials $U(r) + U_{cap}$. However, since we need to collect light from these

trapped ions and we need to send laser light at the ions, we would like to have high optical access. We can make our trap out of 4 cylindrical rods, two of which we drive with radio frequency signals, the other two we hold at a fixed potential. Finally, two coaxial needles come in along the z direction on either side of the ion. Now, this gives us the final potential that will be confining.

$$V_{tot} = \frac{V_0}{2}\cos(\Omega_T t)\left(1 + \frac{x^2 - y^2}{r_0^2}\right) + \frac{U_0}{z_0^2}\left(z^2 - \frac{x^2 + y^2}{2}\right) \tag{4.5}$$

The corresponding field from this potential is $E = -\nabla V_{tot}$

$$E = -V_0\cos(\Omega_T t)\left(\frac{x\hat{x} - y\hat{y}}{r_0^2}\right) - \frac{U_0}{z_0^2}\left(2z\hat{z} - x\hat{x} - y\hat{y}\right) \tag{4.6}$$

Naively, if we time-average this force on a positively charged ion, for $U_0 > 0$, we will get a net inward force only along the z direction and an outward force in the x,y plane. However, for a second let us imagine the atomic motion due to an effective trapping potential and an oscillating driving force.

$$x(t) = x_{trap}(t) + x_{drive}(t) \tag{4.7}$$

Here, the drive at $\cos(\Omega_T t)$ causes the atom to wiggle around at the same frequency with some phase lag. If one now averages over the path that the ions follow, one will get an extra cosine term leading to a cosine-squared term and an averaged non-zero inward force. For an ion with mass m and charge Q, we can write the differential equations as follows:

$$\ddot{x} = -\frac{Q}{m}\left(\frac{V_0}{r_0^2}\cos(\Omega_T t)x - \frac{U_0}{z_0^2}x\right) \tag{4.8}$$

$$\ddot{y} = \frac{Q}{m}\left(\frac{V_0}{r_0^2}\cos(\Omega_T t)y + \frac{U_0}{z_0^2}y\right) \tag{4.9}$$

$$\ddot{z} = -2\frac{Q}{m}\frac{U_0}{z_0^2}z \tag{4.10}$$

The equation in the z direction is harmonic in nature with a frequency $\omega_z = \sqrt{\frac{2QU_0}{mz_0^2}}$. We can rescale Eqn. 4.10 in terms of an unitless parameter $\tau = \Omega t/2$ to obtain equations of the form

$$\frac{\mathrm{d}^2x}{\mathrm{d}\tau^2} = -\frac{4Q}{\Omega_T^2 m}\left(\frac{V_0}{r_0^2}\cos(2\tau) - \frac{U_0}{z_0^2}\right)x \tag{4.11}$$

$$\frac{\mathrm{d}^2y}{\mathrm{d}\tau^2} = +\frac{4Q}{\Omega_T^2 m}\left(\frac{V_0}{r_0^2}\cos(2\tau) + \frac{U_0}{z_0^2}\right)y \tag{4.12}$$

$$\frac{\mathrm{d}^2z}{\mathrm{d}\tau^2} = -\frac{8Q}{\Omega_T^2 m}\frac{U_0}{z_0^2}z \tag{4.13}$$

The equations in the x,y plane are similar in form to Mathieu equations, which look like the following:

$$\frac{\mathrm{d}^2x}{\mathrm{d}\zeta^2} + (2q\cos(2\zeta) + a)x = 0 \tag{4.14}$$

By comparison, we get the following expressions for a and q:

$$q_x = \frac{2QV_0}{m\Omega_T^2 r_0^2} \qquad a_x = -\frac{4QU_0}{m\Omega_T^2 z_0^2} \tag{4.15}$$

$$q_y = -\frac{2QV_0}{m\Omega_T^2 r_0^2} \qquad a_y = -\frac{4QU_0}{m\Omega_T^2 z_0^2} \tag{4.16}$$

We can rearrange to see $q_{x,y} = \pm\frac{2QV_0}{r_0^2}\frac{1}{m\Omega_T^2}$ which shows that it is a ratio of how strongly the RF field curves compared to the ion's resistance to move when shaken at a frequency Ω. The Mathieu q parameter is basically the modulation depth of the spring constant that the ion feels from the RF drive. It tells us how strong the oscillating quadrupole "push" is compared to the ion's inertia at the RF drive frequency. A small q means that the RF is fast/weak enough that the ion mainly feels a time-averaged pseudopotential, and a large q means the RF push is strong/slow enough to cause big micromotion and, eventually, parametric instability. Under the condition $(|a_i|, q_i^2) << 1$, and to the first order, one can solve these equations to

obtain the ion trajectory as :

$$r_{x,y}(t) = A_i cos(\omega_i t + \phi_i)\left(1 + \frac{q_i}{2} cos(\Omega_T t)\right), \qquad \omega_i = \left(\sqrt{a_i + \frac{q_i^2}{2}}\right)\frac{\Omega_T}{2}, \quad i = \{x, y\} \tag{4.17}$$

From Fig. 4.3, we observe that there are two different periodic motions, a slower one

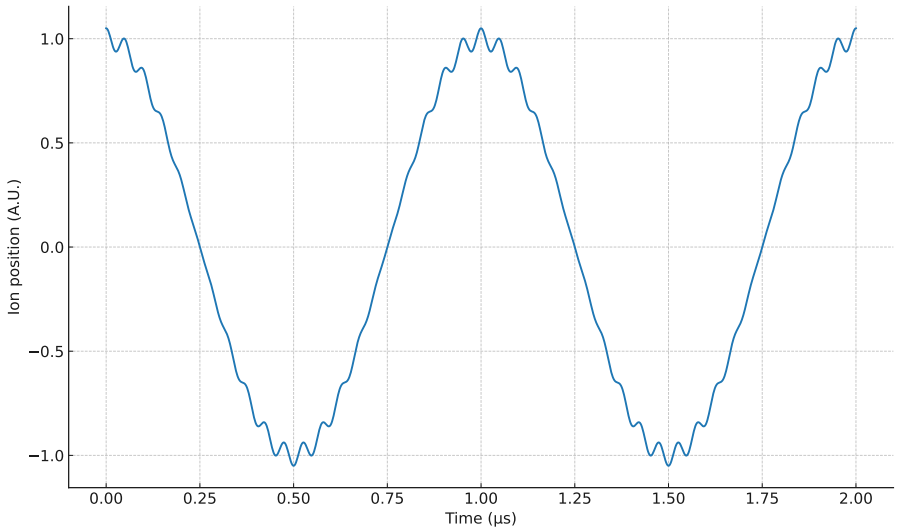

FIGURE 4.3: **Atomic ion position in a trap:** We plot the spatial position of an ion along a specific dimension as a function of time. Assuming the following parameters $q = 0.1$, $\Omega = 20MHz$, $\omega = 1MHz$, we obtain the displayed atomic motion. The low frequency oscillations at ω which is very clearly visible throughout is called secular motion and is due to the effective confining potential. The high frequency motion, discernible at the extremum points is driven motion or micromotion at the trap frequency Ω_T

at ω_i known as secular motion, and a much faster one at the driving frequency of the trap Ω_T known as micromotion. Given that we have a stable ion orbit, the amplitude of micromotion is much smaller than that of secular motion when $a_i < q_i^2 << 1$. Micromotion is suppressed relative to secular motion, by a factor of q_i, and causes unwanted motion of the ions. We say unwanted because the fast motion of the ion at the drive frequency can cause significant higher-order Doppler shifts, changes in line shapes of atomic transitions and reduced confinement time of the ion in absence

of cooling. However, it is the presence of micromotion that enables the trapping of the ion.

If there are static, stray electric fields $E_{DC}\hat{x}$ (assuming the stray field is in the x direction without loss of generality), then in Eq. 4.7, there is an extra term QE_{DC}/m [125]. This changes the solution of the equation to

$$r_x(t) = (A_0 + A_i \cos(\omega_i t + \phi_i)) \left(1 + \frac{q_i}{2} \cos(\Omega_T t)\right) \qquad A_0 = \frac{QE_{DC}}{m\omega_x^2} \tag{4.18}$$

This displacement of the ion causes excess micromotion along the $\hat{x}$ direction, as we can see from the extra term $A_0 \frac{q_i}{2} \cos(\Omega_T t)$. Similarly, a displacement along the $(\hat{x}+\hat{y})$ direction will cause micromotion along the $(\hat{x}-\hat{y})$. In general, micromotion happens along the direction of the instantaneous electric field lines at the ion position. Unlike secular motion, which can be cooled down by various laser cooling techniques as we will see in the next chapter, micromotion cannot be cooled down because it is driven by an external field. As such, it is critical that we ensure there is no excess micromotion by making sure there are no stray fields. However, imperfections in the trap, typically due to surface roughness on the rods of the trap or close by dielectric structures, can cause charge accumulation, which can create stray electric fields. For this reason, we apply DC voltages on the four rods to cancel out this stray field. There can also be excess micromotion if the driving fields on the two rods are not in phase. One can make them run in phase by adding a big capacitor between them.

Once we make sure that there is no excess micromotion and in the limit ($a << q^2$),

we see that the secular motion along the three axes is characterized by:

$$\omega_x = \frac{Q}{m}\sqrt{\frac{\eta^2 V_0^2}{2\Omega_T^2 r_0^4} - \frac{mU_0}{qz_0^2}} \tag{4.19}$$

$$\omega_y = \frac{Q}{m}\sqrt{\frac{\eta^2 V_0^2}{2\Omega_T^2 r_0^4} - \frac{mU_0}{qz_0^2}} \tag{4.20}$$

$$\omega_z = \sqrt{\frac{2QU_0}{mz_0^2}} \tag{4.21}$$

Note that the secular frequencies in the x-y plane are degenerate which can lead to inefficient laser cooling in the said plane. Therefore, it is important to break this radial degeneracy so that a single laser beam, in principle, can be non orthogonal to all the principal axes of the trap, and therefore address the motional modes in all three directions and provide good laser cooling. This can be done by applying static quadrupole voltages on the four rods which create additional confinement and anti-confinement along the x and y directions thereby lifting this degeneracy. The new frequencies are then given by $\omega_{new} = \sqrt{\omega_{x,y}^2 \pm \frac{QU_{DC}}{mr_0^2}}$. We can cool the secular motion so well using laser cooling techniques that they start behaving as a quantum harmonic oscillator. We are then able to speak in terms of occupation numbers of the phonon modes along the three principal directions. They are crucial for trapped atom quantum computing as they are used for performing two qubit gates, cooling operations, etc. [121, 126]. In a different architecture, by having exquisite control over these bosonic modes, one can make qubits out of these fock states, as well as perform quantum simulations [127, 128].

4.1 Ion Trap Construction

Our laboratory has three home-built, tungsten four-rod Paul traps: two legacy systems (Alice and Bob), which we inherited before I joined the group, and a third trap (Cleo) designed during our most recent apparatus development phase. A cross-

sectional view of all three traps is presented in Fig. 4.4.

Alice and Bob share a conventional square geometry: each uses rods of 0.50 mm diameter, with 1.00 mm spacing between adjacent electrodes on all sides. All these systems serve for general quantum-networking experiments and protocol development.

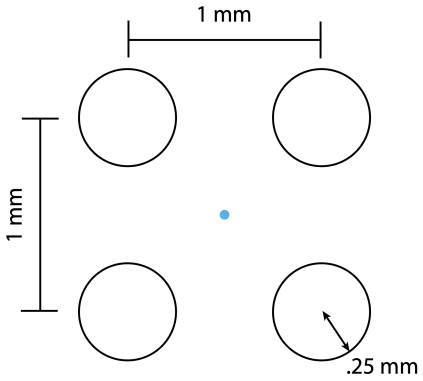

(a) Cross section of the rod trap for Alice and Bob with a square aspect ratio

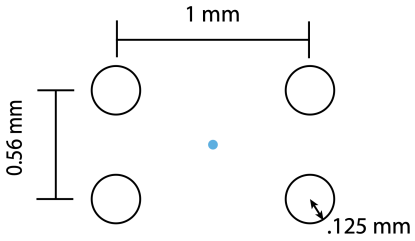

(b) The rod trap for Cleo has an elongated gap between rods along the light collection direction to prevent clipping of emitting light.

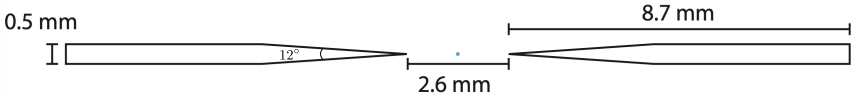

(c) Needle dimensions for axial confinement. For Cleo, the constructed trap had a needle distance longer than designed due to technical challenges, resulting in lower than expected axial frequencies. The cone tip as measured from their pictures suggest an angle of about 12°.

FIGURE 4.4: **4-rod trap dimensions for our setup**

Cleo was specifically engineered to demonstrate high-rate remote entanglement, which requires maximal photon collection. To achieve this, we integrated high-numerical aperture lenses in vacuum (NA = 0.8) that need large optical access. In a standard four-rod trap, the electrodes themselves can block a significant fraction of the ion's emission solid angle. To mitigate this, Cleo's electrode layout is different from the square aspect ratio: its rods are reduced to 0.25 mm in diameter, and

the lateral spacing is elongated to 1.00 mm along one axis and narrowed to 0.56 mm along the orthogonal (short) axis. This rectangular configuration minimizes blockage by the rods, maximizing the effective collection solid angle.

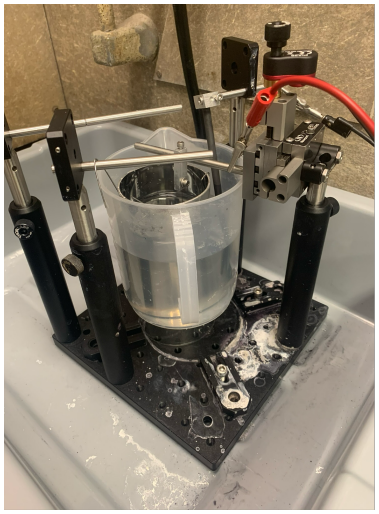

FIGURE 4.5: Setup for electrochemical etching. The stainless steel cylinder can be seen to isolate turbulence at the cathode. The rod can be seen clamped to the rectangular block and the more prominent graphite rod can be seen to it's right.

FIGURE 4.6: One of the fabricated needle for Cleo.

The trapped atomic ions have well-defined phononic states of a quantum harmonic oscillator and it is possible to measure them as described in the next chapter. As such,

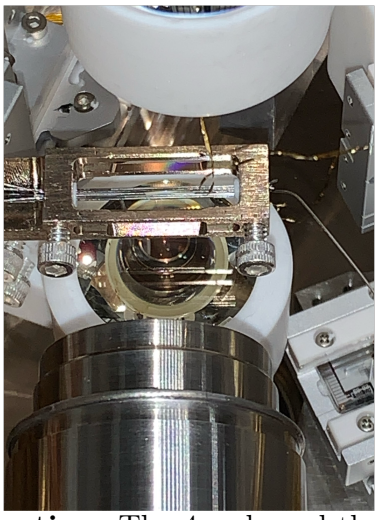

FIGURE 4.7: **Trap construction**: The 4 rods and the two needles can be seen in the trap holder. The white parts at the top and bottom are the MACOR holders, carrying the in-vacuum aspheres. The protruding steel cylinder on the bottom is a reentrant window for imaging ytterbium. Gold wires can be seen, which are clamped to the surface of the asphere for grounding the Indium-tin oxide (ITO) conductive coating on it's surface

we can study the heating rate of these phonon modes and how they are affected due to the ion trap itself. It has been observed that this heating rate scales roughly with the distance d between the electrode surface and the atomic ion as d^{-4}, is inversely correlated with the secular frequencies and decreases when the ion traps are cooled to low temperatures [129–133]. It has also been observed that surface electric field noise plays a big role in high heating rate and as such it is important to reduce the surface roughness as much as possible [134]. Therefore, we use electrochemical etching techniques to decrease surface roughness.

For our trap in Cleo we need four clean, smooth tungsten rods and two needles as the end caps. We follow the steps below to make them:

1. Start by having a 2M NaOH solution.
2. Use the tungsten rod as the anode and a graphite rod as the cathode.
3. Run 8A of current for 8 min. The structure used to hold the rods in place gets coated in salt from the fumes. We clean this to maintain its conductivity.

Continue etching until the rod breaks off and falls into the solution.

4. The part of the rod that falls into the solution is used as the needles.
5. For making the rods, we simply use a short etching time of approximately a minute to smoothen the surface.
6. After we are done with the etching step, we put them in an oxygen free environment, so that the rod surface does not oxidize.

We secure the six trap electrodes (four rods and two needle electrodes) in machined MACOR holders. Each MACOR block contains five precision-drilled holes: four for the rods and one for the needle electrodes. When inserting a needle electrode, we thread its tapered tip carefully through the corresponding hole to avoid contact that could blunt or deform it. Because the electrodes are held by friction fit, it is critical to use rods and needles of the correct diameter; we fabricated a batch of approximately thirty and selected those with the smoothest needle tapers and optimal fit in the MACOR.

Once populated, each MACOR holder is mounted onto a larger support structure attached to a vacuum chamber flange. The holder is secured by two side screws (originally intended as setscrews, but replaced with standard machine screws during assembly). Unfortunately, this substitution created an unwanted scattering of laser light of wavelengths 413, 614, 650 and 935 nm directed at the ion. However, we have not noticed any undesirable effects on the trap due to the scattered light.

We drive our traps with an RF source at a few tens of megahertz, but before the signal reaches the electrodes it is amplified and sent through a quarter-wave helical resonator to clean it up and match the trap impedances. The setup works as follows: the amplified RF feeds an adjustable coil 'antenna' inside the resonator, which sits next to two identical helical coils (15 mm pitch) wound on the same form but kept apart by a Teflon spacer. These two helical coils that connect to the trap rods are made of 5 mm thick copper with a coil diameter of 3.4″ and a coil height of 5.2″.

They're housed inside a hollow 4″ diameter copper can that acts as a ground shield. Here, at resonance, the guided mode inside the resonator along its axis has a quarter wavelength equal to the height of the helical coil. Note that the wavelength of this effective guided mode is shorter than the free-space wavelength.

The can also holds four extra copper wires (each on its own SMA connector) that go to the two DC rods and the two needle electrodes. After everything was cleaned with citric acid, the resonator rings with a quality factor ~ 150 and a resonance at 23.427 MHz. Of course, over time, an oxide layer can build up and deplete the quality factor, as well as change the resonance frequency.

In practice, one end of our coil assembly takes the amplified RF, and the other end terminates with six wires: two carry the RF to the trap rods (we short them together with a capacitor (100nF, 1kV) so they stay in phase and avoid unfixable micromotion), and four carry fixed DC voltages. All six go through a vacuum-rated RF feedthrough (good up to 2 kV against ground). The Alice and Bob traps use similar setups with older resonators but the same basic RF-delivery scheme.

4.2 Ion Loading

In our experiments, we work with both barium ($^{138}Ba^{+}$) and ytterbium ($^{171}Yb^{+}$) atomic ions, requiring us to develop methods for generating and trapping these species. The process of ion trapping begins with an atomic source that emits a thermal beam of neutral atoms. This beam must pass through the trapping region of the linear Paul trap, which subsequently gets confined in a stochastic manner. To ensure a reasonable loading time (typically a few minutes), the atomic beam must have sufficient flux through the trap center.

Step 1: Atomic Beam Generation

To create the atomic beam, we use resistively heated atomic ovens. These ovens are mounted on holders that contain two small-diameter hollow needles (typically 1–2

mm), each containing the appropriate neutral atomic species. The oven assembly is affixed to the side of the vacuum chamber using Groove Grabbers from Kimball Physics, with the open end of each needle directed toward the ion trap center. One needle is filled with 99%+ isotopically enriched ^{171}Yb metal, while the other contains natural-abundance barium beads.

Ytterbium oven

Ytterbium is relatively stable in air, making the loading process straightforward. We load several mg of ^{171}Yb metal into a hypodermic needle, crimping one end to seal it. The needle is then fixed into the over holder with its open end aligned with the trap. We TIG weld a coil of .016″ diameter tungsten wire around the crimped end to serve as a resistive heater. We estimate the length of these tungsten wires to be roughly 2″. These ovens generally require ∼2 A of current to reach operational temperatures and produce a stable atomic flux for photoionization.

Barium oven and handling

Barium, on the other hand, is highly reactive and oxidizes quickly upon contact with air. This sensitivity necessitates a more involved loading procedure. First, the chamber is pumped to high vacuum, and the barium oven is pre-baked by running a high current (8A) to remove any residual moisture. The chamber is then back-filled with an inert gas (nitrogen) to atmospheric pressure. Barium beads, packaged under argon in sealed glass ampoules, are broken open in a dish. All tools used for handling are vacuum-cleaned in advance to remove surface contaminants. Using tweezers, the beads are loaded into the oven in a few seconds. Although some surface oxidation occurs during this time, visible as a whitening of barium, the bulk remains usable for atomic flux generation. Immediately after loading the oven, we closed the chamber and pumped it down.

In different trap systems, the barium ovens are configured slightly differently. For

example, in the Alice setup, the Ba oven is run at 8 A due to the fact that it does not contain a tungsten heating coil. In Bob and Cleo, where tungsten heating coils are used, the Ba ovens operate more efficiently, typically around 2 to 2.5 A, matching the currents of the Yb oven.

Step 2: Photo-ionization

The electronic configuration of ^{171}Yb is [Xe] 4f14 6s2. After removing an electron in it's outermost s-shell, the remaining s-electron bound to the atom is used for quantum computing. We use a 399 nm laser which is wavemeter locked to less than 10 MHz to drive a dipole transition between $^1S_0$ and $^1P_1$. Immediately after this, a 370 nm cavity-locked laser sends this excited electron to continuum, therefore completing photo-ionization. We use several mW of 399 nm and a few μW of 370 nm focused to a hundred micron spot size. A moving atom after getting ionized will get trapped if its kinetic energy is less than the depth of the potential of the trap. Subsequently, Doppler cooling beams reduce its temperature to a few micro Kelvin.

The electronic configuration for ^{138}Ba is [Xe] 6s^2. Similarly, we strip its outermost s-shell electron, but now we use a 413 nm laser beam. First, the electron gets promoted to $^3D_1$ via a quadrupole transition, followed by complete ionization using the same laser. Several mW of 413 nm laser power is required to perform this ionization. Another possible way to ionize them is for the first step to be a dipole transition via 553 nm light, which couples $^1S_0$ to $^1P_1$, followed by promotion to the continuum by 413 nm.

An important point to note here is that, since the ovens are at non-orthogonal angles to the ion traps, the atoms from the oven experience substantial Doppler shifts. Therefore, it is crucial to adjust the frequencies of the ionizing lasers. A typical atom beam, in our vacuum chambers, has a velocity of around 300 m/s. In

Table 4.1: Oven angles for different chambers

	Alice	Bob	Cleo
Angles for barium (θ)	15°	112.5°	67.5°
Angles for ytterbium (θ)	67.5°	157.5°	67.5°

such a case the Doppler shift is :

$$\Delta f = f\frac{v}{c}\cos\theta = \frac{v\cos\theta}{\lambda} = 750 \text{ MHz } \cos\theta \tag{4.22}$$

Table 4.1 lists these angles for our three chambers.

This chapter has demonstrated how we ionize and trap atomic ions in a stable configuration. The charge of the atom has acted like an extra degree of freedom to pin it in space. In the next chapters, we discuss how we can interact with these trapped atomic ions using electromagnetic fields.

5

Qubit Control: Atom Light Interaction

Atom-light interactions are the fundamental processes through which quantum control of atomic systems is achieved. In trapped ion quantum computing and quantum networking, the ability to manipulate the atom's spin states, control its temperature, perform entangling operations, and interface with photonic channels relies on precise and sometimes coherent control of these interactions [121, 135]. In the next couple of sections, we talk about both coherent and incoherent operations on the atomic ions.

5.1 System Hamiltonian

An ion trapped in a linear Paul trap has several degrees of freedom. The fact that it is trapped in a quadratic pseudo-potential makes it behave like a quantum harmonic oscillator; therefore, it has motional degrees of freedom which are the occupation numbers of phononic modes along different directions. The atomic species we deal with in this work has a single electron in its outer shell, which orbits around the nucleus, giving it a relatively simple atomic level structure. For theoretical consideration, we look at only two levels of the spin state at a time, corresponding to an effective two-level approximation. This means that the electron has a ground state and an excited electronic state which differ in energy by $\hbar\omega_0$. Then, any light interacting with the system, is considered by an interaction Hamiltonian [121, 135].

Therefore,

$$H = H_m + H_e + H_I \tag{5.1}$$

where we have three different Hamiltonians H_m, H_e, H_I corresponding to the motion, spin, and light-matter interaction of the atom.

$$H_m = \hbar\omega_m \left(a^\dagger a + \frac{1}{2} \right) \tag{5.2}$$

$$H_e = \frac{\hbar\omega_0\sigma_z}{2} \tag{5.3}$$

$$H_I = -\mathbf{d} \cdot \mathbf{E} \tag{5.4}$$

Here, $\sigma_z = |e\rangle\langle e| - |g\rangle\langle g|$ represents the diagonalized electronic Hamiltonian with $|e\rangle$ and $|g\rangle$ representing the two-level spin system with an energy splitting ω_0. The energy spacings of the quantized oscillations of the harmonic oscillator correspond to ω_m. In the presence of an electric field $\mathbf{E}$ and an effective dipole moment of the ion $\mathbf{d}$ we expect to see an interaction of the form $-\mathbf{d} \cdot \mathbf{E}$. Through the interaction Hamiltonian we expect to see terms that change the spin state of the electron or the motional state of the electron, or a coupling between each of them. We perform the analysis of this interaction Hamiltonian in the semi-classical framework, where the electric field is treated classically but the dipole operator is treated quantum mechanically. We assume a traveling plane wave in the x-direction with an arbitrary polarization $\mathbf{E}_0 = E_y\hat{y} + e^{i\phi}E_z\hat{z}$ of the form

$$\mathbf{E}(x,t) = \mathbf{E}_0 e^{i(kx-\omega t)+} + c.c. \tag{5.5}$$

We can write the interaction Hamiltonian in a complete basis as:

$$H_I = -\sum_{i,j\in\{e,g\}} |i\rangle\langle j| \langle i| \mathbf{d} \cdot \mathbf{E} |j\rangle \tag{5.6}$$

The matrix element $\langle e| \mathbf{d} \cdot \mathbf{E} |g\rangle$, gives rise to coupling strengths among two different levels that we choose based on selection rules. We will look at the three important

couplings which we use in our experiments to perform various tasks such as Doppler cooling or coherent transitions. But first, assume a coupling strength of $\langle e|\, \mathbf{d}\cdot\mathbf{E}_0\, |g\rangle = \frac{\hbar\Omega}{2}$, where $|\Omega|$ is the Rabi frequency of the driven transition and effective wave vectors and frequencies of the light are given by k and ω. We will see later that, different polarizations of the electric field, can couple different quantum states. We then rewrite H_I as

$$H_I = \frac{\hbar\Omega}{2}\left(|e\rangle\langle g| + |g\rangle\langle e|\right) e^{i(kx-\omega t+\phi)} + h.c. \tag{5.7}$$

This can be very easily generalized to 3 dimensions by replacing kx with $\mathbf{k}.\mathbf{r}$. We recognize that the two-level system with $|e\rangle$ and $|g\rangle$ can be written in terms of Pauli matrices:

$$|e\rangle\langle g| + |g\rangle\langle e| = \sigma_x \tag{5.8}$$

$$= \frac{1}{2}(\sigma_x + i\sigma_y) + \frac{1}{2}(\sigma_x - i\sigma_y) \tag{5.9}$$

$$= \sigma_+ + \sigma_- \tag{5.10}$$

Here, σ_+ and σ_- are the spin raising and lowering operators. Thus, we can write

$$H_I = \frac{\hbar\Omega}{2}(\sigma_+ + \sigma_-)e^{i(kx-\omega t+\phi)} + h.c. \tag{5.11}$$

Now we move to the interaction frame by the unitary transformation with the operator $U_0 = e^{-\frac{iH_0 t}{\hbar}}$ with $H_0 = H_m + H_e$, being the free Hamiltonian. After the unitary transformation, we get

$$H_{int.\ frame} = U_0^\dagger H_I U_0 \tag{5.12}$$

$$= e^{\frac{iH_m t}{\hbar}} e^{\frac{iH_e t}{\hbar}} \left(\frac{\hbar\Omega}{2}(\sigma_+ + \sigma_-)e^{i(kx-\omega t+\phi)} + h.c.\right) e^{-\frac{iH_e t}{\hbar}} e^{-\frac{iH_m t}{\hbar}} \tag{5.13}$$

We were able to do this because the motion part and the spin part commute ($[H_m, H_e] = 0$). Furthermore, we observe that $[H_m, (\sigma_+ + \sigma_-)] = 0$. Also, unlike regular angular

momentum, spin angular momentum is intrinsic and acts on different parts of the wave function, therefore $[\sigma_z, x] = 0$. Hence, we can rewrite

$$H_{int\ frame} = \frac{\hbar\Omega}{2} e^{\frac{iH_e t}{\hbar}} (\sigma_+ + \sigma_-) e^{-\frac{iH_e t}{\hbar}} e^{\frac{iH_m t}{\hbar}} \left(e^{i(kx-\omega t+\phi)}\right) e^{-\frac{iH_m t}{\hbar}} + h.c. \tag{5.14}$$

$$= \frac{\hbar\Omega}{2} (\sigma_+ e^{i\omega_0 t} + \sigma_- e^{-i\omega_0 t}) e^{\frac{iH_m t}{\hbar}} \left(e^{i(kx-\omega t+\phi)}\right) e^{-\frac{iH_m t}{\hbar}} + h.c. \tag{5.15}$$

The first part of the equation can be written as:

$$e^{\frac{i\omega_0\sigma_z t}{2}} (\sigma_+ + \sigma_-)\ e^{-\frac{i\omega_0\sigma_z t}{2}} = = e^{\frac{i\omega_0\sigma_z t}{2}} (|e\rangle\langle g| + |g\rangle\langle e|)\ e^{-\frac{i\omega_0\sigma_z t}{2}} \tag{5.16}$$

$$= e^{\frac{i\omega_0\sigma_z t}{2}} |e\rangle\langle g|\, e^{-\frac{i\omega_0\sigma_z t}{2}} + e^{\frac{i\omega_0\sigma_z t}{2}} |g\rangle\langle e|\ e^{-\frac{i\omega_0\sigma_z t}{2}} \tag{5.17}$$

$$= |e\rangle\langle g|\, e^{i\omega_0 t} + |g\rangle\langle e|\ e^{-i\omega_0 t} \tag{5.18}$$

$$= \sigma_+ e^{i\omega_0 t} + \sigma_-\ e^{-i\omega_0 t} \tag{5.19}$$

If we take the $e^{\pm i\omega t}$ term and combine it with the $e^{\pm i\omega_o t}$, we will get two slowly oscillating terms and two fast terms. Because the fast terms oscillate so quickly, at (roughly) the sum of the optical and laser frequencies, i.e. tens or hundreds of terahertz, their contribution averages to (almost) zero over any timescale on which the atomic state actually changes. We drop them by using the rotating-wave approximation (RWA), and it is valid whenever the atom–light coupling strength Ω and the detuning $\Delta = \omega_0 - \omega$ is much smaller than the optical frequency itself, $\Omega, |\Delta| << \omega_0$.

The motional part of the Hamiltonian in interaction frame is equivalent to writing the kx term by its Heisenberg-picture version [121],

$$kx(t) = \eta(au^*(t) + a^\dagger u(t)) \tag{5.20}$$

where we define the supremely important parameter of ion trapping called the Lamb-Dicke parameter [121] as

$$\eta = kx_0 = 2\pi\frac{x_o}{\lambda} \qquad x_0 = \sqrt{\frac{\hbar}{2m\nu}} \tag{5.21}$$

Here, η is a measure of the size of the wavefunction compared to the wavelength of light interacting with it and $u(t) = e^{i\nu t}\Phi(t)$ with $\Phi(t)$ being a periodic function with a period of $2\pi/\Omega_T$ and ν is the secular frequency of the trapped ion. u(t) satisfies the equation of motion $\ddot{u}(t) + \left(\frac{\Omega_T^2}{4}[a + 2q\cos(\Omega_T t)]\right) u(t) = 0$, with the boundary condition $u(0) = 1$ and $\dot{u}(0) = i\nu$. If the ion is sufficiently cold and tightly confined by the trap, η is small and the atom experiences a spatially homogeneous electric field from the light field. So we now have

$$H_{int\ frame} = \frac{\hbar\Omega}{2}\sigma_+ e^{i[(\omega_0-\omega)t+\eta(au^*(t)+a^\dagger u^*(t))]} + h.c. \tag{5.22}$$

For a trapped ion, if $(a, q^2) << 1$, we can rewrite the interaction Hamiltonian as

$$H_{int\ frame} = \frac{\hbar\Omega_0}{2}\sigma_+ e^{i[\eta(ae^{-i\nu t}+a^\dagger e^{-i\nu t})+\delta t+\phi]} + h.c. \tag{5.23}$$

Here $\delta = \omega - \omega_0$ is the detuning between the light's frequency and the frequency of the electronic two-level system, ϕ is the laser phase as measured with respect to the local oscillator in the lab frame, $\nu = \beta\omega_T/2$ is the secular frequency as we had seen in the previous chapter, and Ω_0 is the scaled interaction strength. In the limit where η is small, that is, the ion is cooled well, or the interacting wavelength is large or both, we obtain dynamics in the Lamb-Dicke regime. In such a case, we can expand the exponential and keep only the first-order terms, thereby giving us

$$\boxed{H_{int\ frame} = \frac{\hbar\Omega_0 e^{i(\delta t+\phi)}}{2}\sigma_+(1 + i\eta(ae^{-i\nu t} + a^\dagger e^{i\nu t})) + h.c.} \tag{5.24}$$

The first term gives rise to the carrier transition term for $\delta = 0, \phi = 0$

$$H_{carrier} = \hbar\Omega_0\sigma_x \tag{5.25}$$

This causes transitions between the two internal electronic states or spin-flipping transitions, as is evident by the σ_x operator. The second term gives the blue and

red sideband (bsb, rsb) transitions, which change the electronic state as well as the motional state (in terms of the phononic occupation number),

$$H_{rsb} = \frac{\hbar\Omega_0}{2}\eta[a\sigma_+ + a^\dagger\sigma_-] \tag{5.26}$$

$$H_{bsb} = \frac{\hbar\Omega_0}{2}\eta[a\sigma_- + a^\dagger\sigma_+] \tag{5.27}$$

For the red sideband, we need to have $\delta = -\nu$ and for the blue sideband we need $\delta = \nu$. These transitions increase or decrease the motional quantum number at the expense of changing the electronic spin state. The red sideband decreases one unit of motional quanta while exciting the electronic state. The reverse process occurs for the blue sideband. We can relate the coupling strengths of the carriers and sidebands as follows:

$$\Omega_{n,n-1} = \eta\Omega_0\sqrt{n} \tag{5.28}$$

$$\Omega_{n,n+1} = \eta\Omega_0\sqrt{n+1} \tag{5.29}$$

$$\Omega_{n,n-1} = \sqrt{\frac{n}{n+1}}\Omega_{n,n+1} \tag{5.30}$$

In general, one can couple any of the phononic states to any other by choosing appropriate detunings $\delta = \pm ml$, for any integer m. This comes at the cost of a reduced coupling strength. The generalized Rabi frequency for this case is given by [121]:

$$\Omega_{n+s,n} = \Omega_0 |\langle n+s| e^{i\eta(a+a^\dagger)} |n\rangle| \tag{5.31}$$

$$= \Omega_0 e^{-\eta^2/2}\eta^{|s|}\sqrt{\frac{n_<!}{n_>!}L_{n_<}^{|s|}(\eta^2)} \tag{5.32}$$

where $n_<(n_>)$ is the lesser (greater) of n+s and n and L is the generalized Laguerre polynomial given by:

$$L_{n_<}^{|s|}(\eta^2) = \sum_{m=0}^{n<}(-1)^m \binom{n_<+|s|}{n_<-m}\frac{\eta^{2m}}{m!} \tag{5.33}$$

5.2 Dipole coupling

We now look at different kinds of transition in terms of the effective Rabi frequencies, selection rules, and wavelengths of light that we use to drive our specific atomic systems. We have already seen that the general Rabi frequency for carrier transitions is proportional to $|\Omega|$, where

$$\hbar\Omega/2 = \langle e| \mathbf{d}.\mathbf{E}_0 |g\rangle \tag{5.34}$$

This equation is helpful in calculating the transition strength between any two states $|e\rangle$ and $|g\rangle$ mediated by the dipole interaction. But first it is important to find out the possible quantum numbers or energy levels that are driven by such an interaction. Using the fact that odd/even orbital angular momentum states L are odd/even under parity change, and so is the dipole operator, we can conclude that the change in orbital angular momentum number must be odd. Furthermore, by taking the expectation values of the following equation with respect to the states $|L, m_L\rangle$

$$[L^2, [L^2, r]] = 2\hbar^2(rL^2 + L^2 r) \tag{5.35}$$

we get the selection rule

$$\Delta L = \pm 1 \tag{5.36}$$

Obviously, since the dipole operator does not have any spin degree of freedom, it cannot effect changes to the spin quantum number of state. This along with $\Delta L = \pm 1$ straight forwardly gives

$$\Delta J = \pm 1, 0 \tag{5.37}$$

$$\Delta F = \pm 1, 0 \tag{5.38}$$

for $J = L + S$ and $F = J + I$, where I is the nuclear spin. Certainly $J : 0 \leftrightarrow 0$ and $F : 0 \leftrightarrow 0$ is not allowed since that would violate $\Delta L = \pm 1$.

If we have an electric field of different polarizations we can write them out as

$$\mathbf{E} = E_{\sigma^+}\frac{(\hat{x}+i\hat{y})}{\sqrt{2}} + E_{\sigma^-}\frac{(\hat{x}-i\hat{y})}{\sqrt{2}} + E_{\pi}\hat{z} \tag{5.39}$$

Here, σ^+ and σ^- are right and left circular polarizations of the electric field vector.

The dipole moment operator consists of the charge q and the position operator of the electron. Similar to the electric field, we write the position operator in the spherical harmonic basis

$$\hat{\mathbf{r}} = r\sqrt{\frac{4\pi}{3}}\left(Y_1^{-1}\frac{\hat{x}+i\hat{y}}{\sqrt{2}} + Y_1^0(\hat{z}) + Y_1^1\frac{\hat{x}-i\hat{y}}{\sqrt{2}}\right) \tag{5.40}$$

where the spherical harmonics are

$$Y_1^{-1} = \frac{1}{2}\sqrt{\frac{3}{2\pi}}\sin(\theta)e^{-i\phi} \tag{5.41}$$

$$Y_1^{1} = -\frac{1}{2}\sqrt{\frac{3}{2\pi}}\sin(\theta)e^{i\phi} \tag{5.42}$$

$$Y_1^{0} = \frac{1}{2}\sqrt{\frac{3}{\pi}}\cos(\theta) \tag{5.43}$$

The dot product then is:

$$\mathbf{r}\cdot\mathbf{E} = r\sqrt{\frac{4\pi}{3}}(E_{\sigma^+}Y_1^{-1} + E_{\sigma^-}Y_1^{1} + E_{\pi}Y_1^{0}) \tag{5.44}$$

By calculating the expectation value of the above operator over the angular part of the wavefunction, we find that light fields, whose polarization is along the π direction, induce transitions without any change in the z projection of the angular momentum.

$$\pi \rightarrow \Delta m_j = 0 \tag{5.45}$$

Circularly polarized fields, on the other hand, induce a unit change in the z projection of the angular momentum.

$$\sigma^+ \rightarrow \Delta m_j = +1 \tag{5.46}$$

$$\sigma^- \rightarrow \Delta m_j = -1 \tag{5.47}$$

Since we are looking at the z projection, that means that we have already assumed a quantization axis along the z direction. In a physical system, this is set by the direction of the magnetic field. In summary, light propagating along the quantization axis with circular polarization will induce transitions that change the angular momentum projection, whereas light with polarization parallel to the quantization axis cannot change the angular momentum. These are called σ and π transitions, respectively.

Now, we are ready to apply this knowledge to our system of interest. Fig. 5.1 shows the level diagram of $^{138}Ba^+$with all dipole transitions labeled. Clearly, the dipole transitions connect levels either between $S \rightarrow P$ or $P \rightarrow D$, following the selection rules described earlier. We see the low lying excited state $^2P_{1/2}$, which decays into the the ground state $^2S_{1/2}$ and the low lying, long-lived $^2D_{3/2}$ level. 73% of the time it decays to the S manifold by emitting a 493 nm photon and the remaining decay into the D manifold happens via a 650 nm photon [92]. As mentioned in Chapter 3, the 493 nm transition is the longest wavelength $S \leftrightarrow P$ transition among the group II ions, which makes barium ions appealing as a photonic qubit. One may also think of using the longer wavelength P $\rightarrow$ D transition of 650 nm. However, that transition has a lower branching ratio of 23% while emitting σ^+, σ^-, π photons which can lower the percent of collected photons. The higher energy $^2P_{3/2}$ state decays into the two D levels via various two wavelengths as seen in Fig. 5.1. Both these states are very short lived, having a lifetime of less than 8 ns. This is because there exist levels S and D which couple in a dipolar fashion to P, and the spontaneous emission

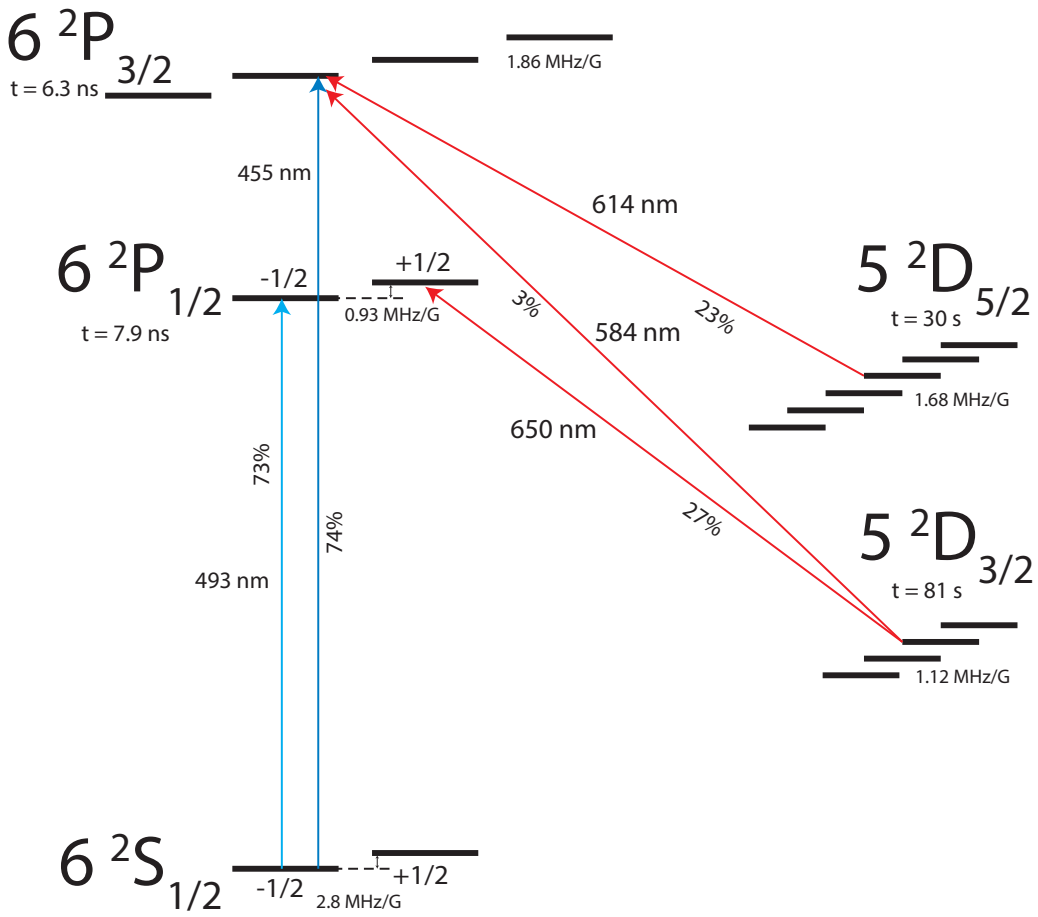

FIGURE 5.1: **Barium dipole transitions:** 493 nm and 650 nm are primarily used for cooling and detection, 614 nm for re pumping, while we do not use 455, 584 nm light. The wavelengths are take from [89].

rate goes as the square of the transition dipole moment, which we encountered earlier as Ω. For this reason though, the $S \leftrightarrow P$ transitions are good for laser cooling, state preparation and fluorescence based state detection, with a high scattering rate in the tens of MHz. In cases, when the spontaneous emission rate is comparable to the stimulated driving rate, equilibrium is reached and the dynamics of the system is completely incoherent. In the following sections, we go into details for each of these.

5.2.1 Applications: Doppler Cooling

Doppler cooling is a technique of laser cooling which takes advantage of the direction dependent Doppler shift of light as observed in the atom's frame of motion [77]. Here the following derivations are based on a two level atomic system. Before delving into the theory of Doppler cooling, we first state the photon scattering rate Γ by an atom with velocity $\mathbf{v}$, energy splitting ω with linewidth γ, interacting with laser light of intensity I is given by

$$\Gamma(\omega, \mathbf{v}) = \frac{s\gamma/2}{1 + s + 4\frac{(\omega - \omega_L + \mathbf{k}.\mathbf{v})^2}{\gamma^2}} \tag{5.48}$$

Here ω_L is the laser frequency, $\mathbf{k}$ is the laser propagation direction, and s is the saturation parameter defined as

$$s = \frac{I}{I_{sat}} = \frac{I}{\frac{\pi hc\gamma}{3\lambda^3}} \tag{5.49}$$

When a transition is saturated ($s >> 1$) , half of the population lives in the excited state and the other half in the ground state. For each of these scattering events the atom gets a photon recoil kick during absorption and another from spontaneous emission. Given that the atom emits along the direction of the wave vector $\mathbf{k}_s$, the change in energy of the atom during such a scattering event is

$$\Delta E = \frac{(m\mathbf{v} + \hbar\mathbf{k} - \hbar\mathbf{k}_s)^2}{2m} - \frac{(m\mathbf{v})^2}{2m} \tag{5.50}$$

$$= \hbar^2\frac{(\mathbf{k} - \mathbf{k}_s)^2}{2m} + \hbar(\mathbf{k} - \mathbf{k}_s).\mathbf{v} \tag{5.51}$$

The total rate of change of energy is then simply a product of the scattering rate and the change in energy, along the principal direction of the trap i

$$\frac{dE_i}{dt} = \Gamma(\omega, \mathbf{v})\Big\langle \hbar k_i v_i + R(f_i + f_{si}) \Big\rangle \tag{5.52}$$

where f_i, f_{si} are the geometrical factors for the incident and scattered photons respectively. For the incident photon, $f_i = \hat{k_i}^2$. For the scattered photon, $f_{si} = P_s(\hat{k_s})\hat{k_s}^2$ with $P_s(\hat{k_s})$ describing the normalized emission pattern. For isotropic emission and scattering, we have $P_s(\hat{k_s}) = 1/4\pi$, $f_{si} = 1/3$ and $\langle \mathbf{k}_s \rangle = 0$ [75].

We average the rate of change of energy over all the velocities assuming that the atom oscillation frequency is much smaller than the radiative linewidth, so $\langle \mathbf{v} \rangle = 0$. We also assume the fact that the Doppler shift is much smaller than the detuning given as $\Delta = \omega - \omega_L$,to obtain the following approximation of Eqn 5.48

$$\Gamma(\omega, \mathbf{v}) = \frac{s\gamma/2}{1 + s + 4\frac{\Delta^2}{\gamma^2}} \left[1 - \frac{8\Delta \mathbf{k.v}}{\gamma^2(1+s) + 4\Delta^2} \right] \tag{5.53}$$

In equilibrium, we can set $\frac{dE_i}{dt} = 0$, $\langle v_i \rangle = 0$ and $\langle v_i v_j \rangle = 0$ for $i \neq j$. This lets us solve for the steady state Doppler cooling energy

$$E_i^D = m\langle v_i^2 \rangle = \frac{\hbar\gamma}{4} \left(1 + \frac{f_{si}}{f_i} \right) \left(\frac{\Delta}{\gamma} + \frac{\gamma(1+s)}{4\Delta} \right) \tag{5.54}$$

$$= \frac{\hbar\gamma}{4} \left(1 + \frac{1}{3\cos^2\theta} \right) \left(\frac{\Delta}{\gamma} + \frac{\gamma(1+s)}{4\Delta} \right) \tag{5.55}$$

One can obtain the Doppler cooling temperature by simply dividing by the Boltzmann constant k_B and we see that this is minimized for low values of s at $\theta = 0$ and $\Delta = \frac{\gamma}{2}$

$$T_{min}^D = \frac{\hbar\gamma}{3k_B} \tag{5.56}$$

We primarily use the transition between $S_{1/2} \leftrightarrow P_{1/2}$ via 493 nm light for Doppler cooling, since it needs only one repumper (650 nm) unlike the $S_{1/2} \leftrightarrow P_{1/2}$ transition. The saturation intensity for this transition is 21.7 mW/cm^2 (0.217 nW/um^2). The Clebsch-Gordon coefficient for the $\Delta m = 0$ transition is $\sqrt{1/3}$ while for the $\Delta m = \pm 1$ transition is $\sqrt{2/3}$. So if we work with only $\sigma^{+/-}$ light, the saturation intensities

get multiplied by a factor of 2/3 resulting in 14.5 mW/cm^2 (0.14 nW/um^2). This shows that dipole transitions typically need a tiny amount of power, ∼100 nW when focused well (10s of micron spot size). In our experiment, we maintain a saturation parameter between 1-2, for all our chambers. We also red de-tune this light by 10 MHz ($\Delta = \gamma/2$) from resonance to obtain good Doppler cooling.

The presence of the low lying D level along with all the Zeeman levels creates a complex Λ system which is not as straightforward as the theory presented for Doppler cooling. Sources [136], suggest that blue and red detuning of the same amount of the 650 nm laser achieve the same Doppler cooling, with maximum cooling power on resonance. Nevertheless, we use the 650 nm light as a re-pumping beam by having a high saturation. In such a case, the job of the 650 nm light is to effectively depopulate the $D_{3/2}$ level at a very high rate so that the electron mostly remains between $S_{1/2} \leftrightarrow D_{3/2}$ and the cooling is done mainly by the 493 nm light.

We also set a magnetic field of roughly 4.1 G, which results in a Zeeman splitting of roughly 12 MHz in the $S_{1/2}$ manifold. To address all Zeeman levels, we use σ^+, σ^- and π transitions as noted earlier. The 493 nm laser beam, set 10 MHz apart, is sent along the direction of the magnetic field with left and right circular polarizations which drive the σ^- and σ^+ transitions, driving $|^2S_{1/2}, m_J = \frac{1}{2}\rangle \leftrightarrow |^2P_{1/2}, m_J = -\frac{1}{2}\rangle$ and $|^2S_{1/2}, m_J = -\frac{1}{2}\rangle \leftrightarrow |^2P_{1/2}, m_J = \frac{1}{2}\rangle$ respectively. To obtain these polarizations, we first combine H and V polarized light coming out of two different fibers onto a polarizing beam splitter, which we send into a quarter wave-plate. The 650 nm light acting as the re-pumper (clearing out the $D_{3/2}$) levels needs to drive all the σ and π transitions. This is achieved by having linearly polarized light at an acute/oblique angle to the magnetic field, such that in the atom's frame of reference we have all the polarizations.

Using such techniques, we are able to get close to the Doppler cooling limit for the trapped ions, which come out as ∼300μK. Initially, during trapping the atomic

ions have a lot of kinetic energy from the fact that they start out hot ($\approx$ 573 K) in the atomic oven. This is why we use a separate trapping beam, which has several hundred μW of 493 nm light with a large detuning of 200 MHz. This helps to cool much faster but equilibrates to a high Doppler temperature. Once we trap, we turn off the trapping beam.

There is also another repumping laser, which is used to clear out the $D_{5/2}$ level. This is mainly used when we populate the $D_{5/2}$ levels, as we will see in the next section. We send about 3-5 uW of 614 nm light parallel to the 650 nm beam for this purpose. Next, we look at the use of different polarizations to prepare the electron in a pure state.

5.2.2 Applications: Optical Pumping

The Zeeman shifts we obtain for a field of 4.1 G, for barium, are approximately 12 MHz at the $S_{1/2}$ levels. We distinguish them by using different polarizations. Optical pumping is a technique where one selectively clears out specific states such that the transition that is not driven is incoherently populated over a specific timescale.

For example, consider the level diagram shown in Fig. 5.2. If one shines σ^+ light on resonance with the transition, over several scattering cycles and some characteristic time depending on the laser powers and frequency detunings, the electronic state will be probabilistically prepared in the edge state. This is because the edge state is untouched by the σ^+ transition while the rest are cleared out by the same. The purity of pumping for such a state is given directly by the purity of polarization. Experimentally, this is tantamount to aligning the beam direction appropriately to the quantization axis. In $^{138}Ba^+$, we typically start our experiment by pumping into $|^2S_{1/2}, m_J = -\frac{1}{2}\rangle$. We do so by turning on σ^- 493 nm light and the 650 nm re-pumper light for several μs, as seen in Fig. 5.3. In this way, we are able to prepare the state deterministically. Our polarizations are aligned to the quantization axis by using the

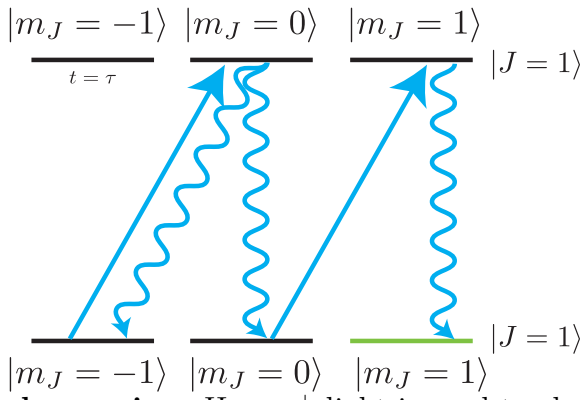

FIGURE 5.2: **Optical pumping:** Here σ^+ light is used to clear out the populations from $|m_J = -1, 0\rangle$ to prepare a pure state in $|m_J = 1\rangle$.

atomic ion as a probe. With the σ^- 493 nm beam and the 650 nm repumper turned on, there should not be any fluorescence from the atom, since it is pumped into a state which does not interact with the laser field (also called a dark state). We look at the fluorescence counts and attempt to minimize it by tuning the magnetic field direction by tweaking a 2 axis current-carrying coil. This lets us align the magnetic field to a precision such that we can pump with >99.5% purity.

5.3 Quadrupole Transitions

Quadrupole transitions occur between states of the same parity. In barium (Ba), quadrupole transitions are particularly relevant for transitions between the long-lived metastable states, such as the S–D transitions. These transitions are central to precision spectroscopy, atomic clocks, and quantum computing applications involving trapped ions [137, 138].

The electric quadrupole moment arises from a non-uniform spatial distribution of the electron charge cloud in an atomic state. Unlike the electric dipole moment, which involves a linear charge displacement, the quadrupole moment describes a second-order spatial distribution, reflecting how electron densities deviate from spherical symmetry. This non-uniformity allows transitions that involve changes in angular momentum states otherwise inaccessible by electric dipole radiation. The interaction

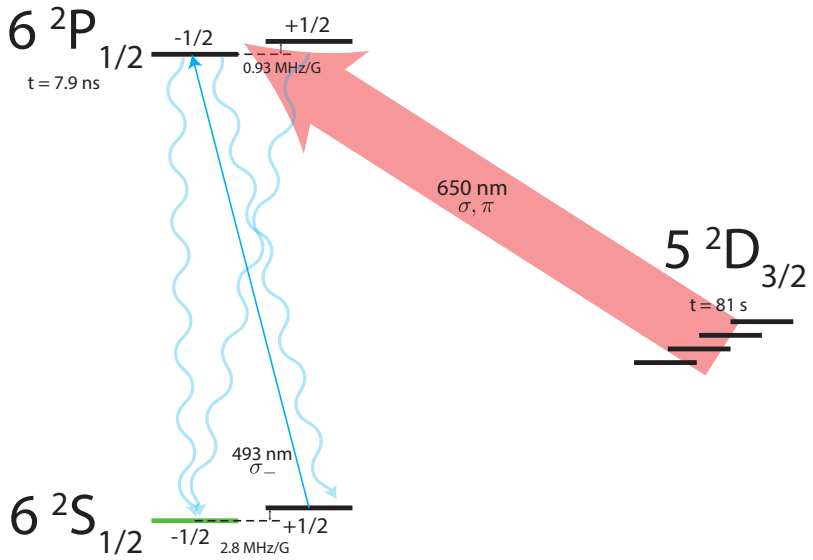

FIGURE 5.3: **Optical pumping in $^{138}Ba^{+}$:** We initialize the state in $|0\rangle = |S_{1/2}, m_J = -1/2\rangle$, by shining 650 nm light containing both σ, π components, and only σ^- 493 nm light. We use ~ 50 μW of 650 nm light and $\sim 50 - 100$ nW of 493 nm light.

Hamiltonian will now contain additional terms

$$H_I = -\mathbf{d} \cdot \mathbf{E} - \frac{1}{6} \sum_{i,j} Q_{ij} \nabla_i E_j \tag{5.57}$$

Here Q_{ij} is the electric quadrupole moment tensor and E_j is the jth component of the electric field. This is further defined as

$$Q_{ij} = q(3x_i x_j - x^2 \delta_{ij}) \tag{5.58}$$

In the dipole approximation, we assumed the electric field to be spatially constant over the atomic wave function. For a higher order approximation, we need to consider how the spatial gradient of the electric field affects the atom, which gives us the quadrupole term. To find the quadrupole transition rate and selection rules, one needs to sandwich the Q_{ij} term in the Hamiltonian between the final and the initial states. One can perform extensive calculations using Winger-Eckert theorem on the

way to find the Rabi frequency for the quadrupole transition as [139]

$$\Omega_0^{QP} = \frac{qE}{\hbar}\sqrt{\frac{15(2j_e+1)\Gamma^{QP}}{4c\alpha k^3}\left|\sum_m \begin{pmatrix} j_e & 2 & k_g \\ m_e & m & m_g \end{pmatrix} \sum_{ij} c_{ij}k_i E_j\right|} \tag{5.59}$$

Here we have the following notations: (j_g, j_e) and (m_e, m_j) are the angular momentum quantum numbers for the ground and the excited state, $\alpha = e^2/4\pi\epsilon_0\hbar c$ is the fine structure constant, k is the wave vector and E is the electric field amplitude. Γ^{QP} is the spontaneous decay rate. The tensor c_{ij} can be found in the reference [140] and the term within the round brackets refer to the Wigner 3-j symbol. The selection rules for the quadrupole transitions read as follows:

$$\Delta J = 0, \pm 1, \pm 2 \qquad J : (0 \nleftrightarrow 1, 2), (1/2 \nleftrightarrow 1/2) \tag{5.60}$$

$$\Delta m_J = 0, \pm 1, \pm 2 \tag{5.61}$$

If we assume a linear polarization for the light field and the magnetic field oriented along the z direction, we assume k and E along the direction given as, and seen in Fig. 5.4

$$k = (\sin(\phi),\ 0,\ \cos(\phi)) \tag{5.62}$$

$$E = (\cos(\gamma)\cos(\phi),\ \sin(\gamma),\ -\cos(\gamma)\sin(\phi)) \tag{5.63}$$

We can also write out the last term of Eqn. 5.59 for different changes in m as follows

$$\Omega_0^{QP}(m, \gamma, \phi) \sim 1/2|\cos(\gamma)\sin(2\phi)| \qquad m = 0 \tag{5.64}$$

$$\sim 1/\sqrt{6}|\cos(\gamma)\cos(2\phi) + i\sin(\gamma)\cos(\phi)| \qquad m = \pm 1 \tag{5.65}$$

$$\sim 1/\sqrt{6}|\cos(\gamma)\sin(2\phi)/2 + i\sin(\gamma)\sin(\phi)| \qquad m = \pm 2 \tag{5.66}$$

We plot these equations in Fig. 5.5 to see how we need to orient the laser k vector and polarization to drive specific transitions.

In $^{138}Ba^+$, the transition between the $S_{1/2}$ ground state and the metastable $D_{5/2}$ state has a wavelength of 1762 nm [101, 141]. The $S_{1/2} \leftrightarrow D_{5/2}$ transition is inherently weak because it involves quadrupole radiation, resulting in a very narrow

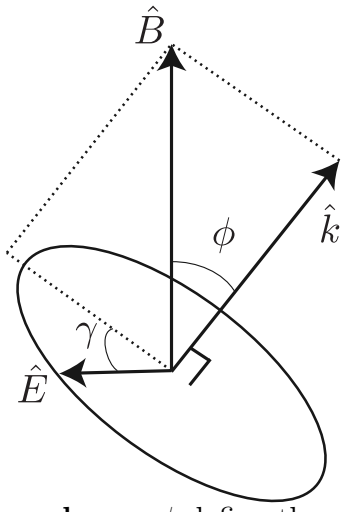

FIGURE 5.4: **Definition of angles:** γ, ϕ define the quadrupole Rabi frequencies. $\hat{k}$ is the propagation direction of the laser, $\hat{E}$ is the electric field polarization, and $\hat{B}$ is the magnetic field direction.

linewidth and a long-lived upper state. Such transitions, despite their low probability, enable precise control and coherence in quantum systems due to minimal spontaneous emission.

Fig. 5.6 shows the quadrupole transitions in $^{138}Ba^{+}$, connecting the S manifold to the $D_{3/2}$ and $D_{5/2}$ manifolds. We drive the 1762 nm transition with an NKT, thulium doped, distributed feedback fiber laser [143]. This light is sent to a fiber amplifier which boosts the power to 450 mW. Since the transition is quite narrow, at 6.1 mHz, we would need to stabilize the laser quite well to drive coherent operations on it. We PDH lock this laser using an ULE hemispherical cavity with a measured finesse of $\approx$ 540000. We measured a linewidth upper bound of 270 Hz based upon comparison of coherence time measurements with another laser.

We split off this laser into three paths and couple them into individual fiber acousto-optic modulators (AOM) for Alice, Bob and Cleo chambers. Each AOM is driven by an RF signal from either a direct digital synthesizer (DDS) or an arbitrary waveform generator (AWG), which provides precise control of the phase along the three optical paths. After the individual AOMs they are sent to the chambers via

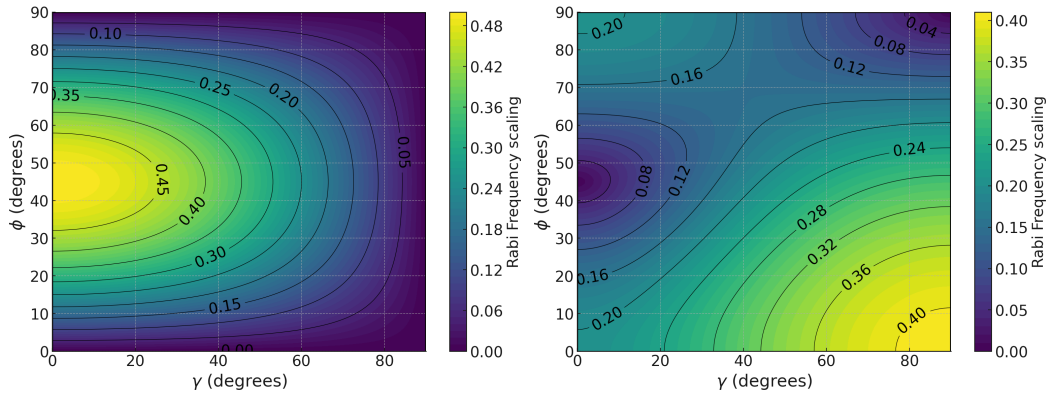

(a) Δm=0 **(b)** Δm=±1

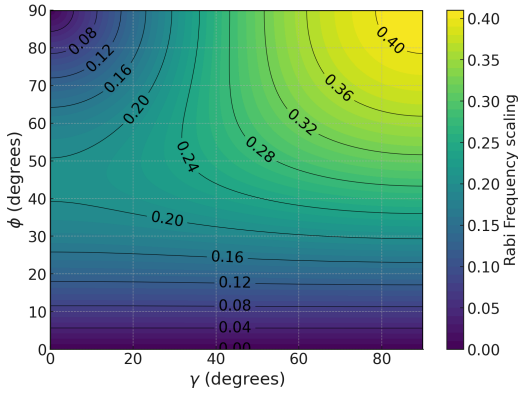

(c) Δm=±2

FIGURE 5.5: **Quadrupole transition strengths:** Corresponding to different angles for ϕ and γ we obtain different Rabi frequencies for transitions with different Δm.

polarization maintaining fibers. In all three systems, approximately 10-20 mW of laser power is focused to a $\approx$ 20 μm waist at the ion. We use a half wave plate and polarizer to send clean polarized light to the atom. Depending on the relative direction of the magnetic field (quantization axis) and the **k** vector of the light, we can drive different carrier transitions as seen in Fig. 5.4 and Fig. 5.5. Specifically, we have used two configurations, $\gamma = 0, \pi/4$. We use this laser for various applications as described in the next sections.

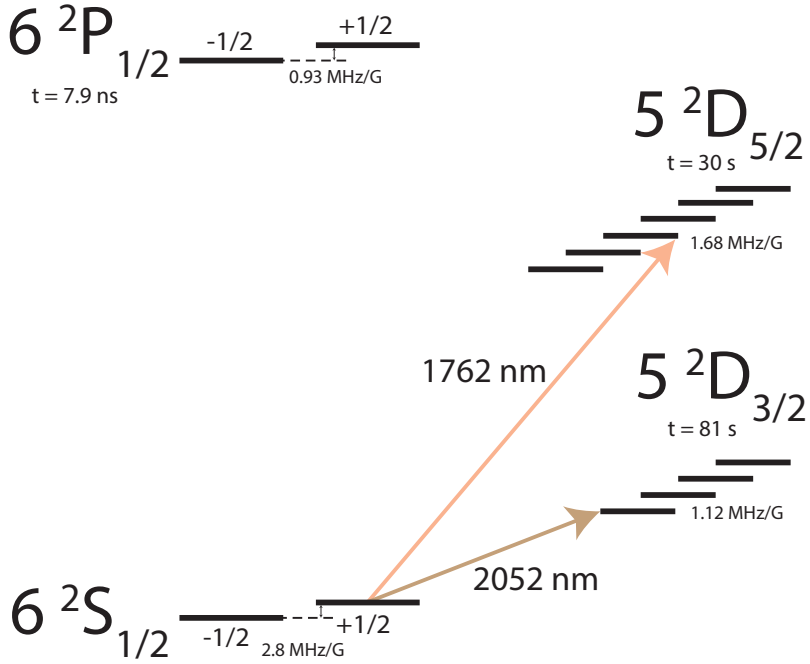

FIGURE 5.6: **Quadrupole transitions of $^{138}Ba^{+}$.** We use the 1762 nm transition heavily, for electron shelving detection, optical qubits, and sideband addressing. We currently do not use 2052 nm in any of our remote entanglement experiments, although potential use cases may be to perform mid circuit readout of stark shifted ancilla qubits [142].

5.3.1 Applications: Single optical qubit gates

Quadrupole transitions can be used to drive single qubit gates. We start by rewriting the interaction for the carrier transition, seen earlier in Eq. 5.25

$$H_I = \frac{\hbar\Omega_0}{2}\left(\sigma_+ e^{i(\delta t+\phi)} + \sigma_- e^{-i(\delta t+\phi)}\right) \tag{5.67}$$

Ω_0 is the quadrupole coupling strength, which in this case is due to the 1762 nm laser intensity (and it's spatial gradient) at the atom. We transform into the drive frame which is given as

$$U(\delta) = |0\rangle\langle 0|\, e^{i\delta t/2} + |1\rangle\langle 1|\, e^{-i\delta t/2} \tag{5.68}$$

The resulting Hamiltonian would then be

$$H_{I_\delta} = \frac{\hbar\delta}{2}\sigma_z + \frac{\hbar\Omega_0}{2}(\sigma_+ e^{i\phi} + \sigma_- e^{-i\phi}) \tag{5.69}$$

The propagator for this Hamiltonian is identified as the propagator for the well-known Rabi oscillation

$$U_I(t) = \begin{pmatrix} \cos(\Omega_\delta t/2) - \frac{i\delta}{\Omega_\delta}\sin(\Omega_\delta t/2) & -i\frac{\Omega}{\Omega_\Delta}\sin(\Omega_\delta t/2)e^{-i\phi} \\ -i\frac{\Omega}{\Omega_\Delta}\sin(\Omega_\delta t/2)e^{+i\phi} & \cos(\Omega_\delta t/2) + \frac{i\delta}{\Omega_\delta}\sin(\Omega_\delta t/2) \end{pmatrix} \tag{5.70}$$

Here we have defined $\Omega_\delta = \sqrt{\Omega_0^2 + \delta^2}$ as the general Rabi frequency. If we associate the two levels, defined earlier as the excited $|e\rangle$ and ground $|g\rangle$ state, with the state vectors

$$|g\rangle = \begin{pmatrix} 1 \\ 0 \end{pmatrix} \tag{5.71}$$

$$|e\rangle = \begin{pmatrix} 0 \\ 1 \end{pmatrix} \tag{5.72}$$

then we can drive resonant transitions with this carrier drive between the states (Rabi oscillations)

$$|\psi(t)\rangle = U_I^\delta(t)\,|0\rangle = \begin{pmatrix} \cos(\Omega_0 t/2) \\ i\sin(\Omega_0 t/2) \end{pmatrix} e^{-i\phi} \tag{5.73}$$

If we look at the probability of finding the atom in the $|0\rangle$ state, we see that it oscillates sinusoidally between the two states with full population transfer happening at the π-time of the drive ($t = \pi/\Omega_0$)

$$P(0) = \cos^2(\Omega_0 t/2) \tag{5.74}$$

We see these oscillations at different detunings in Fig. 5.7. This laser based inter-

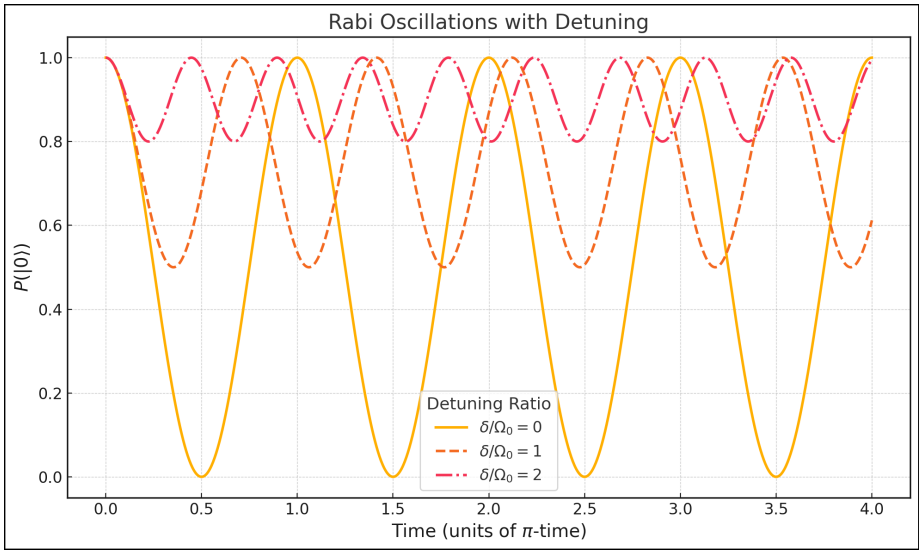

FIGURE 5.7: **Rabi oscillations:** Only during resonance $\delta = 0$, these oscillations transfer populations completely between $|0\rangle \leftrightarrow |1\rangle$. For $\delta > 0$, we have partial state transfer.

action forms the basis of single qubit X and Y gates for quantum computing. The phase and rotation angle are adjusted by setting the duration and phase of the pulse.

The single qubit Z gate corresponds to only a phase change and therefore can be implemented by keeping track of the phase and updating the phase of upcoming X and Y rotations. More generally we can write these as the rotation transformations in the Bloch sphere, given by

$$R(\theta, \phi) = \begin{pmatrix} \cos(\theta/2) & -i\sin(\theta/2)e^{-i\phi} \\ -i\sin(\theta/2)e^{i\phi} & \cos(\theta/2) \end{pmatrix} \tag{5.75}$$

where $\theta = \Omega_0 t$ is the pulse angle and ϕ is the phase of the laser relative to some local oscillator.

5.3.2 Applications: Resolving sidebands

Due to the narrow linewidth of the 1762 laser, we can use it to probe sidebands, as seen in the equations following 5.26. These transitions are suppressed by a factor of η^2, but they help to couple spin with motion. Fig. 5.8 illustrates what these

transitions look like. In this figure, we show some Zeeman levels in the S and D

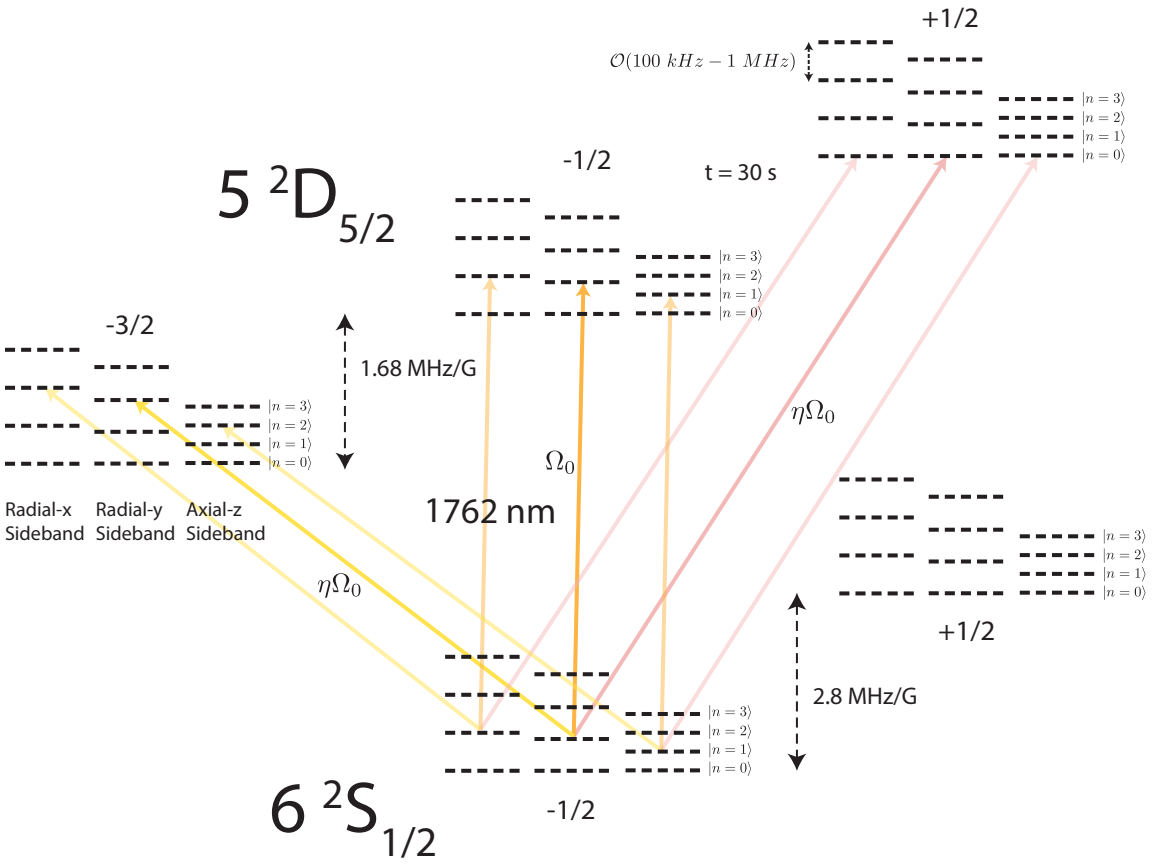

FIGURE 5.8: **Sideband transitions with 1762 nm light:** We show some of the relevant levels that the 1762 beams can address. Each of the Zeeman levels, have sub-levels corresponding to the phononic occupation number along the 3 motional directions (2 radials and 1 axial, assuming there is a single trapped atom.) The sideband transitions are suppressed by a factor of η^2 and change the motional and the spin state together. The motional frequencies in range between 100s of kHz and several MHz.

manifold along with their resolved sidebands. We have not plotted all the Zeeman levels in $D_{5/2}$. This figure is representative of a single trapped $^{138}Ba^+$, in which there are 3 sidebands or bosonic fields, representative of the quantized motion of the atoms moving along the three spatial directions. Our 1762 nm laser helps to drive these transitions, which effectively work as a Jaynes-Cummings model. These transitions can be used for determination of the expected motional occupation number $\bar{n}$ and

consequently the heating rate, $\dot{\bar{n}}$, as well as for cooling below the Doppler limit.

The idea behind measuring $\bar{n}$ is to look at the ratio of blue sideband and red sideband strengths. If the atom is cooled to the motional ground state, then there does not exist a red sideband. If the atom is cooled well and η is small, one can use the relation $\Omega_{rsb}/\Omega_{bsb} = \sqrt{\bar{n}/(\bar{n}+1)}$, along with the observation that transition strength probability P scale as $\sim |\langle f| d.E |i\rangle|^2 \sim \Omega_0^2$, therefore, $P_{rsb}/P_{bsb} = \bar{n}/(\bar{n}+1)$. From here, one can measure $\bar{n}$ at different intervals to determine $\dot{\bar{n}}$. In case the atom has a high $\bar{n}$ (>10), the ratio technique becomes difficult, since this ratio approaches 1 and the relative strengths need to be determined with a higher precision. In such a case, we use a different technique that relies on the the observation that the Rabi frequencies of the transition on the red, blue or carrier sideband at different occupation numbers n are all different. We rewrite an earlier equation for convenience of the reader

$$\Omega_{n+s,n} = \Omega_0 e^{-\eta^2/2} \eta^{|s|} \sqrt{\frac{n_<!}{n_>!} L_{n_<}^{|s|}(\eta^2)}, \qquad L_{n_<}^{|s|}(\eta^2) = \sum_{m=0}^{n_<} (-1)^m \binom{n_< + |s|}{n_< - m} \frac{\eta^{2m}}{m!} \tag{5.76}$$

For carrier and sideband terms, if we choose to keep higher order η terms

$$\Omega_{n+1,n} = \Omega_0 e^{-\eta^2/2} \eta \sqrt{\frac{n!}{(n+1)!} L_n^1(\eta^2)} \tag{5.77}$$

$$= \Omega_0 e^{-\eta^2/2} \eta \sqrt{\frac{L_n(\eta^2)}{(n+1)}} \tag{5.78}$$

$$\Omega_{n,n} = \Omega_0 e^{-\eta^2/2} \sqrt{L_n(\eta^2)} \tag{5.79}$$

$$\Omega_{n-1,n} = \Omega_0 e^{-\eta^2/2} \eta \sqrt{\frac{(n-1)!}{n!} L_n^1(\eta^2)} \tag{5.80}$$

$$= \Omega_0 e^{-\eta^2/2} \eta \sqrt{\frac{L_n^1(\eta^2)}{n}} \tag{5.81}$$

For a given thermal distribution, the probability that the atom is in state n is given

by

$$p_n = \frac{\bar{n}^n}{(\bar{n}+1)^{n+1}} \tag{5.82}$$

Therefore, we can write the carrier Rabi flopping as

$$P(|0\rangle) = \sum_n p_n cos^2\left(\frac{\Omega_0 e^{-\eta^2/2}\sqrt{L_n(\eta^2)}t}{2}\right) \tag{5.83}$$

One can drive these transitions, and fit them by choosing to sum over a finite large number, and therefore obtaining n. A similar process can be carried out by flopping on the blue sideband as well. In the resolved sideband limit, we can also use the red sidebands to successively take out quantas of motion successively. A simple protocol would look as follows

Sideband Cooling

1. Doppler cool and prepare state in spin $|0\rangle = |^2S_{1/2}, m_J = -\frac{1}{2}\rangle$.
2. Drive red sideband of $|D_{5/2}, m = -5/2\rangle$ via 1762.
3. Pump out of the $D_{5/2}$ and $D_{3/2}$ by short pulses, to reduce the number of scattering events and heating.
4. Optically pump with low 493 nm σ^- power.
5. Repeat from step 2, for a total time of cooling on the order of several milli-seconds.

We typically do not use sideband cooling during remote entanglement experiments, since they take a long time. However, we use them to cool to the ground state for taking heating rate measurements. If our atoms exist in a low motional quanta state, it becomes much easier to estimate $\bar{n}$ either by the ratio of blue sideband to red sideband technique or the flopping technique.

5.3.3 Applications: State detection by electron shelving

Perhaps this is the most important application of the quadrupole transition. State discrimination and detection is an important component of trapped ion quantum computing.

A short digression: Before we had the 1762 laser, we were using the Zeeman qubit states $|^2S_{1/2}, m_J = \frac{1}{2}\rangle$ and $|^2S_{1/2}, m_J = -\frac{1}{2}\rangle$. Our state detection relied on selectively shining the atom with σ^+ and σ^-. Only if they are in the correct state, they will scatter on average 2.8 photons. However we collect on average 6-7% of this light, thereby making this scheme slow since we need to rely on statistics by repeating the experiment many number of times. This was the primary motivation to purchase the quadrupole 1762 laser.

In the Zeeman encoding as before, now we can shelve one of the levels, let's say $|^2S_{1/2}, m_J = -\frac{1}{2}\rangle \rightarrow |^2D_{5/2}, m_J = -\frac{1}{2}\rangle$. After this we can simply shine 493 nm (both σ^+ and σ^- polarizations) and 650 nm light, which overall forms a closed cycling transition. Since the $D_{5/2}$ is a metastable state with 30 s lifetime and isolated from 493/650 nm transitions, it will not get affected by the 493/650 nm beams. We collect the resulting fluorescence into photo multiplying tubes (or APDs) via imaging optics and count the number of photons for a given detection time, usually upto 1 ms. If the atom is in the $-1/2$ state, it gets shelved and the atom does not fluoresce while in the other case it does. We alternate preparation of the atoms in both states and look at the photon collection statistics for both.

Based on such a histogram 7.5, we set a discriminating photon number to minimize the overlap between the two distributions. The average photon number obtained during a single experiment is now compared with this discriminator to determine the state of the atom. This gives a way to perform deterministic readout of the atom. The fidelity of this readout is limited by the quality of the shelving pulse and back-

ground scattering into the detector, which ultimately gives a finite overlap between the photon distributions collected from both the states.

5.4 Two photon Raman coupling

The two Zeeman levels in the ground $S_{1/2}$ manifold of $^{138}Ba^{+}$have the same angular momentum $L = 0$, therefore they cannot be driven via single photon dipole transitions. However they can be coupled via two-photon Raman transitions. They have been widely used for engineering an effective two-level system from ground-state sub-levels that lack a convenient direct optical transition [12]. The idea is to drive the ion with two laser fields whose frequency difference, $\omega_1 - \omega_2$ equals the qubit splitting ω_0 (plus any small offset required for sideband addressing, dynamical-decoupling, or 2 qubit gate operations):

$$\omega_1 - \omega_2 = \omega_0 + \mu \tag{5.84}$$

The two arms of the Raman transition are each de-tuned from the nearest dipole coupled level by 10s of THz. Because the individual laser beams are far-detuned, the probability of actually populating this state is vanishingly small. This allows for a powerful theoretical simplification known as adiabatic elimination, to effectively convert a three level system Hamiltonian into two level dyanmics with the effective Rabi frequency

$$\Omega_0 = \frac{E_1 E_2}{4\hbar^2} \sum_{m'} \frac{\langle 0| \mathbf{d}.\hat{E}_1 |m'\rangle \langle m'| \mathbf{d}.\hat{E}_2 |1\rangle}{\Delta} \tag{5.85}$$

Here, $|0\rangle$ and $|1\rangle$ are the qubit states in the Zeeman level, and $|m'\rangle$ is a virtual level through which we couple the two levels. These two components each should have σ^+ or σ^- and π components to effectively deliver a unit of angular momentum required for the transition.

We use a pulsed 532 nm laser with a repetition rate of 120 MHz (taken by modifying an existing Paladin Compact 355-2000) to drive these two photon transitions.

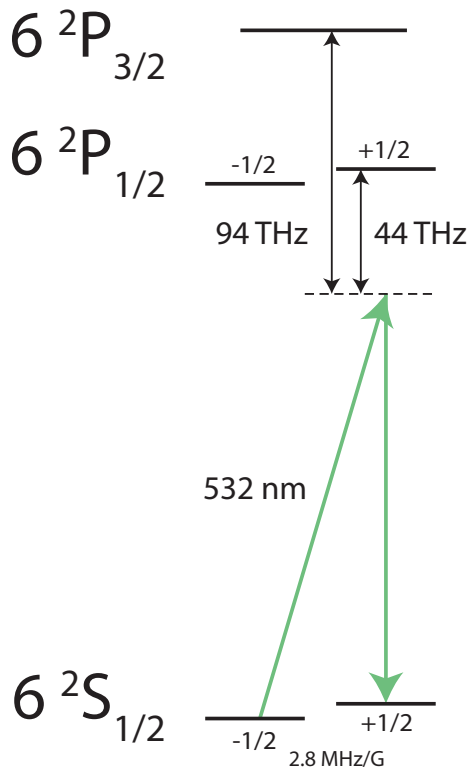

FIGURE 5.9**: Raman based 1Q gates:** 532 nm beams drive single qubit gates in the $S_{1/2}$ levels via Raman transitions. They contain both σ, π light components to drive effectively Δm=$\pm$1. Large detunings of 44 and 94 THz prevent populating the intermediate state.

This qubit splitting in $^{138}Ba^{+}$is small enough ($\sim$ 12 MHz) that it can be bridged directly by sending two frequency tones on the AOM in the Raman beam path. These AOMs, driven by an AWG, provide fast control over the frequency, amplitude, and phase of the light, which in turn defines the parameters of the quantum gate. More specifically, for a single qubit gate implementation via this scheme, the effective rotation angle is given by $\theta = \int \Omega_0(t)dt$ and the phase is set by the differential phase between the two beams.

6

Remote entanglement of trapped atomic ions

This chapter is based on the article

"Fast photon-mediated entanglement of continuously cooled trapped ions for quantum networking" [1, 143].

In this chapter, we discuss the techniques which were used to perform entanglement between remote atoms in physically separated chambers using the polarization degree of freedom in a photon. As we have seen earlier, some of the heralded entanglement techniques rely on having the following conditions [144]:

1. A specific degree of freedom of the atom (usually spin) entangled with a specific degree of freedom of the photon (frequency, time or polarization).
2. Interfering the photons on a beam splitter and erasing the information about the parent emitter of the photon.
3. Detecting single-photon clicks and projecting the atoms into an entangled state.

In the following paragraphs, we describe ideas for performing and heralding remote entanglement. The process starts by exciting an atom to a short-lived state, followed by spontaneous or cavity-mediated emission. These photons, now entangled with specific quantum degrees of freedom of the atom, are collected and routed to a beam splitter. If the photons are indistinguishable, the beam-splitter can erase the origin of the photon wave packet. Additionally, when these photons are detected after the beam splitter in a specific pattern, they post-select the atom's state and leave them entangled. In the following notation, the first ket denotes the state of the first atom

and the second ket denotes the state of the second atom. We explicitly write the tensor product symbol to delineate each atom. A generalized remote entanglement scheme based on two photonic clicks can be summarized in the following steps:

1. Prepare two atom which are to be entangled in a well-defined quantum state $|\Psi_1\rangle \otimes |\Psi_2\rangle$.
2. Excite both atoms to a short lived state $|\Psi_i \rightarrow e_i\rangle$.

$$|\Psi\rangle = |e_1\rangle \otimes |e_2\rangle \tag{6.1}$$

3. Collect photon emission (ν_i) from each atom. Assume that the atom, starting from the state $|e_1, e_2\rangle$ can decay into two different atomic states (ϕ_1, ϕ_2). Since the emission conserves angular momentum and energy , and if we are able to perfectly track the states of the atom and the photon, the resulting pair would be perfectly correlated i.e. entangled. These collected atom-photon pairs are then directed into each port of a beam splitter, denoted by the subscript (A,B)

$$\begin{aligned}
|\Psi\rangle &= (|\phi_1, \nu_1\rangle + |\phi_2, \nu_2\rangle)_A \otimes (|\phi_1, \nu_1\rangle + |\phi_2, \nu_2\rangle)_B \\
&= (a^\dagger_{A,\nu 1} |\phi_1\rangle + a^\dagger_{A,\nu 2} |\phi_2\rangle) \otimes (a^\dagger_{B,\nu 1} |\phi_1\rangle + a^\dagger_{B,\nu 2} |\phi_2\rangle) \\
&= a^\dagger_{A,\nu 1} a^\dagger_{B,\nu 1} |\phi_1\rangle \otimes |\phi_1\rangle + a^\dagger_{A,\nu 1} a^\dagger_{B,\nu 2} |\phi_1\rangle \otimes |\phi_2\rangle \\
&+ a^\dagger_{A,\nu 2} a^\dagger_{B,\nu 1} |\phi_2\rangle \otimes |\phi_1\rangle + a^\dagger_{A,\nu 2} a^\dagger_{B,\nu 2} |\phi_2\rangle \otimes |\phi_2\rangle
\end{aligned} \tag{6.2}$$

Here ν_1, ν_2 refers to the emitted photon's two degrees of freedom. The subscripts (A,B) refer to the two different ports of a beam splitter also labeled as (A,B). $a^\dagger_{A,\nu 1}$ represents the creation of a photon in port A with the photonic

state ν_1 Now, note that Eqn 6.2 can be refactored as follows:

$$\begin{aligned}|\Psi\rangle = \frac{1}{\sqrt{2}}\Big((a^\dagger_{A,\nu1}a^\dagger_{B,\nu1} + a^\dagger_{A,\nu2}a^\dagger_{B,\nu2})(|\phi_1\rangle\otimes|\phi_1\rangle + |\phi_2\rangle\otimes|\phi_2\rangle)\\ +(a^\dagger_{A,\nu1}a^\dagger_{B,\nu1} - a^\dagger_{A,\nu2}a^\dagger_{B,\nu2})(|\phi_1\rangle\otimes|\phi_1\rangle - |\phi_2\rangle\otimes|\phi_2\rangle)\\ +(a^\dagger_{A,\nu1}a^\dagger_{B,\nu2} + a^\dagger_{A,\nu2}a^\dagger_{B,\nu1})(|\phi_1\rangle\otimes|\phi_2\rangle + |\phi_2\rangle\otimes|\phi_1\rangle)\\ +(a^\dagger_{A,\nu1}a^\dagger_{B,\nu2} - a^\dagger_{A,\nu2}a^\dagger_{B,\nu1})(|\phi_1\rangle\otimes|\phi_2\rangle - |\phi_2\rangle\otimes|\phi_1\rangle)\Big)\end{aligned} \tag{6.3}$$

In Eqn 6.7, we readily recognize that each term of the atoms-photon pair are Bell states. This means that if we can measure the photons in a Bell basis, we can herald the atoms in an entangled state.

4. Use a beam-splitter along with appropriate photonic detectors to perform a Bell-basis measurement. Here the beam splitter transformation is given by $a^\dagger_A \rightarrow \frac{a^\dagger_C + a^\dagger_D}{\sqrt{2}}; a^\dagger_B \rightarrow \frac{a^\dagger_C - a^\dagger_D}{\sqrt{2}}$. Now we can write transformed state as follows:

$$\begin{aligned}|\Psi\rangle = \frac{1}{2}\Big((a^{\dagger 2}_{C,\nu1} + a^{\dagger 2}_{C,\nu2} - a^{\dagger 2}_{D,\nu1} - a^{\dagger 2}_{D,\nu2})(|\phi_1,\phi_1\rangle + |\phi_2,\phi_2\rangle)\\ +(a^{\dagger 2}_{C,\nu1} - a^{\dagger 2}_{C,\nu2} - a^{\dagger 2}_{D,\nu1} + a^{\dagger 2}_{D,\nu2})(|\phi_1,\phi_1\rangle - |\phi_2,\phi_2\rangle)\\ +2(a^\dagger_{C,\nu1}a^\dagger_{C,\nu2} - a^\dagger_{D,\nu1}a^\dagger_{D,\nu2})(|\phi_1,\phi_2\rangle + |\phi_2,\phi_1\rangle)\\ +2(a^\dagger_{C,\nu2}a^\dagger_{D,\nu1} - a^\dagger_{C,\nu1}a^\dagger_{D,\nu2})(|\phi_1,\phi_2\rangle - |\phi_2,\phi_1\rangle)\Big)\end{aligned} \tag{6.4}$$

The first two terms arise from Hong-Ou Mandel interference [145]. Two indistinguishable photons coming into the same mode of a beam splitter always exit out of the same modes in the splitter. In most cases, we are not able to detect two indistinguishable photons coming in at the same time. However, we can very easily detect photons when they come out on the opposite exit modes or ports, or when two different photons come out of the same port. In such a case, the atoms get entangled in a state of the form $|\phi_1,\phi_2\rangle \pm |\phi_2,\phi_1\rangle$.

To herald states of the form $|\phi_1,\phi_1\rangle \pm |\phi_2,\phi_2\rangle$, we simply perform the measurement in a different basis. For example, we can use a transformation which mixes

the two photonic states together $a^\dagger_{\nu 1}/a^\dagger_{\nu 2} \rightarrow \frac{a^\dagger_{\nu 1}+a^\dagger_{\nu 2}}{\sqrt{2}}/\frac{a^\dagger_{\nu 1}-a^\dagger_{\nu 2}}{\sqrt{2}}$, before using a photon distinguishing beam splitter. Usually, the atomic state is encoded in the spin degree of freedom, so $|\Psi\rangle = \alpha\,|0\rangle + \beta\,|1\rangle$. For photons, we have the choice of using different encoding schemes as already discussed in Chapter 2. We start by choosing polarization as the preferred degree of freedom since passive linear optical components like wave plates and polarizers can be used to easily control the polarization state. The next few sections are taken from the paper [1] and are intended to motivate the need to consider other forms of photonic encoding instead of polarization. They are written in a summarized fashion and we refer the reader to [143] for a much more detailed description.

6.1 Polarization encoding: The Good and the Bad

Atoms naturally emit light of specific polarization, which makes the polarization scheme quite attractive. In our case, we use a singly ionized barium atom to emit single photons of different polarizations. The figure 6.1 shows the relevant excited state of $^{138}Ba^+$and its two possible decay channels. They carry either no angular momentum, corresponding to a π transition, or one unit angular momentum, corresponding to a σ transition. Accounting for the appropriate coupling strengths corresponding to the two decay channels, we can write out the joint atom-photon state as:

$$\Psi_{atom-photon} = \sqrt{\frac{2}{3}}\,|0\sigma^+\rangle + \sqrt{\frac{1}{3}}\,|1\pi\rangle \tag{6.5}$$

Now, if one collects these single photons perpendicular to the magnetic field into a single mode fiber, these specific light fields uniquely map to its orthogonal polarization state such that the Clebsch-Gordan coefficients cancel out in exactly the opposite way to yield a perfectly balanced maximal atom-photon entangled state [146, 147]. This is due to the fact that we can write the polarization of the emitted photons as: $|\mathbf{k}_\pi\rangle = -\sin(\theta)\,|\hat{\theta}\rangle$ and $|\mathbf{k}_\sigma\rangle = e^{i\phi}/\sqrt{2}(\cos\theta)\,|\hat{\theta}\rangle + i\,|\hat{\phi}\rangle)$, and the additional $\sqrt{2}$ factor

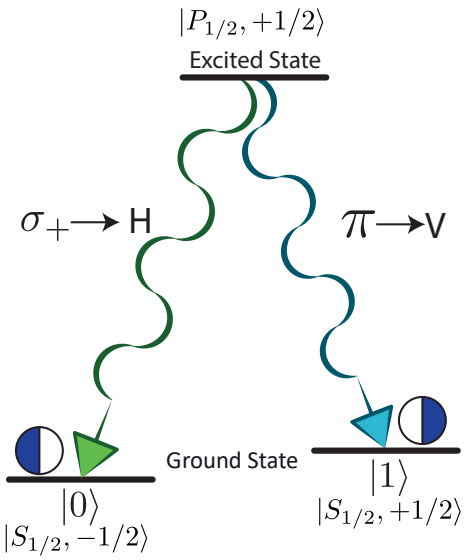

FIGURE 6.1: **Polarization encoding:** The excited state after decay can emit a σ or a π photon conditional on the state that it ends up in. This generates atom-photon entanglement.

from the σ polarization cancels out the Clebsch-Gordon coefficient.

$$\Psi_{atom-photon} = \sqrt{\frac{1}{2}}\,|0H\rangle + \sqrt{\frac{1}{2}}\,|1V\rangle \tag{6.6}$$

.

Now, if we collect two such photons from two atoms and interfere on the beam splitter, we can follow the same treatment as we did before in Eqn 6.7, keeping in mind that $\{\nu_1, \nu_2\} \rightarrow \{H, V\}$ and $\{\phi_1, \phi_2\} \rightarrow \{|0\rangle, |1\rangle\}$. Given this state mapping, Eqn 6.7 can be written as:

$$\begin{aligned}|\Psi\rangle = \frac{1}{2}\Big(&(|H_C, H_C\rangle + |V_C, V_C\rangle - |H_D, H_D\rangle - |V_D, V_D\rangle)(|00\rangle + |11\rangle)\rangle \\ &+(|H_C, H_C\rangle - |V_C, V_C\rangle - |H_D, H_D\rangle + |V_D, V_D\rangle)(|00\rangle - |11\rangle) \\ &+2(|H_C, V_C\rangle - |H_D, V_D\rangle)(|01\rangle + |10\rangle) \\ &+2(|H_C, V_D\rangle - |H_D, V_C\rangle)(|01\rangle - |10\rangle)\Big)\end{aligned} \tag{6.7}$$

So if we use a polarizer after the beam splitter, and detect two photons of different

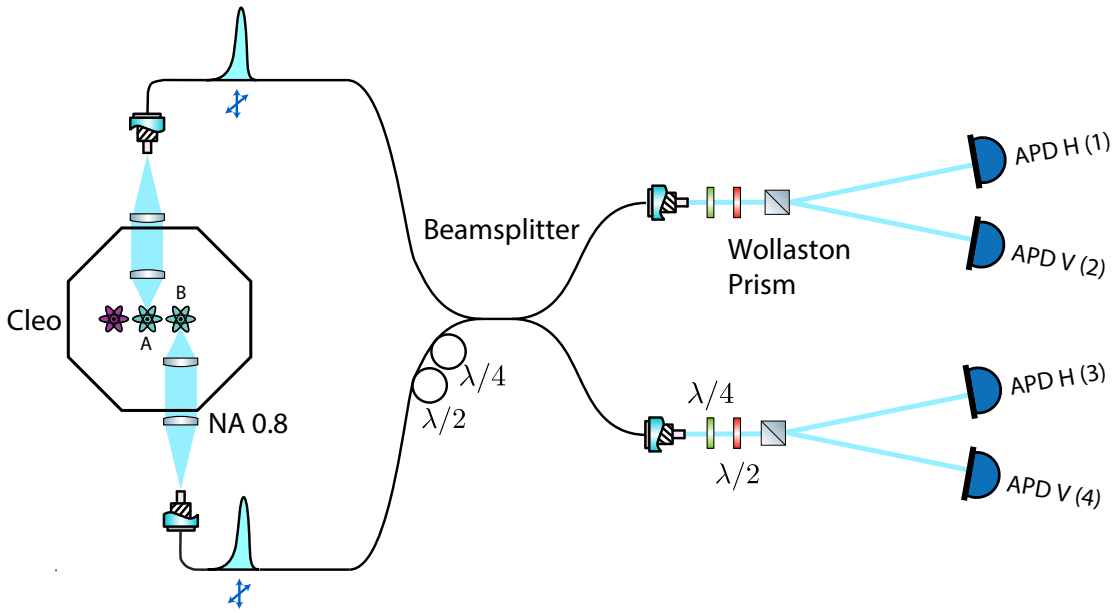

FIGURE 6.2: **Experimental setup for performing remote entanglement between two co-trapped $^{138}Ba^{+}$atoms in Cleo.** Two in-vacuum aspheres collimate light emitted from two co-trapped atoms. An out-of-vacuum asphere couples this light into the two ports of a fiber beam splitter. One fiber arm of the splitter contains fiber paddles acting as waveplates to compensate for the relative birefringence difference between the two input ports. At the output ports we have the Bell state analyzer consisting of waveplates, prisms and avalanche photodiodes to measure single photons in any polarization basis.

polarizations, we will herald Bell states represented by the last two terms in the Eq. 6.7, $|\Psi\rangle = |01\rangle \pm |10\rangle$.

We perform such an experiment in our recently built Cleo system featuring state-of-the-art light collection from atoms via the use of in-vacua high NA (0.8) asphere [148]. Our objective was to obtain the highest rate of entanglement of atoms using polarization-encoded photons. For this purpose, we used the two in-vacuum aspheres of Cleo to collect single photons from two co-trapped barium-138 atoms. Each asphere was aligned to collect single photons from one of the two atoms. The field of view is sufficiently small to have negligible cross fiber coupling. Fig 6.2 shows the experimental setup and the protocol.

Protocol: Polarization Entanglement

1. Using optical pumping with 493 nm σ^- and 650 nm light, prepare each atom in $|^2S_{1/2}, m_J = -\frac{1}{2}\rangle$.
2. Excite atom with a 3 picosecond, σ^+ polarized 493 nm pulse to $|^2P_{1/2}, m_J = \frac{1}{2}\rangle$
3. The excited state has a lifetime of ∼8 ns. Using the aspheres, collect single photons into the two ports of a fiber beam splitter.
4. Detect two orthogonally polarized photon clicks after the beam splitters. The click patterns and the states are given as in Table 6.1.

Table 6.1: Heralding click pattern

APD Clicks	Atom state
(1,2) or (3,4)	$\|\Psi^-\rangle = \frac{1}{\sqrt{2}}(\|01\rangle - \|10\rangle)$
(1,3) or (2,4)	$\|\Psi^+\rangle = \frac{1}{\sqrt{2}}(\|01\rangle + \|10\rangle)$

Before we proceed to atom-atom entanglement, we first characterize the atom-photon state. This is performed by doing a joint state detection of the atom and the photon in different basis. We take correlations by detecting the state of the atom and detecting the photons in {H,V} polarization basis. For an ideal correlation, turning the polarization state of the photon would concurrently turn the atomic state. Using quarter and half waveplates after the beam splitter, we change the polarization of the photons, which are then detected by avalanche photo-diodes in (H,V) basis by using high extinction ratio polarizing beam splitters. Immediately after, we detect the atomic state via state selective fluorescence as described in Chapter 5. We also perform "coherence" measurements by detecting the photons in the $|H + V\rangle/\sqrt{2}, |H - V\rangle/\sqrt{2}$ basis followed by detecting the state of the ion after a 532 nm $\pi/2$ analysis pulse with a phase that we scan. The coherence measure-

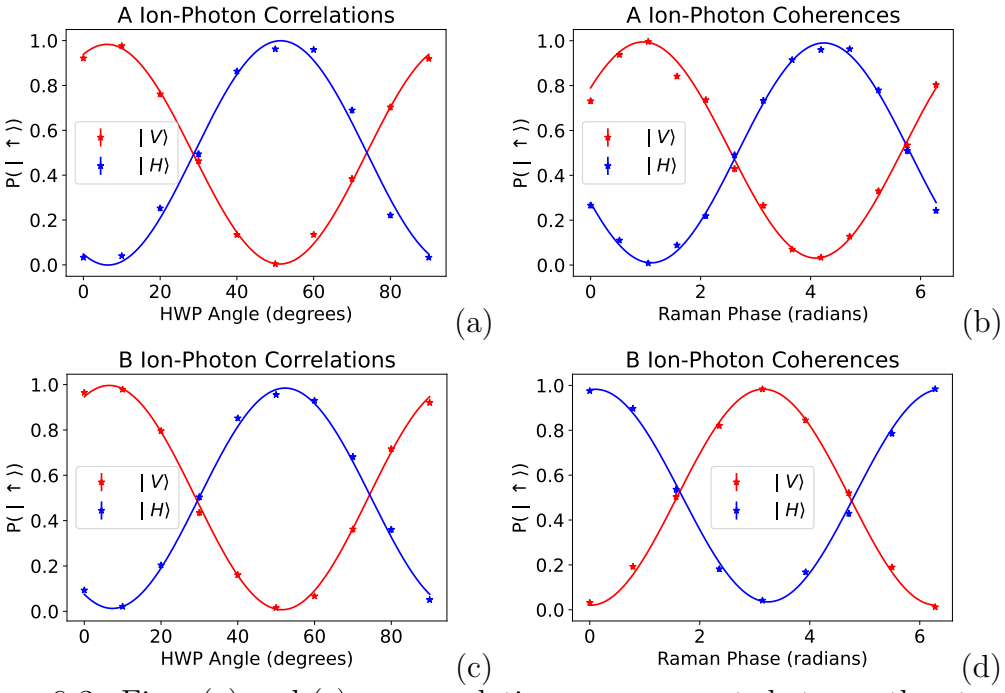

FIGURE 6.3: Figs. (a) and (c) are correlation measurements between the atom and the photon states as the half waveplate is turned. They are fitted via non-linear least squares fitting using offset sinusoidal functions resulting in fitted contrasts of: (a) $0.979^{+0.009}_{-0.009}$ red, $1.00^{+0.0}_{-0.03}$ blue and (c) $0.989^{+0.011}_{-0.011}$ red, $0.972^{+0.017}_{-0.017}$ blue. Figs. (b) and (d) measure the atom state after a $\pi/2$ Raman pulse with variable phase ϕ conditioned on measuring the photons in the diagonal basis. Least squares fitting for the plots on the left give fitted contrasts of (b) $0.964^{+0.013}_{-0.013}$ red, $0.98^{+0.012}_{-0.012}$ blue and (d) $0.963^{+0.01}_{-0.01}$ red, $0.948^{+0.013}_{-0.013}$ blue.

ments are performed with the photon collected in a short window of 3 ns to avoid unwanted phase evolution of the atom-photon state after the spontaneous emission of the photon. These measurements, known as correlations and coherences, help in bounding the ion-photon fidelity. The ion-photon fidelity bounds are calculated to be $99.1(1.0)\% > F_A > 98.1(1.4)\%$ and $99.1(0.7)\% > F_B > 96.8(0.6)\%$ [143].

6.1.1 Entanglement rate: The Good

Once the atom-photon states are characterized, we proceed to generate Bell states of the atoms. Photon detection according to 6.1 projects the atoms into the corresponding Bell states, and are consequently analyzed by relevant analysis pulses and

atom state detections. Since we collect photons using a state-of-the-art, in-vacuum, 0.8 NA asphere, we were able to obtain the highest entanglement rate ever across quantum memories in any platform mediated by photons.

We can calculate the obtained entanglement rate as $R = \frac{1}{2} f p_A p_B$ where f is the frequency at which we attempt entanglement generation, and p_A, p_B are the probabilities that single photons emitted from each atom A, B are collected and detected. A complete cycle of the protocol given earlier takes 1 µs, so our attempt rate is 1 MHz. However, each time these atoms absorb and emit a single photon, they undergo recoil, and over many tries they start heating up roughly at the rate of 0.1 quanta per attempt. Photon-recoil induced heating is a problem, since fiber coupling drops drastically and the rate suffers even more. We circumvent this by co-trapping an $^{171}Yb^{+}$atom and use it for continuous sympathetic cooling, so that we can perform uninterrupted entanglement attempts at $f = 1MHz$.

The probability of light collection gets reduced by a variety of losses at each step of the process. For this experiment, we pumped and excited with a probability of 96(2)%. 493 nm photons are emitted 73% of the time of which we collect 19.5% (with a rod clipping of 3%) along with a 90% optical transmission loss through the asphere. 30% of these collected photons are fiber coupled which are then detected with a 71% detection efficiency by our APDs. This gives a net success probability of 2.5(3)%, but we observe slightly lower numbers which we attribute to additional surface losses from collection optics and variations in fiber coupling during the experiment. For our system we get, p_A and p_B as 2.3(1)% and 2.2(1)% respectively, for a net entanglement rate R = 250 s^{-1}.

This is exactly why polarization encoded photons are good: it is easy to generate atom-photon entangled pairs by simply exciting an atom and looking at different decay paths with different selection rules to give photons of different polarizations. Short decay times of nanoseconds along with simultaneous emission of horizontally

and vertically polarized photons, along with their easy manipulation make it a great choice for having high rates of entanglement.

6.1.2 Entanglement fidelity: The Bad

We can perform ion-ion measurements to bound the fidelity of the entangled state. First, we look at the phase of the joint state:

$$|\Psi\rangle = \left(|0H\rangle + e^{i(k_H x_H - k_V x_V)}|1V\rangle\right) \otimes \left(|0H\rangle + e^{i(k'_H x'_H - k'_V x'_V)}|1V\rangle\right) \tag{6.8}$$

Now we make the following reasonable assumptions:

- The wavenumbers for the two H photons are approximately the same for the two atoms i.e. $k_H \approx k'_H$. This is because the magnetic field difference between the two atoms is small $\sim$ 1kHz.
- The difference in path lengths of the photons emitted by two different atoms is the same for both polarizations i.e. $x_H - x'_H \approx x_V - x'_V$. This is because the birefringence of standard fibers are $\approx 10^{-7}$. This makes the approximation correct to 10^{-7}.

We know that the terms that matter in Eq. 6.7 have two photons of different polarizations, so we want to look at the terms with photons of polarization $|H, V\rangle$ or $|V, H\rangle$. This along with the assumptions before makes the effective phase difference due to photon propagation as:

$$|\Psi\rangle \propto |01\rangle \pm e^{i\Delta k \Delta x}|10\rangle \tag{6.9}$$

We compute this term to be $\sim 2\times10^{-9}$, which can be safely ignored. In addition to these, there is a time-dependent phase in the Bell state due to the magnetic field difference. This is because the energy splitting between $|01\rangle$ and $|10\rangle$ is proportional to the magnetic field difference between the two atoms. This phase evolution starts after the second photon detection. Due to this, all common mode magnetic field noise is canceled out and it is expected to have a longer coherence time than two

uncorrelated Zeeman qubits. Indeed, we measured an extended Bell state coherence time of 38(13) ms.

Since we entangle atoms which are co-trapped and our laser systems cannot individually address them, we can only perform global operations on our atomic qubits. This restricts us to only being able to bound our entanglement fidelity. We use population measurements and parity scans to identify these bounds. Akin to the atom-photon correlation, atom-atom populations are joint measurements of the state of the atom. The parity of the two-atom state reflects the probability of the atoms' spins being aligned or anti-aligned and is defined as:

$$P = p_{00} + p_{11} - p_{01} - p_{10} \tag{6.10}$$

where each of the p_{ij} denotes the probability of the two atoms to be in the i,j th state respectively. We perform our parity scans on the Bell states $|01\rangle \pm |10\rangle$. A global analysis $\pi/2$ pulse with zero phase converts

$$|01\rangle + |10\rangle \longrightarrow |00\rangle - |11\rangle,$$

while leaving

$$|01\rangle - |10\rangle$$

unchanged. A second $\pi/2$ pulse with phase ϕ then implements

$$|01\rangle + |10\rangle \longrightarrow -\cos\phi\,(|01\rangle + |10\rangle) + \sin\phi\,(|00\rangle e^{-i\phi} - |11\rangle e^{i\phi}).$$

By measuring the parity observable in Eq. 6.10 as we scan ϕ, we observe that $|01\rangle - |10\rangle$ has a constant parity $P = +1$, whereas $|01\rangle + |10\rangle$ oscillates between $+1$ and -1. Together with the population data, these parity scans establish a lower bound on our fidelity of $> 93.7(1.3)\%$ [149].

There are a variety of error sources that limited this experiment to a lower fidelity. The two entangled ions have a coherence time of 32 ms due to suppression of

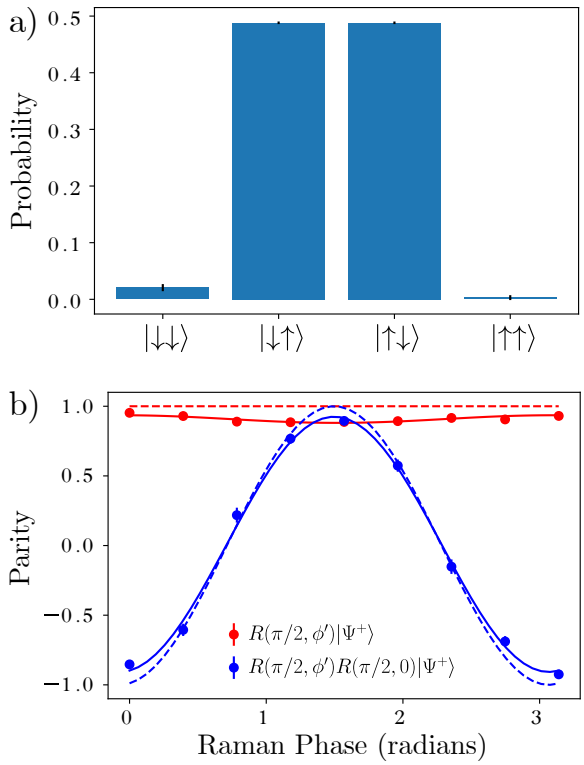

FIGURE 6.4: The top figure shows the population of the atoms among all the spin states, which are $|\downarrow\downarrow\rangle \equiv |00\rangle, |\downarrow\uparrow\rangle \equiv |01\rangle, |\uparrow\downarrow\rangle \equiv |10\rangle, |\uparrow\uparrow\rangle \equiv |11\rangle$. The bottom figure shows parity scans for the Bell state $|01\rangle + |10\rangle$. The red curve is scanning the phase of a single $\pi/2$ pulse while the blue curve is scanning the phase of a $\pi/2$ pulse after a $\pi/2$ rotation with zero phase. The blue data points are fit to a sinusoid using least squares technique which gives a fitted contrast of 0.925(0.017) while the red data points give a fitted contrast of 0.027(0.018).

common-mode noise, which corresponds to an error of 0.3(1)%. There are additional small error sources as well; for example, temporal mismatch of the photons, double excitation of the atom, dark count on the detector, and imperfect beam splitter (49:51 in-fiber beam splitting) which contributes to net error <0.25(2)%. However, the most important point is to realize that the bulk of the errors come from an imperfect ion-photon state, contributing about 2.9(1.6)% error. This error is calculated by considering ion-photon correlation measurements. We hypothesize that some of this error comes from the polarization channel which we do not completely understand, for more details see [149].

As the photon passes through the fiber, we obtain non-trivial time-varying unitary transformations which impart a relative phase between the Bell states. This can be tracked and compensated for by performing polarization rotations using wave plates just before detecting the single photons. However, there are atleast two specific cases in our experimental system which can cause unavoidable polarization induced fidelity losses.

1. If the light collection into the fiber is not performed exactly in the plane perpendicular to the magnetic field, then the preferred mapping of polarizations i.e. $|\sigma^+\rangle \rightarrow |H\rangle$ and $|\pi\rangle \rightarrow |V\rangle$ does not hold true anymore. This leads to polarization mixing errors and directly impacts the atom-photon entanglement fidelity.
2. The emitted photon has to travel through the vacuum window before it gets collected into the fiber. If the window's birefringence varies across its surface, the desired polarization mapping can fail: a photon traveling through different spots on the window experiences different polarization rotations. When integrated over the entire window, this can cause irrecoverable fidelity loss since we are tracing out the photon's polarization state at the end. The window's spatial retardance was measured to be small before it was installed, on the order of 10^{-1} degrees as seen and described in Fig. 6.5 and this does not completely account for the 2.9% error we attribute to the ion photon state infidelity. However, it may be possible that clamping the windows onto the vacuum chamber causes stress induced birefringence which causes the afore-mentioned effects [150].

While it is possible to fix or reduce errors from misalignment by performing atom-photon correlations and doing iterative adjustments on the photon collection imaging system, it is challenging to fix polarization scrambling from the vacuum windows. A possible solution may be to map the birefringence of the mounted window and use a

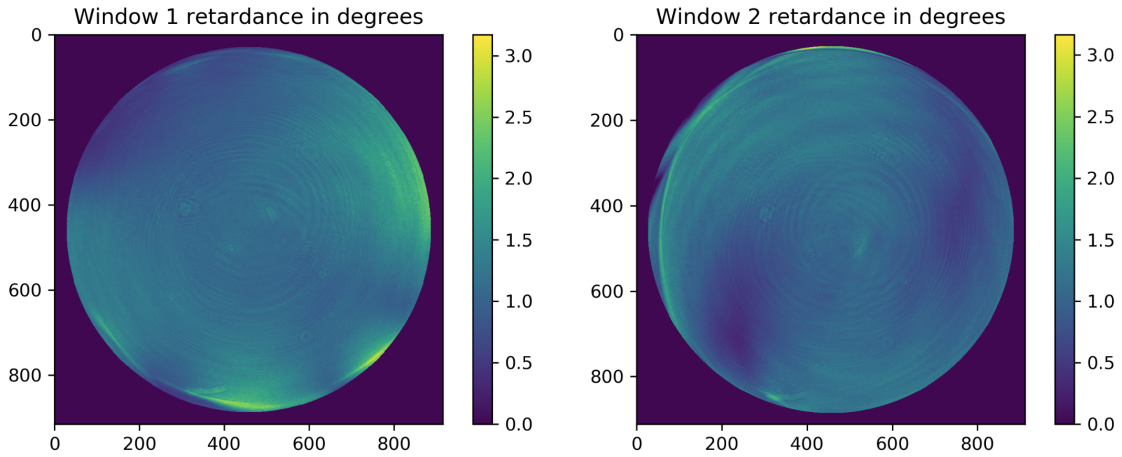

FIGURE 6.5: **Window birefringence measurement:** The retardance in degrees is plotted as a function of the pixel coordinates. When the windows were not mounted, we measured an average window retardance of 0.6 and 0.5 degrees respectively. This measurement was performed by placing the window between two crossed polarizers and shining a large 493 nm beam to cover the entire window. The image was then analyzed using Jones calculus formalism to calculate the retardances.

custom metasurface optic to cancel that out [151]. Another option would be to choose a different material for the glass window with lower stress induced birefringence, for example SF-57 [152]. The final option is to choose a different photon encoding scheme which is insensitive to these errors. We can use frequency encoding which is usually resistant to group velocity dispersion as it passes through the glass medium, but that may introduce small timing issues [51]. We can also use time-bin encoding which encodes information in the timing of a fixed polarization photon pulse. This would allow us to filter out wrong polarizations to obtain a higher fidelity at the cost of a rate trade-off. In the context of a long-distance quantum network, using polarization encoding means there will be a need to perform frequent polarization calibration which can limit the connectivity rate of the quantum network [153]. For that reason, we study an encoding scheme of using time-binned photons in the next chapter. We will talk about our results from time-bin mediated entanglement experiments which

circumvent polarization errors and offer a path to higher fidelities.

7

Time-bin mediated remote entanglement

This chapter is based on the articles:
"High-fidelity remote entanglement of trapped atoms mediated by time-bin photons" and *"Entanglement fidelity limits of photonically-networked atomic qubits from recoil and timing"* [154, 155].

The technique of using the photon's time degree of freedom for remote entanglement purposes was first suggested by Barett and Kok [48] and has been demonstrated in solid state quantum memories [108, 156, 157]. The scheme relies on the existence of an excited state which couples strongly to only one of the qubit states. Unlike in the polarization scheme where we had simultaneous spontaneous decay which generated two photons at the same time, here the atom is excited twice, thereby having two windows of time where the photon can be emitted, thus the *time-binned* photons. At the same time, this scheme is akin to the polarization case, in a sense that it also relies on double heralding which makes it resistant to most experimental error sources [158]. Assuming the excited state only decays to the $|0\rangle$ level, the protocol below shows the steps required for generating time-bin entanglement with the spin-state of the photon.

Protocol: Time-Bin Entanglement Generation

1. Initialize qubits in $|0\rangle$ state.
2. Apply Hadamard gates to create superposition $(|0\rangle + |1\rangle)/\sqrt{2}$.
3. Apply excitation pulse to transfer $|0\rangle$ to a short lived state $|e\rangle$.
4. Collect any spontaneous emission.
5. Swap populations between $|0\rangle \leftrightarrow |1\rangle$ using a π pulse.
6. Excite $|0\rangle$ to $|e\rangle$ again and collect emission.

7.1 Atomic level structure for time-bins

We are now concerned with an encoding scheme in $^{138}Ba^{+}$that permits the Barrett-Kok protocol. Fig. 7.1 shows the level structure of $^{138}Ba^{+}$. If we had the ability to image 455 nm photons, it would be appropriate to use one of the edge Zeeman states in $P_{3/2}$ as the excited state, since they decay only to a specific Zeeman level in $S_{1/2}$ due to polarization selection rule. Since our imaging system and photon collection optics are optimized to operate at 493 nm, the excited state is chosen to be $|e\rangle = |^2P_{1/2}, m_J = \frac{1}{2}\rangle$.

We use an optical qubit with the qubit states defined as $|0\rangle = |^2S_{1/2}, m_J = -\frac{1}{2}\rangle$ and $|1\rangle = |^2D_{5/2}, m_J = -\frac{1}{2}\rangle$ [159]. Our narrow-linewidth 1762 nm laser drives coherent operations between the $|0\rangle$ and the $|1\rangle$ states. Such an encoding satisfies Barrett-Kok's requirement, since the excited state does not couple to the $|1\rangle$ state [48]. The excited state $|^2P_{1/2}, m_J = \frac{1}{2}\rangle$ has two decay pathways emitting a σ or a π photon as we had seen earlier in the polarization encoding scheme. The branching ratio to the $S_{1/2}$ manifold is 73%. In addition 2/3 of these decays return the population to $|0\rangle_q$ for a net branching ratio of $\beta = 49\%$. We reject events with decays to the other ground state ($|^2S_{1/2}, m_J = +1/2\rangle$) via a π-polarized photon with a polarization filter, as seen

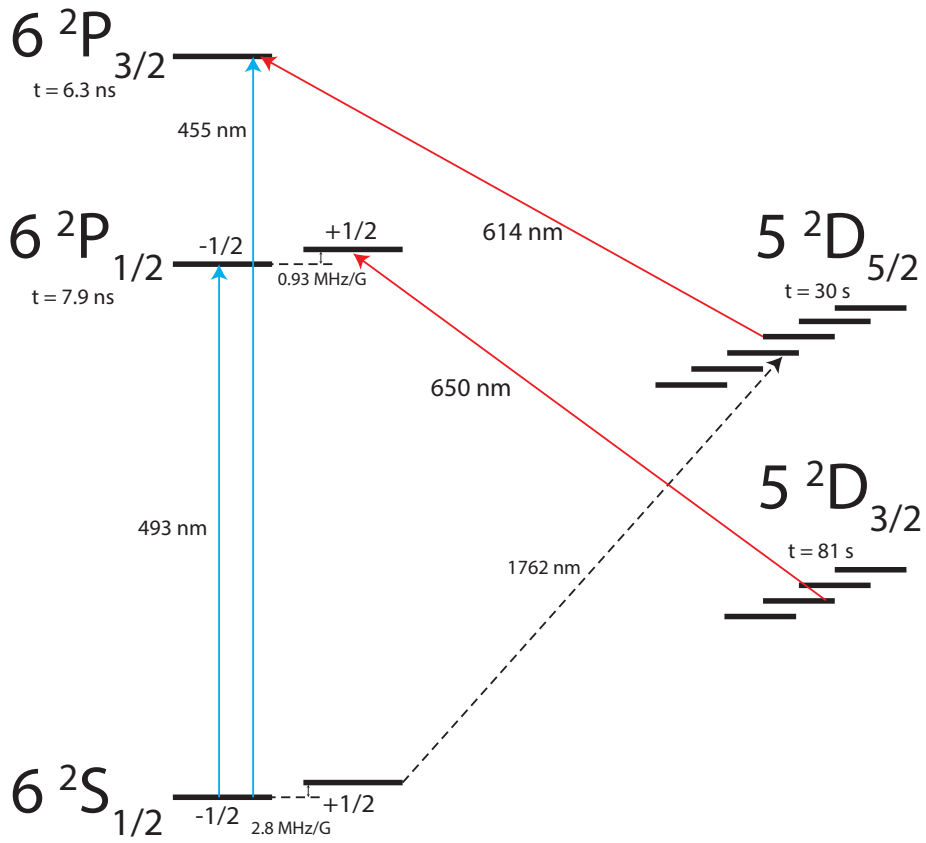

FIGURE 7.1: **Energy levels in $^{138}Ba^{+}$**

in Fig. 7.2. Decay to the $^2D_{3/2}$ state (27% branching ratio) by emission of a 650 nm photon is rejected through spectral filtering as well as chromatic shifts resulting in zero fiber coupling. To measure the state of the atom we perform state-dependent atom fluorescence with a detection time of 1 ms. Histograms of fluorescence counts are shown in Fig. 7.5 for Alice. To differentiate between bright and dark states, we use a threshold of 2.5 counts and 10.5 counts for Alice and Bob, respectively. The different thresholds are due to the fact that the atom state in Bob is detected through the high N.A. side while that for Alice is via the low N.A. side. Employing this method, we achieve a state preparation and measurement (SPAM) fidelity exceeding 99.5% for both Alice and Bob with the residual SPAM error dominated by fluctuations in the 1762 nm operations.

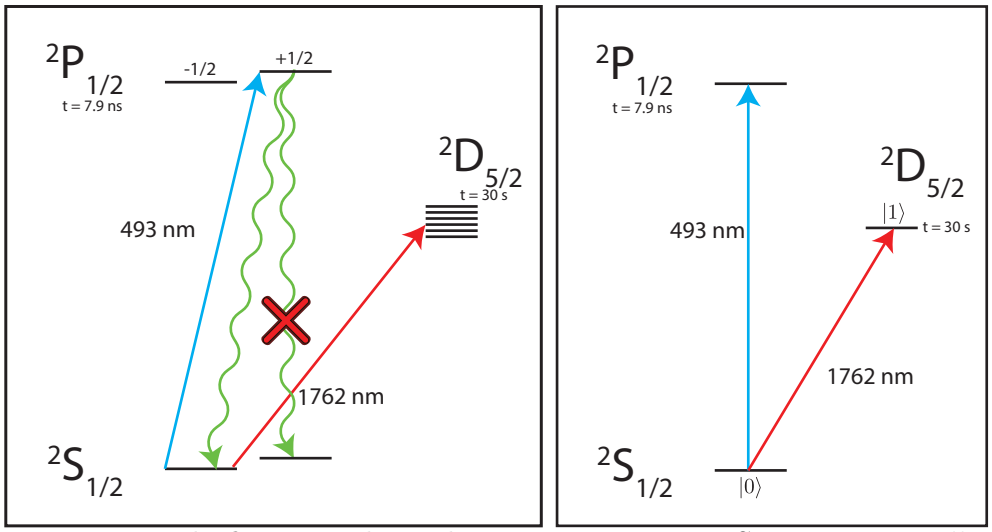

FIGURE 7.2: **Levels for time-bin photon generation:** Since we can collect 493 nm photons, we choose $|0\rangle \equiv |S_{1/2}, m_J = -1/2\rangle$ with 493 decays from $P_{1/2}$. We reject events where the atoms end in $|S_{1/2}, m_J = 1/2\rangle$ by filtering out π photons that get coupled into the fiber. Since $P_{1/2}$ does not decay to $D_{5/2}$ we define $|1\rangle \equiv |D_{5/2}, m_J = -1/2\rangle$. The figure on the right shows that with appropriate definition we can have a level structure as the Barrett-Kok scheme demands.

The experimental setup is completely identical to the previous experiment, since it already had polarization control elements for ion-photon analysis. In this experiment, we couple the same σ and π photons as in the polarization scheme. However, we choose to analyze only the data corresponding to the H photons, while the V photons are completely ignored. This setup is now represented in Fig. 7.3. Similar to before, we collect 493 nm photons emitted from remote trapped atoms into single-mode optical fibers, but now they are entangled in their time of emission.

7.2 Entanglement protocol

We remotely herald entanglement as described below, and shown in Fig. 7.4. First, we use 493 nm and 650 nm laser beams to Doppler-cool each atom. We follow that with state preparation via optical pumping into the $|0\rangle$ state. This is done by turning on the σ^- polarized 493 nm beam together with the 614, 650 nm beams addressing all levels in $D_{3/2}, D_{5/2}$. This incoherent process, prepares a pure

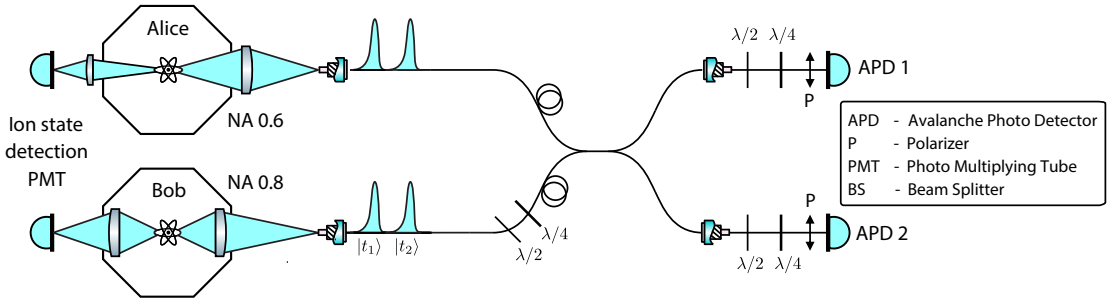

FIGURE 7.3: **Experimental setup:** Our experimental setup is identical to the setup as before, except now we collect photons from two separate chambers: one using 0.8 NA in vacuum aspheres and another using 0.6 NA out of vacuum objectives. Instead of detecting two different polarizations we now detect only horizontal polarizations corresponding to σ^+ decays.

state, by populating only a single level. After this, we apply a $\pi/2$ pulse using 1762 nm light to prepare the coherent superposition state $\frac{1}{\sqrt{2}}(0_q + 1_q)$ [160]. At time t_e, we use a single 493 nm circularly polarized pulse of 3 ps duration to drive $|0\rangle$ to the excited state $|e\rangle$ with a probability $P_{\text{exc}} \sim 0.80$ (excitation probability limited by laser power). Spontaneous emission from $|e\rangle_q$ produces a single 493 nm photon wavepacket that is exponentially distributed over time according to a decay with lifetime of $\tau_R = 7.85$ ns [161]. The ideal unnormalized state of each ion q and its collected photon mode is now

$$\sqrt{1-p_q}\,|0_q 0_e\rangle_q + \sqrt{p_q} e^{i(\phi_{qe}+\phi_{opt})}\,|0_q 1_e\rangle_q + |1_q 0_e\rangle_q \tag{7.1}$$

where $|1_e\rangle$ ($|0_e\rangle$) denotes the presence (absence) of a photon in the first (early) time-bin and p_q is the probability a single photon has been collected. The phase $\phi_{qe} = \mathbf{\Delta k} \cdot \mathbf{r}_q(t_e) + \phi^*_{qe}$ includes the position $\mathbf{r}_q(t_e)$ of ion q. This position is measured in the trap frame, with the origin of the coordinate system set at the trap center, at time t_e of the early time-bin. The phase also includes the wavevector difference $\mathbf{\Delta k} = \mathbf{k}' - \mathbf{k}$, which is the difference between the excitation pulse wavevector $\mathbf{k}'$ and that of the emitted photon $\mathbf{k}$ (both of magnitude k). The small random phase ϕ^*_{qe}

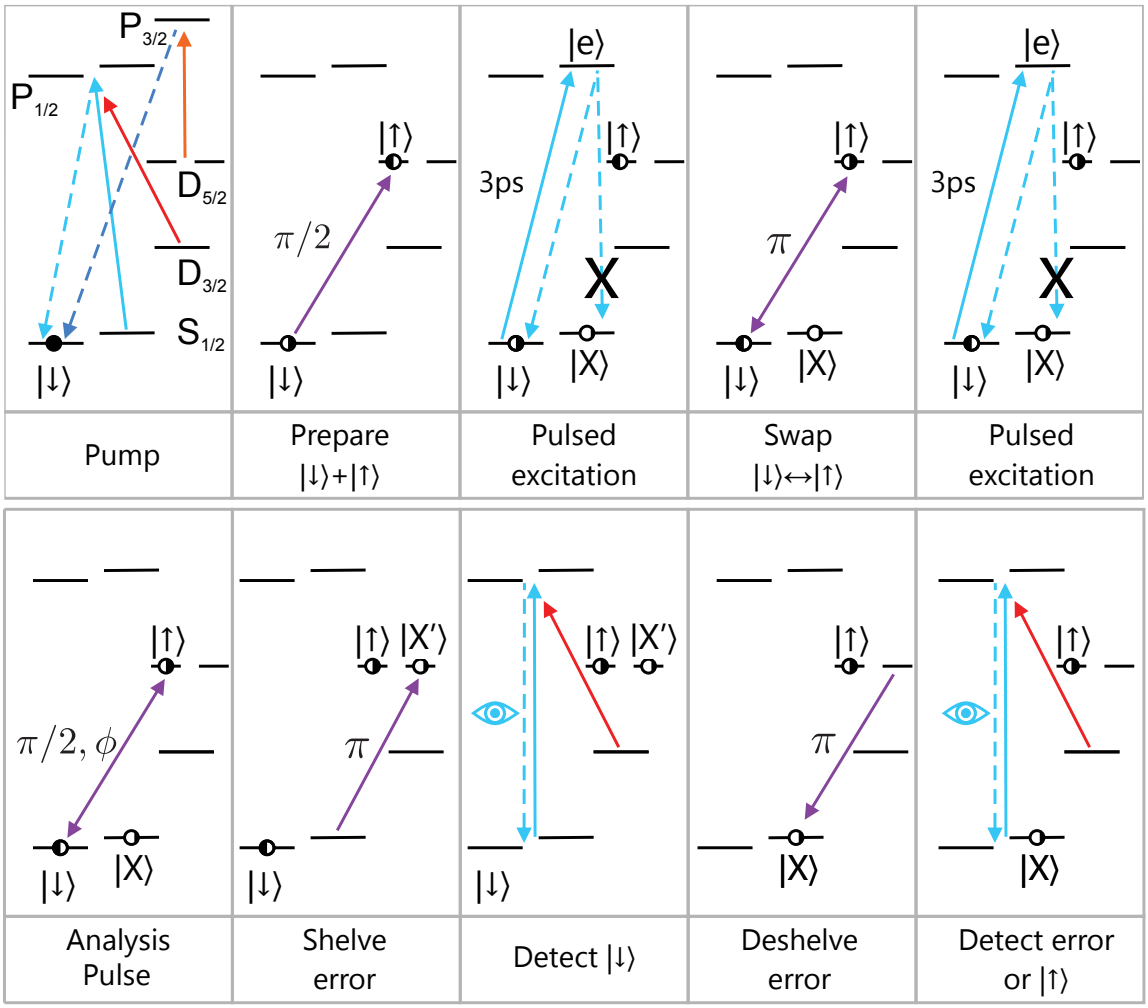

FIGURE 7.4: **Experimental protocol:** We follow the steps in each of the boxes shown above. (1) We start by pumping with 493 nm, 650 nm and 614 nm light. (2) A coherent equal superposition is created with 1762 nm light. (3) The ground state is excited with a 3 ps 493 nm pulse of light and any emission is collected. (4) The qubit levels are swapped. (5) The ground state is excite again and any emission is collected. (6) A $\pi/2$ analysis pulse with a variable phase ϕ is applied. (7) The error state is shelved to $|D_{5/2,m_J} = 1/2\rangle$. (8) First the qubit $|0\rangle$ state is detected by shining 493 nm, 650 nm light. (9) Then the error state is deshelved. (10) The error state is detected and the trial event is discarded if an error hit is found.

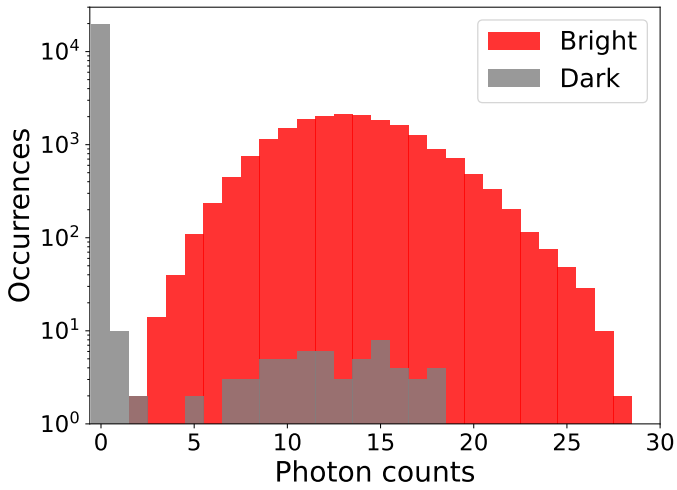

FIGURE 7.5: **State detection histogram:** Here we plot the histogram of single photons detected during a detection time of 1 ms in Alice. State discrimination threshold based on average photon counts obtained in this detection time is set to 2.5.

accounts for the narrow distribution of emission times and is discussed later, while ϕ_{opt} is an optical phase that gets picked up from the excitation and collection path. To generate the second (late) time-bin photon, the populations in $|0\rangle_q$ and $|1\rangle_q$ are swapped with a 1762 nm π-pulse, then at time t_l the $|0\rangle_q$ state is again excited to the $|e\rangle_q$ state. With probability p_q, there is now a single-photon time-bin qubit entangled with its parent atom qubit, ideally in the state

$$e^{i\phi_{opt}}(e^{i\phi_{qe}}\,|1_q\rangle\,|1_e0_l\rangle_q + e^{i\phi_{ql}}\,|0_q\rangle\,|0_e1_l\rangle_q) \tag{7.2}$$

where $|n_e n_l\rangle_q$ denotes a state of n_e (n_l) photons in the early (late) time-bin from atom q. Here we pull out the global phase ϕ_{opt} and ignore it from the rest of the calculations by assuming that the excitation and collection optical path lengths are stable between the early and late excitations. The time-bin photons from Alice and Bob, as seen in Figure 7.6, are then directed to a non-polarizing 50:50 fiber beamsplitter (BS), which erases their "which-path" information through Hong-Ou-Mandel interference [145]. Subsequent detection of early and late photons ideally

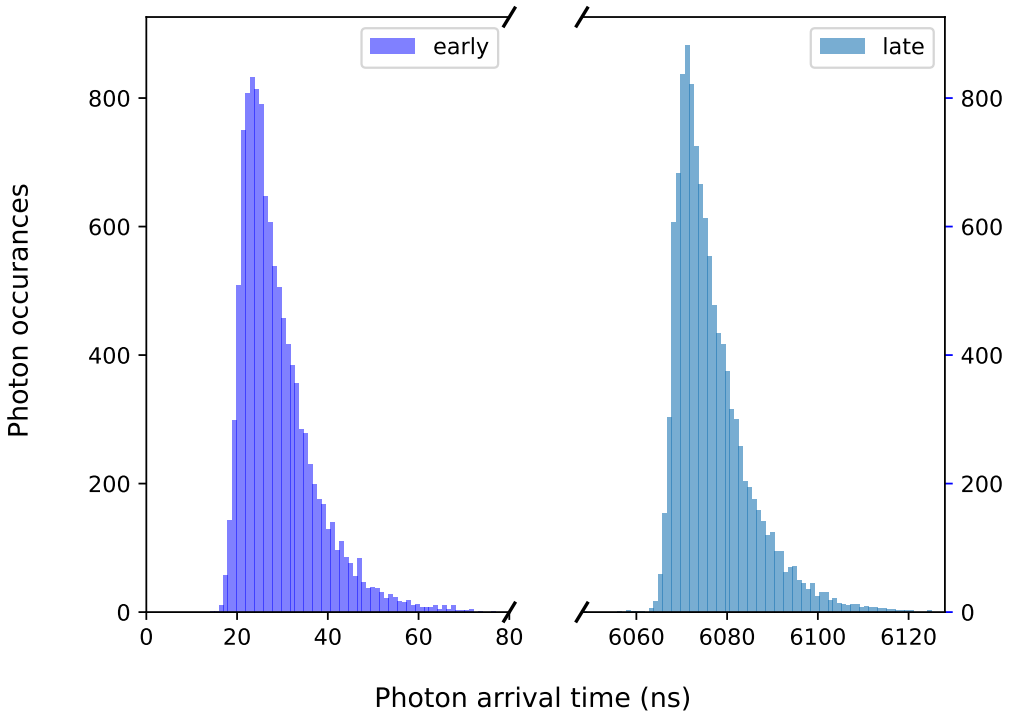

FIGURE 7.6: **Histogram of arrival times** of the late and early photons totaling 11435 events. Early and late time bins are separated by 6048 ns.

projects the ions into a Bell state [51, 155]

$$\Psi^{\pm} = |0_A 1_B\rangle \pm e^{i\phi} |1_A 0_B\rangle \tag{7.3}$$

where the phase is $\phi = (\phi_{Ae} - \phi_{Be}) - (\phi_{Al} - \phi_{Bl})$. The Ψ^+ (Ψ^-) state is heralded by early and late detections on the same (opposite) BS output channels.

The stability of this phase factor is of paramount importance. If this phase starts to vary, we will get Bell states with arbitrary relative phases. When averaged over such states, we will get completely mixed states.

7.3 Entangled phase state stability

Multiple excitation times in the time-bin protocol or even the distribution of emission times within a single time-bin can lead to entanglement between the photon qubit and motion of the each atom from atomic recoil. We use a slightly different

notation than the one on the paper, for the sake of clarity for the reader. We work in the density matrix formalism for calculating the effects of recoil. The initial state of atom $q \in (A, B)$, including its time-bin photon emission modes and motion is

$$\rho_q = \frac{(|1\rangle + |0\rangle)_q(\langle 1| + \langle 0|)_q}{2} \otimes |0_e 0_l\rangle_q \langle 0_e 0_l|_q \otimes M_q \tag{7.4}$$

where $|N_e N_l\rangle_q$ denotes N_e (N_l) photons emitted in the early (late) time bin. The initial motional density matrix M_q is expressed as a thermal state in the basis of coherent states [162]:

$$M_q = \prod_i \frac{1}{\pi \bar{n}_{qi}} \int \mathrm{d}^2\alpha_i |\alpha_i\rangle\langle\alpha_i| e^{-|\alpha_i|^2/\bar{n}_{qi}} \tag{7.5}$$

where $\bar{n}_i$ is the average thermal motional quantum number in direction i.

For now, we drop the index q and also do not worry about the photonic occupation numbers. This is because we are now interested in looking at the effect of recoil on the phase of the atom. Then we can rewrite the state of the atom as

$$\rho = \frac{(|1\rangle + |0\rangle)(\langle 1| + \langle 0|)}{2} \otimes M \tag{7.6}$$

We define the projectors into $|0\rangle$ and $|1\rangle$ as:

$$P_0 = |0\rangle\langle 0|\,; \qquad P_1 = |1\rangle\langle 1| \tag{7.7}$$

These operators are introduced, since after emission and detection of the photon, the atoms will be projected into a specific state. We also notice that the phase we were trying to keep track of earlier as $e^{i\mathbf{\Delta k}\cdot\mathbf{r}(t)}$ is actually the phase change due to a recoil of the atom during a photon absorption/emission event. This amounts to a displacement of the initial phase space distribution of the atom [163]. Note that, as we had defined earlier, $\mathbf{r}(t)$ is the position of the ion measured in the trap frame

with the coordinate origin set at the trap center. We are able to use this inertial frame by assuming that the trap is stable relative to the 493-nm laser light between the early and the late excitations. Therefore we can also rewrite this phase in terms of the coherent displacement operator $\mathcal{D}$ in phase space [162]

$$e^{i\mathbf{\Delta k}\cdot\mathbf{r}(t)} = \mathcal{D}(i\eta) \tag{7.8}$$

Here, η is the Lamb-Dicke parameter given as $\eta = \Delta\mathbf{k} \cdot \mathbf{r}_0$, where $\mathbf{r}_0$ is the spread of the atomic wavefunction in its ground state. η is a measure of how well localized the atom is compared to the wavelength of light interacting with it. After the first excitation and emission, assuming that the photon deterministically interacts with the atom, we can write the operator that acts on the initial density matrix as

$$U_1 = P_0\mathcal{D}(i\eta) + P_1 \tag{7.9}$$

Clearly, this shows that the atom gets a kick when it is in the state $|0\rangle$. This is followed by free evolution for a time τ during which we also swap the two qubit states. This would be then represented by the unitary

$$U_2 = e^{-iH\tau}X \tag{7.10}$$

Here, the Hamiltonian $H = \sum_i \omega_i(n_+\frac{1}{2})$ describes the free evolution of the atomic motion in the trap with harmonic frequencies ω_i and phonon occupation numbers n_i in all three dimensions. The Pauli spin-flip operator $X = |0\rangle\langle 1| + |1\rangle\langle 0|$ describes the qubit swap between emission attempts. Following this we have the late excitation, which is again the same as U_1

$$U_3 = U_1 = P_0\mathcal{D}(i\eta) + P_1 \tag{7.11}$$

Hence the final state, after all of these steps is

$$\rho_f = U_3U_2U_1\rho(U_3U_2U_1)^\dagger \tag{7.12}$$

We can compute the product of the operators to get

$$U_3U_2U_1 = (P_0\mathcal{D}(i\eta) + P_1)\ \ e^{-iH\tau}X\ \ (P_0\mathcal{D}(i\eta) + P_1) \tag{7.13}$$

$$= (P_0\mathcal{D}(i\eta) + P_1)\ \ e^{-iH\tau}(|0\rangle\langle 1| + |1\rangle\langle 0|)\ \ (P_0\mathcal{D}(i\eta) + P_1) \tag{7.14}$$

$$= (P_0\mathcal{D}(i\eta) + P_1)\ \ e^{-iH\tau}\ \ (|1\rangle\langle 0|\,\mathcal{D}(i\eta) + |0\rangle\langle 1|) \tag{7.15}$$

$$= (|0\rangle\langle 1|\,\mathcal{D}(i\eta)e^{-iH\tau} + |1\rangle\langle 0|\,e^{-iH\tau}\mathcal{D}(i\eta)) \tag{7.16}$$

Here we have used the fact that motional and spin part of the Hilbert space commute with each other. Now we can apply this to the initial density matrix to get

$$U_3U_2U_1\rho = (|0\rangle\langle 1|\,\mathcal{D}(i\eta)e^{-iH\tau} + |1\rangle\langle 0|\,e^{-iH\tau}\mathcal{D}(i\eta))\frac{(|1\rangle + |0\rangle)(\langle 1| + \langle 0|)}{2} \otimes M \tag{7.17}$$

$$= (|0\rangle\langle 1| + |0\rangle\langle 0|)\mathcal{D}(i\eta)e^{-iH\tau} + (|1\rangle\langle 0| + |1\rangle\langle 1|)e^{-iH\tau}\mathcal{D}(i\eta) \otimes M/2 \tag{7.18}$$

Also on the other side, we have the adjoint of this operator

$$(U_3U_2U_1)^\dagger = (e^{iH\tau}\mathcal{D}(-i\eta)\,|1\rangle\langle 0| + \mathcal{D}(-i\eta)e^{iH\tau}\,|0\rangle\langle 1|) \tag{7.19}$$

Finally, then we can multiply all terms together to get

$$\rho_f = U_3U_2U_1\rho(U_3U_2U_1)^\dagger \tag{7.20}$$

$$= [(|0\rangle\langle 1| + |0\rangle\langle 0|)\mathcal{D}(i\eta)e^{-iH\tau} + (|1\rangle\langle 0| + |1\rangle\langle 1|)e^{-iH\tau}\mathcal{D}(i\eta)] \otimes M/2 \tag{7.21}$$

$$\otimes\,[e^{iH\tau}\mathcal{D}(-i\eta)\,|1\rangle\langle 0| + \mathcal{D}(-i\eta)e^{iH\tau}\,|0\rangle\langle 1|] \tag{7.22}$$

$$= \int d^2\alpha \frac{e^{-|\alpha|^2}}{2\pi\bar{n}}[(|0\rangle\langle 1| + |0\rangle\langle 0|)\mathcal{D}(i\eta)e^{-iH\tau}\,|\alpha\rangle + (|1\rangle\langle 0| + |1\rangle\langle 1|)e^{-iH\tau}\mathcal{D}(i\eta)\,|\alpha\rangle] \tag{7.23}$$

$$\otimes\,[\langle\alpha|\,e^{iH\tau}\mathcal{D}(-i\eta)\,|1\rangle\langle 0| + \langle\alpha|\,\mathcal{D}(-i\eta)e^{iH\tau}\,|0\rangle\langle 1|] \tag{7.24}$$

Now we are can finally trace over the motional part, by looking at the diagonal

components of the motional subspace:

$$\rho_f = \int d^2\alpha \frac{e^{-|\alpha|^2}}{2\pi\bar{n}} [\, |0\rangle\langle 0| \langle\alpha|\, e^{iH\tau}\mathcal{D}(-\rangle\eta)\mathcal{D}(\rangle\eta)e^{-iH\tau}\, |\alpha\rangle + \tag{7.25}$$

$$|1\rangle\langle 1| \langle\alpha|\, \mathcal{D}(-\rangle\eta)e^{iH\tau}e^{-iH\tau}\mathcal{D}(\rangle\eta)\, |\alpha\rangle + \tag{7.26}$$

$$|1\rangle\langle 0| \langle\alpha|\, e^{iH\tau}\mathcal{D}(-i\eta)e^{-iH\tau}\mathcal{D}(i\eta)\, |\alpha\rangle + \tag{7.27}$$

$$|0\rangle\langle 1| \langle\alpha|\, \mathcal{D}(-i\eta)e^{iH\tau}\mathcal{D}(i\eta)e^{-iH\tau}\, |\alpha\rangle] \tag{7.28}$$

The diagonal terms simplify to unity, however the off diagonal terms need to be calculated. To compute these matrix elements we first state some properties of coherent states. Notice that,

$$e^{-iH\tau}\, |\alpha\rangle = |\alpha e^{-i\omega\tau}\rangle, \quad \langle\alpha|\, e^{iH\tau} = \langle\alpha e^{i\omega\tau}|\,.$$

and,

$$\langle\alpha|\, e^{\frac{i}{\hbar}H\tau}\, D(-i\eta)\, e^{-\frac{i}{\hbar}H\tau} = \langle\alpha e^{i\omega\tau}|\, D\big(-i\eta\, e^{-i\omega\tau}\big).$$

Now consider the term,

$$\rho_f^{10} = \int \frac{d^2\alpha}{2\pi\bar{n}}\, e^{-\frac{|\alpha|^2}{\bar{n}}}\, \langle\alpha|\, e^{iH\tau}\, D(-i\eta)\, e^{iH\tau}\, D(i\eta)\, |\alpha\rangle\,. \tag{7.29}$$

Using the displacement-product identity

$$D(\lambda_1)\, D(\lambda_2) = e^{\frac{1}{2}(\lambda_1\lambda_2^* - \lambda_1^*\lambda_2)}\, D(\lambda_1 + \lambda_2),$$

we set $\lambda_1 = -i\eta\, e^{-i\omega\tau}$, $\lambda_2 = i\eta$ to get

$$D(-i\eta\, e^{-i\omega\tau})\, D(i\eta) = e^{-\,i\eta^2 \sin(\omega\tau)}\, D\big(i\eta(1 - e^{-i\omega\tau})\big).$$

We also look at this result for writing the displacement operator in a coherent state basis

$$\langle\beta|\, D(\lambda)\, |\alpha\rangle = \exp\Big[-\tfrac{1}{2}|\lambda|^2 + \lambda\,\alpha^* - \lambda^*\,\beta + \beta^*\,\alpha\Big].$$

Finally, we can compute the cross terms of the final density matrix

$$\rho_f^{10} = = e^{-\,i\eta^2\sin(\omega\tau)} \int \frac{d^2\alpha}{2\pi\bar{n}}\ \exp\Big[-\tfrac{|\alpha|^2}{\bar{n}} - \tfrac{1}{2}\big|i\eta(1-e^{-i\omega\tau})\big|^2\ +\ i\eta(1-e^{-i\omega\tau})\,\alpha^* \\ -\ (-i\eta(1-e^{i\omega\tau}))\,(\alpha e^{i\omega\tau}) + \alpha^* e^{-i\omega\tau}\,\alpha\Big] \tag{7.30}$$

We switch to $\alpha = x + iy$, complete the square in x, y, and use the Gaussian integral result$\int e^{-a(x-b)^2}dx = \sqrt{\pi/a}$ to find that

$$\rho_f^{10} = \tfrac{1}{2}\ \exp\Big[-(2\bar{n}+1)\,\eta^2\,(1-\cos\omega\tau)\Big]\ \exp\Big[i\,\eta^2\sin(\omega\tau)\Big]. \tag{7.31}$$

Hence, we can write the full density matrix as

$$\rho_f = \frac{1}{2}\begin{pmatrix} 1 & e^{-\Gamma(\tau)}\,e^{i\phi(\tau)} \\ e^{-\Gamma(\tau)}\,e^{-i\phi(\tau)} & 1 \end{pmatrix},$$

with

$$\Gamma(\tau) = (2\bar{n}+1)\,\eta^2\,[1-\cos(\omega\tau)], \quad \phi(\tau) = \eta^2\sin(\omega\tau).$$

The coherence amplitude, now summing over all dimensions i, can be written as

$$C = \prod_i e^{-\eta_i^2(2\bar{n}_i+1)(1-\cos\omega_i\tau)} \tag{7.32}$$

and its zero-point phase offset is $\phi_i = \eta_i^2\sin\omega_i\tau$, which is very small for $\eta_i \ll 1$. Here τ is the time separation between the two emissions from the atom. To maximize the coherence amplitude, which will directly impact the fidelity, we can try making the exponent of the exponential close to zero by cooling the atom well to reduce $\bar{n}$, reducing η by confining the atom strongly or have $\omega_i\tau = 0$ or $n\pi$.

One can try to implement the last condition, by fixing the time between the excitations to be commensurate with the secular frequencies. However, there will always be an intrinsic randomness because the emission is spontaneous due to the finite lifetime τ_R of each atomic emitter resulting in the random phase ϕ_e^* that appeared earlier. If we carry out the same treatment as above for the case of time

variations due to spontaneous emissions, we find that the coherence amplitude is reduced further by the factor

$$C' = \prod_i e^{-\zeta_i^2(2\bar{n}_i+1)[1-\cos\omega_i(\tau^*-\tau)]} \tag{7.33}$$

with an additional negligible phase offset [155]. Here, τ^* is the measured difference in detection time of the two photons in the early and late time bins for each event. This is similar to the form of Eq. 7.32, except the relevant Lamb-Dicke parameter $\zeta_{qi} = k_i\sqrt{\hbar/2m\omega_{qi}}$ is associated with only the recoil from emission. The random variable τ^* follows a double-sided exponential (Laplace) distribution with mean 0 and variance $2\tau_R^2$. We can reduce the impact of this variance by symmetrically truncating this distribution by post-selecting events with photon detection times within $\pm\delta t$ of the nominal value, or $|\tau^* - \tau| < \delta t$. This results in $\tau^* - \tau$ following a truncated Laplace distribution with mean 0 and variance $2\tau_R^2 W$, where the variance parameter

$$W = \frac{1-(1+w+w^2/2)e^{-w}}{1-e^{-w}} \tag{7.34}$$

smoothly increases from 0 to 1 as the relative window size $w \equiv \delta t/\tau_R$ increases from 0 to ∞. The yield of accepted events is $Y = 1 - e^{-w}$. For $\omega_{qi}\tau_R \ll 1$, the above average results in

$$C' \approx \prod_{qi} e^{-\zeta_{qi}^2(2\bar{n}_{qi}+1)W\omega_{qi}^2\tau_R^2}. \tag{7.35}$$

Furthermore, if also $\zeta_{qi}^2(2\bar{n}_{qi}+1)\omega_{qi}\tau_R \ll 1$, then

$$C' \approx 1 - \sum_{qi} \zeta_{qi}^2(2\bar{n}_{qi}+1)W\omega_{qi}^2\tau_R^2. \tag{7.36}$$

The net entanglement contrast is $C = CC'$, comes out as:

$$C = \prod_{qi} \exp\left\{-(2\bar{n}_{qi}+1)\left[\eta_{qi}^2(1-\cos\omega_{qi}\tau) + \zeta_{qi}^2 W\omega_{qi}^2\tau_R^2\right]\right\} \tag{7.37}$$

The first decoherence term in Eq. 7.37 is due to residual entanglement between the spin of the atom and it's motion from the separated time of excitation $\tau = t_l - t_e$ and is specific to time-bin encoding schemes. Here, the Lamb-Dicke recoil parameter is given by $\eta_{qi} = \Delta k_i \sqrt{\hbar/2m\omega_{qi}}$ for ion q with mass m with respect to the wavevector difference between excitation and emission along i. Only when $\omega_{qi}\tau$ is an integer multiple of 2π for all modes, each ion is excited from the same position in each time bin, thereby erasing any residual spin-motion entanglement. We implement this in our experiment by tuning the mode frequencies to be commensurate and setting the excitation rate $1/\tau$ to be their greatest common divisor ($\tau = 6048$ ns), as summarized in Table 7.1. We also observe this effect by scanning the difference in

Table 7.1: Measured harmonic motional frequencies ω_{qi} for the two atomic ions $q = A, B$ along direction i and their commensurability with the photonic excitation rate $\tau^{-1} = 165.35$ kHz ($\tau = 6048$ ns). The six mode frequencies are set to be nearly integer multiples of the excitation rate, suppressing errors from residual entanglement with motion. Also shown are the Lamb-Dicke parameters η_{qi} and ζ_{qi} with respect to the excitation/emission wavevector difference and the wavevector of emission, respectively.

q (ion)	i (mode)	$\frac{\omega_{qi}}{2\pi}$ (kHz)	$\frac{\omega_{qi}\tau}{2\pi}$	η_{qi}	ζ_{qi}
A	Axial	991.5	5.996	0.055	0
A	Radial 1	1157.5	7.000	0.086	0.051
A	Radial 2	1488.0	8.999	0.013	0.045
B	Axial	330.3	1.997	0.095	0
B	Radial 1	826.7	4.999	0.066	0.0067
B	Radial 2	992.0	5.999	0.073	0.077

excitation times τ about the nominal value, as shown in Fig. 7.8. We estimate that the residual fidelity error from the drift in mode frequencies is less than 0.1%.

The second decoherence term in the exponent of Eq. 7.37 is a fundamental error which has not been studied or observed before. It arises from the random detection times of the photons in each time bin through the random phase ϕ^*_{qe} given by the finite lifetime of the emitting atoms, creating residual entanglement between the

qubits and their motion as above. Note that, in this case, the Lamb-Dicke recoil parameter $\zeta_{qi} = k_i\sqrt{\hbar/2m\omega_{qi}}$ is with respect to the emission wavevector only. This decoherence effect can be difficult to eliminate. In principle, if one can measure the exact time of emission of the two photons, then appropriate spin-dependent kicks of the right strength can be applied to combat this effect. We controlled this effect simply by narrowing the detection window δt characterized by the scaled variance $0 < W < 1$, at the cost of a degraded yield Y and consequently a reduced rate of entanglement.

Figure 7.9 shows the observed fidelity and yield as we vary δt from 2 ns ($W \approx 0.01$, $Y = 0.22$) to 50 ns ($W \approx 0.95$, $Y = 0.998$). The measurements are consistent with the model of Eq. 7.37, assuming thermal states of motion near the Doppler laser-cooling limit for all modes. We observe a $\sim 1\%$ improvement in the fidelity by decreasing the window from 50 ns to 10 ns ($Y = 0.71$), with a residual fidelity error of $\sim 0.2\%$.

This decoherence from random photon arrival times is universal to all photonic encoding schemes for recoiling emitters but has not been previously observed. For fixed emitters such as color-centers in solid-state hosts [156], the emitter mass becomes so large that $\eta_{qi}, \zeta_{qi} \to 0$ and the above recoil-induced decoherence is negligible. For very weakly-bound emitters such as neutral atoms [164, 165], where $\omega_{qi}\tau, \zeta_{qi} \ll 1$, these effects can be prominent, depending on the level of cooling.

7.4 Experimental parameters

The linear Zeeman splitting between our qubit states is 0.56 MHz/G as seen in Table 3.2. A static magnetic field of approximately 4 G is applied to each ion trap chamber, and the field strength is balanced to better than 1 mG across both traps to align the qubit transition frequencies within 200 Hz.

7.4.1 1762 nm laser system

The 1762 nm light is generated by a Thulium-doped distributed-feedback fiber laser (NKT Photonics), which is amplified to a total output of 450 mW. In both systems, approximately 20 mW of laser power is focused to a 20 μm waist at the ion, allowing us to drive a resonant π-pulse from $|0\rangle = |^2S_{1/2}, m_J = -\frac{1}{2}\rangle$ to $|1\rangle = |^2D_{5/2}, m_J = -\frac{1}{2}\rangle$ in $\tilde{4}.2$ μs, corresponding to a Rabi frequency of approximately 120 kHz.

7.4.2 493 nm pulsed laser system

Single photon generation relies on excitation pulses of duration $t_p \ll \tau_R$, where $\tau_R = 7.855$ ns is the radiative lifetime of the excited $|e\rangle$ state. To generate fast, single pulses at 493 nm, we use a mode-locked Ti:Sapphire laser (Coherent Mira 900P) at 986 nm, producing $t_p \approx 3$ ps pulses at a repetition rate of $f_{\text{rep}} = 76.226$ MHz [1]. The pulses are sent through an electro-optic pulse picker that selectively transmits a single pulse when triggered. These pulses are then frequency-doubled with a MgO-doped, periodically-poled lithium niobate crystal to 493 nm, quadratically increasing the extinction ratio of neighboring pulses to a level below 10^{-4}. After passing through an AOM that further extinguishes subsequent pulses, the single pulse is split in two paths and fiber-coupled into polarization-maintaining optical fibers directed to Alice and Bob.

The probability of two photons being emitted from either atom after a single pulse is estimated to be $P_{\text{exc}}^2\beta^2(t_p/8\tau_R) < 10^{-5}$. Here $P_{\text{exc}} \sim 0.8$ (limited by laser power) is the excitation probability over the duration of the pulse and $\beta = 0.49$ is the successful branching ratio back to the 0 state. The emitted single photons are then collected into a fiber with 0.6 and 0.8 NA objectives. Since these objectives focus 650 nm light at a different spatial point 650 nm photons are filtered out due to heavy mismatch of wave overlap at the single mode fiber face. Band-pass filter with

a bandwidth of 10 nm centered at 488 nm and an OD more than 5 at 650 nm also help in blocking 650 nm photons.

We connect the clock output of the Ti:Sapphire laser to the control system to synchronize the start of the experimental procedure with the laser repetition rate. This synchronization leads to a more precise time-stamp of the arrival photons, removing a potential unsynchronized $1/f_{\text{rep}} \approx 13$ ns timing jitter.

7.5 Experimental results

Entanglement events are heralded by the detection of a single photon within a defined temporal window that includes both the early and late time bins as seen in Fig. 7.6. We measure the quality of entanglement by measuring state fidelity with respect to the Bell state in Eq. 7.3. The fidelity is recorded by experimentally measuring the following terms of the equation, $F = (P_{\text{odd}} + C)/2$. Here P_{odd} is the population of the odd parity states $|0_A 1_B\rangle$ or $|1_A 0_B\rangle$ and C is the contrast of parity oscillations of the two qubit states as the relative phase of analysis $\pi/2$ rotations on each qubit is scanned [166]. In this experiment, since we have atoms trapped in different chambers, we can drive 1762 rotations with different phases. Since we scan the relative phase between the two atoms, both the Bell states undergo sinusoidal parity oscillations with a maximum theoretical amplitude of 1. Fig. 7.7 shows measurements of the fidelity, parity contrast, populations, detection window time and the yield of measurements for both states $\Psi^{\pm}$. Here, we measure yield as the fraction of entanglement events that we keep from the total dataset given that two clicks fall within a certain collection window δt.

As shown in Fig. 7.7, the measured fidelities of the entangled states (uncorrected for SPAM) are $F = 0.968(4)$ for the state Ψ^+ and $F = 0.972(3)$ for the state Ψ^-.

As predicted in Eq. 7.37, we see in Fig. 7.8 that, as the time between excitations become non-commensurate with the motional frequencies, the fidelities drop. The

Bell state	$P_{\uparrow_A\downarrow_B} + P_{\downarrow_A\uparrow_B}$	C	F	δt	Y
Ψ^+	0.990(4)	0.927(6)	0.959(4)	50 ns	0.998
Ψ^-	0.996(3)	0.931(6)	0.963(3)	50 ns	0.998
Ψ^+	0.990(4)	0.948(6)	0.968(4)	10 ns	0.714
Ψ^-	0.996(3)	0.949(6)	0.972(3)	10 ns	0.714

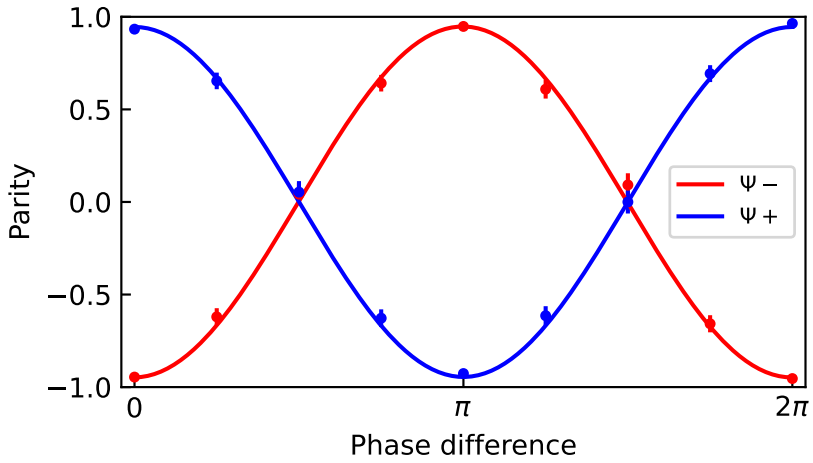

FIGURE 7.7: **Parity scan:** Here we plot the parity of the entangled state, given in Eqn. 6.10 as a function of the phase difference applied to the qubit laser across the two qubits. The entangled states undergo parity oscillations as the phase of the analysis $\pi/2$ pulse is scanned in opposite directions for different atoms. The top table shows the populations of the entangled state as measured in the z basis. Along with the contrast measurements C from the parity fringes, we obtain the fidelity $F = (P + C)/2$. Measurements for two different photon collection window sizes δt are given, showing that closing down the window increases fidelity at the cost of a reduced yield. The yield Y in the table measures the fraction of clicks we keep as we choose clicks in a given window δt. Note that the parity oscillations shown in the figure correspond to a detection window of δt, given in the last two rows of the table.

fidelities are maximized with time between excitations $\tau = 6048$ ns. Note that the experimental data which are plotted as red dots were not optimized to obtain the best fidelity, but to demonstrate the fidelity dependence on motional synchronization and therefore are separate from the main results shown in this chapter. In this figure, the red curve shows the cooling configuration in our experiment, where one of the principal axis of the trap is almost orthogonal to the laser cooling beam leading to

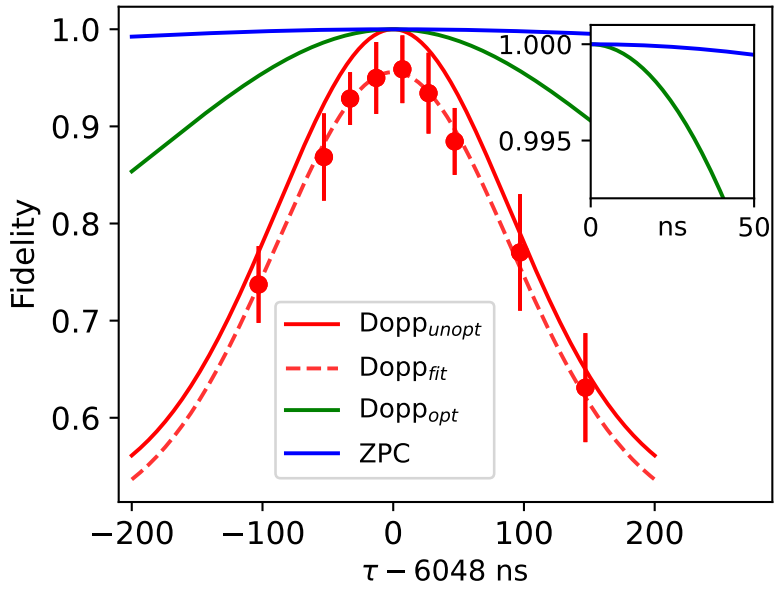

FIGURE 7.8: Here we plot the measured fidelities of the entangled state of two ions as we vary the time between two excitations in our time-bin scheme. The red dashed curve represents a rescaled version of Eq. 7.37. The red solid curve shows the theoretical curve given our current sub-optimal Doppler cooling beam geometry, with $\bar{n}$ values along the three axis given by (13, 12, 15) for Alice and (38, 15, 826) for Bob. This sub-optimal geometry is due to the fact that one of the principal axis in the radial plane is almost orthogonal to the Doppler cooling beam resulting in inefficient cooling along that direction. The green curve is assuming a beam geometry that forms a 45° angle between the Doppler cooling beam and any principal trap axis. Finally the blue curve show zero-point cooling (ZPC, $\bar{n} \sim 0$). The inset shows that with a reasonable window size and optimal Doppler cooling, it is possible to obtain fidelities exceeding 99.5%.

high temperatures along that direction. By applying appropriate quadrupole DC voltages, it is possible to rotate the principal axis such that the cooling beam is at equal angles to all the principal axes resulting in cooling along all directions. This is depicted by the green curve, in the same figure.

The coherence of the entangled state of Eq. 7.3 is insensitive to common-mode qubit decoherence. In order to determine the effect of differential qubit decoherence on the observed state fidelity (presumably from differential magnetic field noise), we perform a Ramsey experiment on qubit A as observed from the frame of qubit

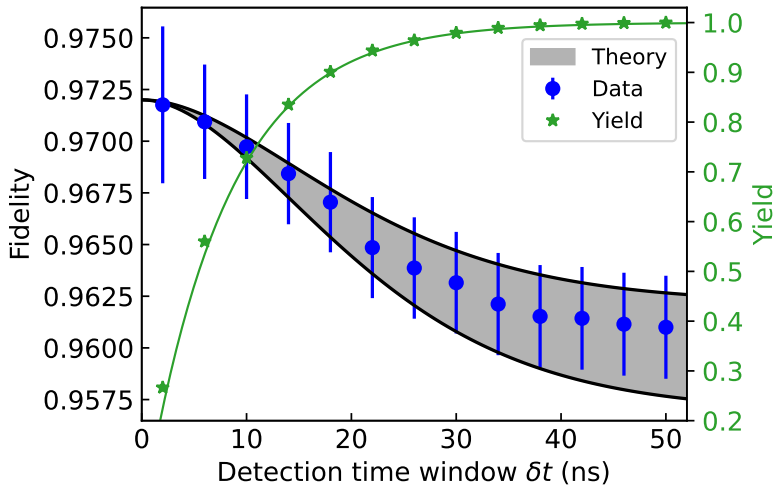

FIGURE 7.9: In this figure we plot the fidelity of the entangled state, as we close down the detection window in the early and late time bins. The data points are drawn from a single experimental run, and, heralded states within a certain detection window are analyzed for their fidelity, with statistical error bars shown. For a given detection time window δt we include all the data points detected in that time window difference. The green curve shows the fraction of data from the dataset, that we keep based on δt. The shaded region indicates the expected fidelity, including motional recoil from Eq. 7.37, assuming Doppler cooling for all modes given the beam geometry. This band was normalized to match the experimental value for $\delta t = 0$ with a width reflecting the uncertainty in the angles of the ion trap principal axes. The green line (right axis) shows the measured (points) and theoretical (line) yield for each value of, with no free fit parameters.

B [93, 167]. After preparing both ions in the $|0\rangle$ state, we use the 1762 nm laser to apply a $\pi/2$ pulse to both qubits, wait for some delay time Δt, and then apply another $\pi/2$ pulse with a scrambled phase. By varying the relative phase difference of the second pulse between the two ions, we measure and fit the parity of the two qubit states to extract the contrast as shown in Fig. 7.10. Since the two qubits are not initially entangled, the maximum parity expected without decoherence is 0.5. After repeating the measurement for different Δt, we fit the parity amplitudes to measure the differential decoherence time T_2^*. From the data shown in Fig. 7.10 we fit to $\exp[-(t/T_2^*)^2]$ and obtain $T_2^* = 2.10(4)$ ms. This is consistent with an rms differential magnetic field noise of ~ 1 mG over the measurement bandwidth.

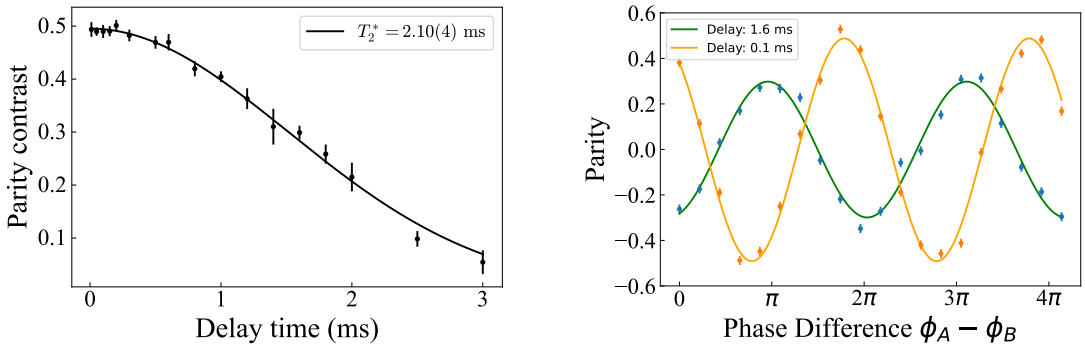

FIGURE 7.10: **Differential qubit coherence:** In the left figure, we perform a Ramsey time experiment, where after waiting a delay time, we measure the two atom parity. In the left figure we plot the contrast of parity oscillations of two, ideally uncorrelated ions as a function of the delay time in a Ramsey-type experiment. In the right figure we plot the joint parity of the qubits as we scan the phase difference between the analysis pulses of the qubit lasers. For such a completely uncorrelated qubit this number should be one half. However due to differential noise, we see a decay in the parity contrast with a decay time of 2.1 ms.

7.5.1 Correction of Erasure Errors

During the photon emission process, there is a $\sim$ 24% probability that each ion decays to the wrong ground state $|X\rangle = |^2S_{1/2}, m_J = +1/2\rangle$. Although the corresponding π-polarized photons are blocked by a polarizer with $>$ 98% efficiency, polarization mixing from imperfect alignment [168], drifts of the fiber birefringence or possibly window birefringence make it difficult to passively eliminate these false positives. However, we can flag this qubit erasure error by shelving the state $|X\rangle$ to $|X'\rangle = |^2D_{5/2}, m_J = +1/2\rangle$ before state detection. After state detection, we de-shelve $|X'\rangle$ back to $|X\rangle$ and perform another round of state detection to check for the error as denoted in Fig. 7.11. This allows for the suppression of erasure errors to below 0.1% [169] with very little loss in success rate. Using this technique, we observed a fidelity improvement of at least 1%, with gains exceeding 10% in unoptimized experimental runs characterized by a higher polarization error. This erasure-veto technique will play an increasingly important role in suppressing errors when single

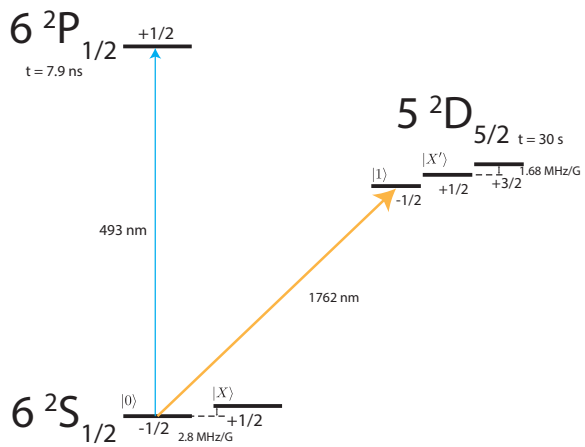

FIGURE 7.11: **Erasure levels:** When the atom falls into the wrong state, we can shelve it to a different state, and check it later to see if we had an error. This is known as an erasure error.

mode fibers susceptible to polarization drifts are used for long-distance quantum communication [170].

7.5.2 Entanglement rate calculation

The maximum success probability of ion-ion entanglement is $P_E = \frac{1}{2} p_A p_B$ which is measured to be 2.3×10^{-5}. The factor of 1/2 accounts for the rejection of events where both photons are collected in the same time-bin (and on the same detector). The individual collection and detection probabilities of each node are $p_q = p_{\text{exc}} \beta \epsilon_F T \epsilon_D (d\Omega_q / 4\pi)$. Here $p_{exc} = 0.8$ is the probability of excitation (limited by laser power), $\beta = 0.49$ is the effective branching ratio into the correct subspace, $\epsilon_F \approx 19\%$ is the fiber coupling efficiency (including polarization rejection by the fiber [168]), $T \approx 90\%$ is the transmission through optical elements, $\epsilon_D = 0.71$ is the detector efficiency of the avalanche photodiodes (APD), and $d\Omega_q$ is the solid angle of light collection from chamber q. The objective lenses have numerical apertures (NA) of 0.6 in Alice and 0.8 in Bob [148]), so $d\Omega_A/4\pi = 10\%$ and $d\Omega_B/4\pi = 20\%$.

We select coincident events occurring within a detection time window $\pm\delta t$ of the mean photon arrival time of each time-bin, resulting in a small reduction in P_E by the

yield factor $Y = 1 - e^{-\delta t/\tau_R}$, given the atomic lifetime τ_R. For a detection time window of $\delta t = 10$ ns (yield $Y = 0.71$), the mean entanglement rate is $P_E Y R f = 0.35\, s^{-1}$ at a repetition rate of $R = 70$ kHz and a duty cycle of $f = 30\%$ due to laser-cooling interruptions.

7.5.3 Error budget

The largest source of error in the entangled state fidelity is intensity fluctuations in the 1762 nm laser that drives coherent qubit rotations, contributing to SPAM and the swap of qubit states in the protocol. We observe $\sim 0.5\%$ fluctuations of the 1762 π time over a few-hour time period. Slow drifts longer than several hours are eliminated between runs through periodic calibration. These fluctuations degrade SPAM and are expected to contribute to a fidelity error of 1.9%. We have not used compound pulses such as BB1 or SK1, which can reduce 1762 pulse errors at the cost of an extended duty cycle of the experiment.

The temporal wavefunctions of the photons are matched to within 30 ps at the BS by equalising the path length between the excitation laser and the BS, leading to a small error of 0.2%. We expect a fidelity error of 0.2% from residual entanglement with ion motion due to the recoil from the spread of photon detection times within each time-bin, at a detection window of $\delta t = 10$ ns. Dark counts on the photon detectors and background scattered light from the excitation pulse are expected to contribute <0.2%. Imbalance in the fiber BS (measured to be less than 2% from the nominal 50:50) and imperfect BS mode matching are expected to limit fidelity errors to below 0.1%. We observe a differential qubit coherence time of 2.1 ms, likely due to differential magnetic field noise between the two qubits. This is expected to reduce the fidelity by $< 10^{-4}$ during the ~ 8 μs dwell time between the early photon detection and the analysis $\pi/2$-pulse. Residual rf micromotion of trapped ions [125] can result in a fluctuating frequency of the emitted photons,

causing a phase error in the final entangled state and a reduction in the fidelity. We measure a micromotion-induced Doppler shift of under 200 kHz through a photon autocorrelation procedure [125], and expect this to contribute to a fidelity error of less than 10^{-4}.

All these error sources are summarized in Table 7.2.

Table 7.2: Sources of error affecting fidelity and their magnitudes.

Source of error	**Fidelity Error**
SPAM / 1762 intensity fluctuations	0.019
Photon wavepacket overlap	0.002
Atom recoil, $\delta t = 10$ ns	0.002
Background counts	< 0.002
Atom recoil, ω_{qi} fluctuation	< 0.001
Beamsplitter imperfection	< 0.001
Residual erasure errors	< 0.001
Micromotion	< 0.0001
Coherence time	< 0.0001
TOTAL	**<0.029**

7.6 Discussion

Time-bin encoded photons offer a reliable and arguably simple way to entangle trapped ions over long distances with very high fidelity. We find that most of our entanglement errors come from technical limitations. By stabilizing the 1762 nm laser power, using hyperfine clock qubits with essentially unlimited coherence, locking trap frequencies in the MHz range, cooling ions to below one motional quantum, and improving state preparation and measurement, we expect to push remote entanglement fidelities beyond 99.9%.

Increasing the 1762 nm laser intensity and stability to reach Rabi frequencies above 1 MHz could raise entanglement rates to around 10^3 events per second. Achiev-

ing both high fidelity and high speed is crucial for scaling up photonically connected quantum computers, building efficient quantum repeaters, and enabling long-distance quantum communication protocols [171].

7.6.1 Optimizing Rate and Fidelity

Our error budget (Table 7.2) shows that drift in the Rabi frequency of our 1762 nm laser is the largest error source. Adding a noise eater or active feedback to stabilize laser power below 0.1%, using low-intensity Doppler cooling on all axes, setting a short photon detection window (<10 ns), and running at high trap frequencies will bring us to the Doppler cooling limit. At that point, recoil-limited fidelity naturally exceeds 99.9% (see Fig. 7.8).

The difference in rates between the time-bin schemes and the polarization scheme are primarily due to a reduced attempt rate from the long 1762 pulses and an effective lower single photon collection due to working with a single polarization. To boost our current sub-Hz entanglement rates into the kHz regime, we need shorter 1762 nm pulses. By focusing the laser more tightly, we can cut π-pulse times to a few hundred nanoseconds. Higher trap frequencies (several MHz) let us synchronize with ion motion without slowing down the fast loop. This along with a faster EOM based pumping scheme to bypass the latency due to AOMs may allow us to increase our attempt rate to more than 1.0 MHz from the current 70 kHz. We can construct a second Cleo to get twice the light collection for the second chamber, increase the fiber coupling to 45% from the current 19% using corrective lenses, perform complete excitation by using more laser power (increase to 1 from the current 0.8), choose to excite and collect from an edge Zeeman state which requires no π filtering (for e.g. $|P_{3/2}, -3/2\rangle$ resulting in an increase to 0.74 from the current 0.49), choose a 50 ns detection window (to increase the yield to 1 from 0.7), use a sympathetic coolant to avoid re-cooling interruptions (increasing duty cycle to 1 from 0.3), and by using

SNSPDs for photon detection (90% efficiency as compared to the current 70%). With these improvements and starting from the time-bin rate of 0.35 s^{-1}, multiplying the appropriate numbers with the correct powers we obtain, $0.35s^{-1} \times 2 \times (0.45/0.19)^2 \times (1/0.8)^2 \times (0.74/0.49)^2 \times (1/0.7) \times (1/0.3) \times (0.9/0.7)^2 \times (1\text{ MHz}/70\text{ kHz}) = 1511\ s^{-1}$. It will probably be easier to use cavity based photon extraction to exceed 1 kHz entanglement rates. At that point multiplexing can be used to get into 10s of kHz which will then become comparable to local two qubit entangling gate speeds in ion traps, at the cost of using more ions.

In the next chapter, we extend this scheme to multiple time bins, making it easy to interface with high-dimensional quantum registers [86, 172]. That flexibility lets us generate complex entangled qudit states for advanced networking [173] and quantum computing tasks [174].

8

Higher dimensional quantum networking of atoms

This chapter is based on the preprint "Photonic Networking of Quantum Memories in High-Dimensions". [175]

In Chapter 7, we explored the challenge of creating remote entanglement between our trapped ion-based quantum memories. While encoding quantum information in a photon's polarization is a relatively straightforward approach, it comes with a significant problem: the polarization state is fragile and easily scrambled by the unavoidable birefringence in different optical elements. This poses a problem in building a large and reliable quantum network where qubits are entangled with low error rates, enabling distributed quantum computing [176].

To address this, we utilized time-bin encoding as a promising alternative. By encoding information in the time degree of freedom, we are robust against almost all unitaries. This is due to the difficulty of mixing information which are light-like separated (possible only via electromagnetic interaction). This chapter describes the experimental realization of this idea, but with an extension: we move beyond two-level qubits to harness the rich energy level structure of our $^{138}Ba^{+}$ions to create and network high-dimensional quantum systems, or "qudits".

Qudits have d-distinct levels, instead of the usual two in a qubit [177]. Thus, their Hilbert space grows as d^n instead of 2^n for qubits. This may have advantages: more efficient resource utilization via a higher-dimensional Hilbert space may allow the discovery of novel, resource-friendly algorithms and simulation techniques [43, 98, 172,

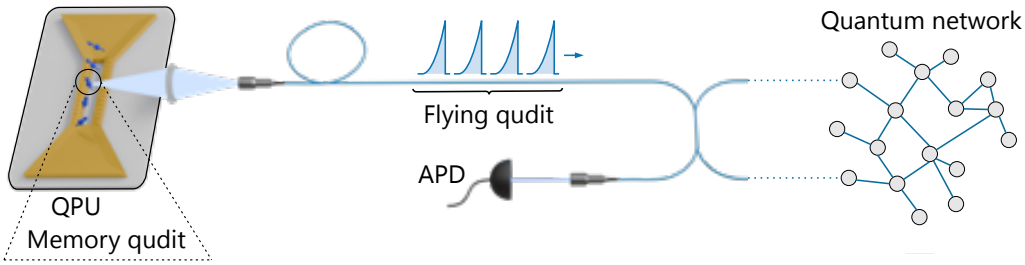

FIGURE 8.1: **Representative diagram of quantum memory**: Interfacing with a quantum network via time-binned photons.

178, 179]. They may also be useful for new quantum networking applications: using the higher dimensional Hilbert state of the entangled atom-photon pair to distribute more quantum information per photon [113, 180] and quantum key distribution [181, 182]. Memory implementations of qudits have been demonstrated in platforms such as superconducting Josephson Junctions where the anharmonicity of the quantum oscillators offers access to many levels [183, 184]. Many atomic species exhibit rich, multi-level structure that can be used as qudits [98]. While atoms, with their large number of long-lived atomic levels, can interface with optical photons, it can be challenging to do the same with superconducting qubits [185, 186]. Qudit entanglement via photons have been explored using atomic ensembles [187], however they are not practical for use in a quantum computer. On another side, high-dimensional (HD) photons have been realized via different degrees of freedom, e.g. frequency, time and angular momentum [113]. Two photons have been entangled in a massive 100x100 dimensional Hilbert space [188].

In this chapter, we describe our work on generating high-dimensional (HD) single photons encoded in time-bins and entangling them with single-atom qudit memories of dimension up to four. By operating two such spatially separated atom-photon qudit nodes, we create, interfere and detect these HD photons to probabilistically project the two distant atomic qudits into Bell-like entangled states. We achieve

qubit-entanglement fidelities as high as 0.987(13). Finally, we directly measure the photonic-qudit heralding success probability

$$\mathscr{F} = 1 - \frac{1}{d} \tag{8.1}$$

which exceeds the usual Bell-state limit of 1/2 for qubits.

I will detail our protocol for entangling an atomic qudit with a time-bin-encoded photon, the networking of two such remote memories, the high-fidelity results we achieved, and an analysis of the experimental results.

8.1 The Atom-Photon Interface: Creating a Flying Qudit

The core of our high-dimensional network is the ability to create a single photon whose quantum state is entangled with the state of an atomic qudit. First, we detail the experimental protocol we developed to achieve this, generating single photons encoded in up to four distinct time windows, or "time-bins", from a single trapped $^{138}Ba^{+}$ ion.

8.1.1 Qudit Levels

To host our high-dimensional quantum state, we take advantage of the rich energy level structure of the $^{138}Ba^{+}$ ion. We encode the qudit states across the ground and metastable electronic manifolds, similar to what we did in the last chapter. As shown in the level diagram in Fig. 8.2, we define our qudit states as:

- $|0\rangle \equiv |^2S_{1/2}, m_J = -1/2\rangle$
- $|\{1,2,3\}\rangle \equiv |^2D_{5/2}, m_J = \{-1/2, -3/2, +1/2\}\rangle$

The ground state, $|0\rangle$, serves as our "bright" state. It has a strong, fast transition to the excited state $|e\rangle \equiv |^2P_{1/2}, m_J = +1/2\rangle$ that we can drive with our pulsed 493 nm laser light to reliably produce a time-bin photon, exactly as before. The other states, $|1\rangle$, $|2\rangle$, and $|3\rangle$, are stored in the long-lived metastable $^2D_{5/2}$ manifold. This structure allows us to use the bright $|0\rangle$ state as a temporary bus for generating

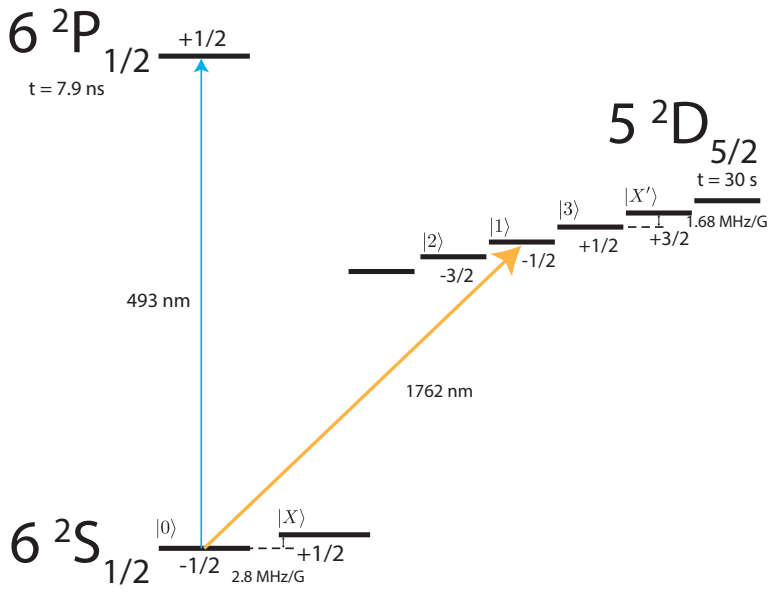

FIGURE 8.2: **Scheme for qudit-photon entanglement generation:** A single level in the ground S level $|0 \equiv S_{1/2}, m_j = -1/2\rangle$ is used for single photon generation. Additional levels in $D_{5/2}$ are used to encode the other qudit states $|1\rangle, |2\rangle, |3\rangle$. Note that we use $|X\rangle = |S_{1/2}, m_J = 1/2\rangle$ level as an error state which we shelve to $|X'\rangle = |D_{5/2}, m_j = 3/2\rangle$, rendering the atom dark during state detection.

a photon entangled with any of the qudit states.

For error-mitigation purposes, we also define two additional states: an error state in the ground manifold, $|X\rangle \equiv |^2S_{1/2}, m_J = +1/2\rangle$, and a corresponding error state in the metastable manifold, $|X'\rangle \equiv |^2D_{5/2}, m_J = +3/2\rangle$. As we will discuss later, these states are used for error-erasure that significantly improves our final fidelity [154].

8.1.2 Qudit-HD photon entanglement

Generating a time-bin photon that is entangled with our atomic qudit follows exactly the same protocol as described in the previous chapter. We now simply extend it to the d-dimensional case as shown in Fig. 8.3.

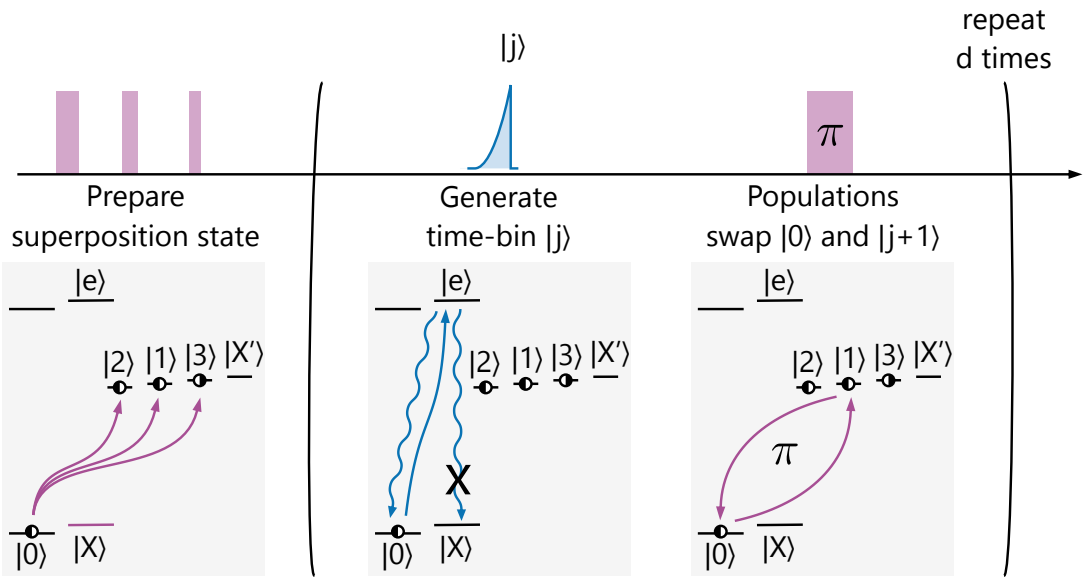

FIGURE 8.3: **Qudit time-bin generation:** After optically pumping into $|0\rangle$, we create an equal superposition by transferring an appropriate population into $|1\rangle, |2\rangle, |3\rangle$ sequentially. To generate entangled high dimensional photons, we excite $|0\rangle$ to $|e\rangle$ and collect any σ^+ emission. After this we swap $|0\rangle \leftrightarrow |j\rangle \forall j \in \{1, 2, 3\}$ and repeat the last two steps, d times for a d-dimensional qubit.

Protocol: Qudit Entanglement Generation

1. Cool and initialize qubits in $|0\rangle$ state.
2. Create an equal superposition $|\psi_0\rangle = \frac{1}{\sqrt{d}} \sum_{j=0}^{d-1} |j\rangle$.
3. Apply excitation pulse to transfer $|0\rangle$ to a short lived state $|e\rangle$.
4. Collect any spontaneous emission.
5. Swap populations between $|0\rangle \leftrightarrow |i\rangle$; $i \subset 0, 1, 2, 3$ using a π pulse.
6. Repeat steps 3-5 until all qudit levels gets swapped and excited.

1. Initialization and state preparation: The experiment begins by Doppler cooling the ion with 493 nm and 650 nm light. We then optically pump the atom into the $|0\rangle$ state. Using a series of carefully calibrated pulses from our 1762 nm laser, we prepare the ion in an equal superposition of all d qudit states: $|\psi_0\rangle =$

$\frac{1}{\sqrt{d}} \sum_{j=0}^{d-1} |j\rangle$. This is done by sequentially driving transitions between $|0\rangle$ and $|j\rangle$ states of the qudit. For d dimensions, assuming a π-time t_π, we drive a 1762 pulse of duration $t = \frac{2t_\pi}{\pi} cos^{-1}(1/\sqrt{d})$ between $|0\rangle$ and $|i\rangle \quad \forall i \in [1, 2, 3]$ with zero phase.

2. Generate the first time-bin: A single 3 ps, σ^+-polarized 493 nm laser pulse from our excitation laser is sent to the ion. This pulse is resonant with the $|0\rangle \rightarrow |e\rangle$ transition. If the atom was in the $|0\rangle$ state, it gets excited with a probability p and then spontaneously decays, emitting a photon. This time-bin, arrives in the $|0\rangle$ time window, has a characteristic exponential decay time of 7.86 ns, and is now entangled with the atomic state $|0\rangle$.
3. Swap and Excite for Subsequent Time-Bins: To generate the next time-bin, we apply a π-pulse with the 1762 nm laser to swap the populations of the $|0\rangle$ and $|1\rangle$ states. We then fire another 493 nm excitation pulse. Now, any population that was originally in the $|1\rangle$ state is in the bright state and will be correlated with the second time-bin. This "swap-and-excite" process is repeated for all the remaining qudit states [48].

A major experimental challenge here is dealing with the arbitrary phase due to the "atomic recoil". As discussed in Chapter 7, this recoil can entangle the atom's internal state with its motion in the trap, which will lead to an irreversible loss in fidelity of both the atom-photon and atom-atom entangled state, unless accounted for. To prevent this, we must ensure the atom's motion completes a full circle in phase space between photon emissions. We achieve this by carefully setting the time separation between our excitation pulses to be synchronous with the atom's motional time period. For this experiment, we used a time-bin separation of $\tau = 5680$ ns, which is commensurate with the period of atomic motion. This effectively erases any "which-path" information that could be encoded in the atom's motion, thereby

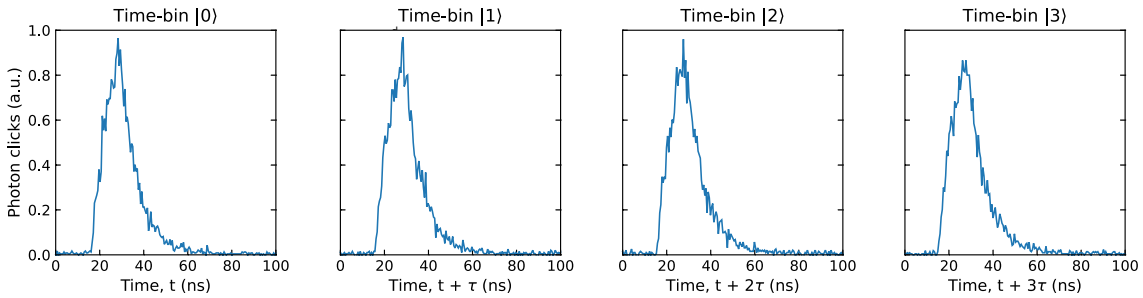

FIGURE 8.4: **High dimensional photons in time:** Arrival times of 6106 single photon detection events at different time windows separated by $\tau = 5680$ ns. These time-binned photons have an exponential decay of $t = 7.86$ ns due to the excited state lifetime, which are smeared out due to electronic response times.

recovering the entangled state fidelity [154, 158, 189, 190]. The resulting photon arrival histogram, clearly showing four distinct time-bins, is displayed in Fig. 8.4.

We collect the photon emitted from the atom using a high-numerical-aperture objective and couple it into a single-mode optical fiber. If a photon is successfully collected, the atom and photon are ideally left in the maximally entangled state:

$$|\psi\rangle_{\text{atom-photon}} = \frac{1}{\sqrt{d}} \sum_{j=0}^{d-1} |j\rangle^{(a)} |j\rangle^{(p)}, \tag{8.2}$$

where $|j\rangle^{(a)}$ is the state of the atomic qudit and $|j\rangle^{(p)}$ denotes a photon detected in the j^{th} time-bin. This entangled atom-photon pair is the fundamental building block for our network.

In our two-node experiment, we generate two of these entangled pairs in two separate systems, which we label A and B. The end-to-end probability of collecting and detecting a photon from each system is $p_A = 0.005$ and $p_B = 0.007$. These probabilities are a product of several factors, including the solid angle of our collection optics, losses in the optical path, and the quantum efficiency of our detectors, as shown in Table 8.1. Based on the fidelity of the final remote entangled state between the two atoms (which we will discuss in the next section), we can infer a lower bound

Table 8.1: Photon collection and detection efficiencies p_A and p_B.

Component	System A	System B
Lens solid angle	0.1	0.2
Fiber coupling	0.30(4)	0.20(3)
Trap clipping	0.78(2)	0.97(1)
Optical losses	0.90(2)	0.80(2)
APD quantum efficiency	0.65(3)	0.65(3)
Excitation probability	0.70(5)	0.70(5)
Branching ratio	0.486	0.486
Total	$p_A = 0.0047(8)$	$p_B = 0.0069(12)$

on the fidelity of our initial atom-photon entangled states. Using the methods similar to [191], we find these fidelities to be $F > \{0.959, 0.931, 0.913\}$ for qudit dimensions $d = \{2, 3, 4\}$, respectively. This confirms that we are generating entangled pairs which are now ready to be used for quantum networking.

8.2 Networking Qudit Memories

Using the the method described above, for creating a HD entangled pair between a single atom and a photon, we next utilize it to entangle two remote atoms with each other. One possible way to do this is to overlap the two photons at a beam splitter and wait for coincident clicks, projecting the atoms in an entangled state, analogous to a Bell State Measurement. The difference between this technique and the earlier ones is that we now expect a greater number of detection patterns, corresponding to the greater number of levels the atom can be entangled in.

8.2.1 The Experimental Setup and Protocol

We entangle two qudit memories of dimensions d upto four using the same setup as the qubit experiment, shown schematically in Fig. 8.5. In each node, we perform the atom-photon entanglement protocol we described earlier. The single photons emitted from each atom are collected and coupled into single-mode optical fibers.

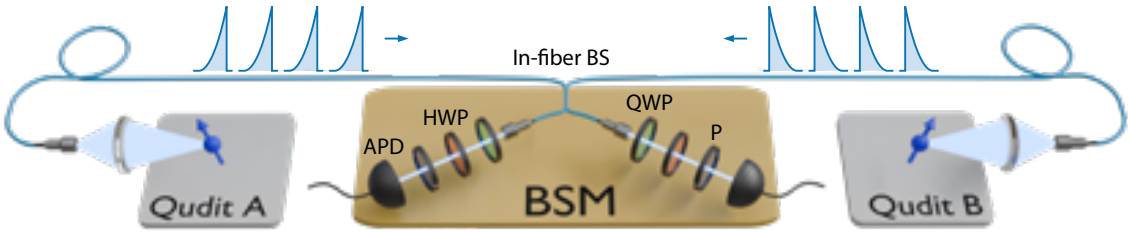

FIGURE 8.5: **Remote entanglement mediated by high dimensional photons**

These fibers guide the photons to a Bell state analyzer where they are interfered on a 50:50 in-fiber beamsplitter and sent to a set of avalanche photodetectors (APDs) where two photons in different time-bins $|n\rangle$ and $|m\rangle$ are detected.

We run the atom-photon generation sequence on both nodes at the exact same time. We Doppler cool and initialize the atoms in $|0\rangle$. After this we prepare each atom in an equal superposition of its d qudit states. The combined two-atom state can be written as:

$$|\psi_0\rangle = \frac{1}{d}\left(\sum_{j=0}^{d-1} |j\rangle_A^{(a)}\right) \otimes \left(\sum_{q=0}^{d-1} |q\rangle_B^{(a)}\right) \tag{8.3}$$

where the superscript (a) denotes an atomic state, and the labels $\{A, B\}$ refer to the atoms in the two nodes.

Next, we generate the time-bin photons as described before. The process of emitting a photon in time-bin $|j\rangle$ can be described by the operator:

$$A_j = |j\rangle^{(a)} \langle j|^{(a)} \left(\sqrt{p} e^{i\mathbf{\Delta k}\cdot\mathbf{r}_{A,B}(t_j)} c_j^\dagger + \sqrt{1-p}\right) + \sum_{q\neq j}^{d-1} |q\rangle^{(a)} \langle q|^{(a)} \tag{8.4}$$

Here, p is the overall probability of detecting the photon, $c_j^\dagger$ is the photon creation operator for time-bin j, $\mathbf{\Delta k} = \mathbf{k}' - \mathbf{k}$ is the wavevector difference from the excitation and emission process, and $\mathbf{r}_{A,B}(t_j)$ is the position of the atom at the time of emission t_j. The first term therefore describes the case when the atom gets excited, and its emitted photon collected and detected resulting in a momentum kick as well. The

second term describes the case when excitation has failed. The third term keeps the atom's state which are not in the j^{th} level, intact.

Let's consider the state after the first photon has been successfully collected from one of the the atoms in the time-bin, n. The joint state of the two atoms and their corresponding photons at the input of the beamsplitter is:

$$|\psi_1\rangle = |n\rangle_A^{(a)} \left(\sum_{j>n}^{d-1} |j\rangle_B^{(a)} \right) |n\rangle_A^{(p)} e^{i\phi_{A,n}} + |n\rangle_B^{(a)} \left(\sum_{j>n}^{d-1} |j\rangle_A^{(a)} \right) |n\rangle_B^{(p)} e^{i\phi_{B,n}} \tag{8.5}$$

where $\phi_{\{A,B\},n} = \mathbf{\Delta k} \cdot \mathbf{r}_{\{A,B\}}(t_n) + \phi_{\{A,B\}}^{\text{opt}}$ accounts for both the motional and optical phases acquired by the photon. The photons are then interfered on the beamsplitter, which performs the transformation $|n\rangle_{\{A,B\}} \rightarrow (|n\rangle_C \pm |n\rangle_D)/\sqrt{2}$, where A, B are the input ports corresponding to the two nodes and C,D are the output ports. The state after the beamsplitter, conditioned on a single photon detection in one of the output modes (say, C), is:

$$|\psi_2\rangle \propto |n\rangle_C^{(p)} \left(|n\rangle_A^{(a)} \sum_{j>n}^{d-1} |j\rangle_B^{(a)} e^{i\phi_{A,n}} + |n\rangle_B^{(a)} \sum_{j>n}^{d-1} |j\rangle_A^{(a)} e^{i\phi_{B,n}} \right) \tag{8.6}$$

Finally, after the population swap and a second excitation pulse, a second photon is detected in a later time-bin, $m > n$. This heralds the creation of a maximally entangled Bell state between the two remote atomic memories. The final state of the two atoms, conditioned on the photon detection pattern, is:

$$|\psi_3\rangle = (|n\rangle_A^{(a)} |m\rangle_B^{(a)} e^{i\Delta\phi} \pm |m\rangle_A^{(a)} |n\rangle_B^{(a)})/\sqrt{2} \tag{8.7}$$

where the differential phase is $\Delta\phi = (\phi_{A,n} - \phi_{A,m}) - (\phi_{B,n} - \phi_{B,m})$. The sign depends on which detectors clicked: (+) for the same detector clicking on different time bins, and (-) for different detectors clicking on different time bins. It is important to note that because of the swap pulses used to generate the time-bins, the final atomic states are advanced, so a detection in time-bins (n, m) actually corresponds to the atomic state involving levels $(n+1, m+1)$ mod d. All of these steps are illustrated in Fig. 8.6.

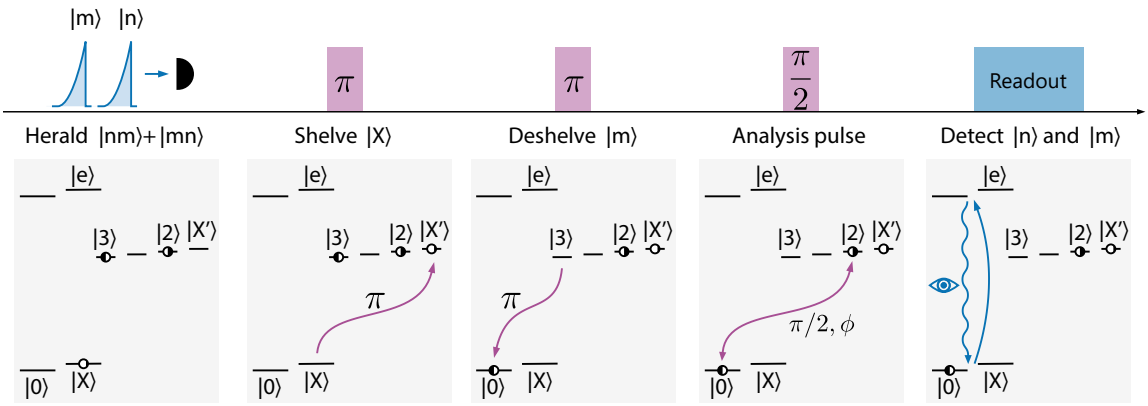

FIGURE 8.6: **State analysis pulse sequence:** Once we get photon clicks in time bins n and m (2,3 for example), we proceed with state analysis. First we shelve the error state $|X\rangle \rightarrow |X'\rangle$. After that we bring the state m (m>n, since m has a higher magnetic field sensitivity) back into $|0\rangle$. This is followed with an analysis $\pi/2$ pulse with a varying phase between the appropriate states ($|0\rangle \leftrightarrow |2\rangle$), and state detection.

8.2.2 Entanglement results

Once an entanglement is heralded (for states n,m), we need to verify that we have actually created the state we intended. We do this by measuring the final state of the two atomic qudits. This is performed in two-steps. First, we use 1762 nm laser to coherently transfer the populations from level m (>n) to the ground state. We perform a standard fluorescence measurement to check if either of the atom was in level m. Note that we shelve the higher labeled state to the ground level first, since it has a higher magnetic field sensitivity. We repeat the same procedure for the atom in level n. We discard trials in which either of the atoms are dark. Our state detection fidelity is better than 99%, including any imperfections from the population transfer pulses.

To quantify the quality of our entangled state, we measure its fidelity, F, with respect to the ideal Bell state. The fidelity is given by $F = (P + C)/2$, where P is the population in the correct basis states (i.e., the probability of finding the atoms in either $|n\rangle_A |m\rangle_B$ or $|m\rangle_A |n\rangle_B$), and C is the contrast of parity oscillations between

these two states [166].

We perform a parity scan between the level n,m by applying an analysis $\pi/2$ pulse with a variable relative phase $\Delta\phi$ to both atoms before performing the state detection. We construct the parity observable from Eq. 6.10, and extract its contrast, to obtain the fidelity of the entangled state.

All of the results for these measurements, for qudit dimensions $d = 2, 3$, and 4 are shown in Fig. 8.7. We also show the calculated populations, parity contrasts and fidelities of all the heralded states in Tab. 8.2. Additionally we also plot the distribution of the states right after the heralding and after the analysis pulses in the set of figures given in 8.9, 8.8. We observed fidelities, ranging from 0.849(23) to an excellent 0.987(13), without correcting for any state preparation or measurement errors.

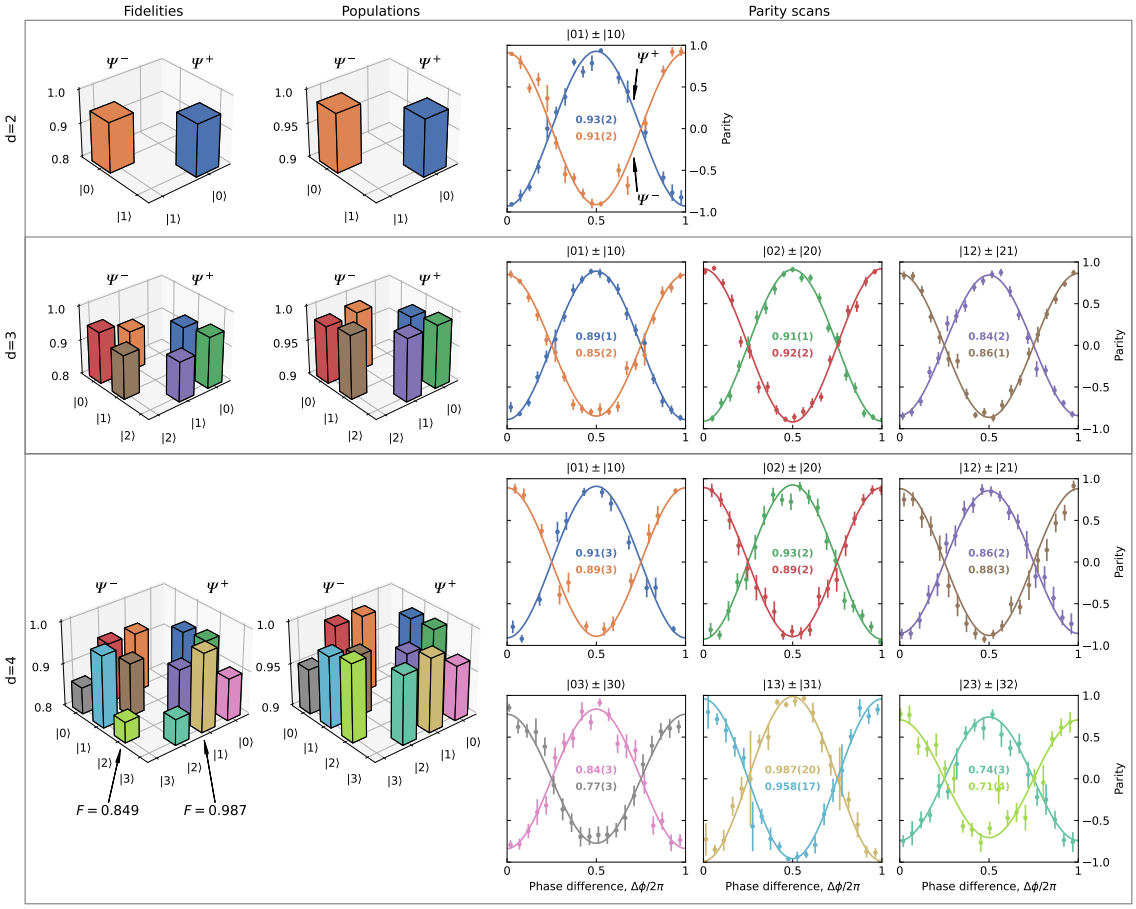

FIGURE 8.7: **Qudit entangled state analysis.** We measure the fidelity of each entangled qudit state $\Psi^{\pm} = |n\rangle_A |m\rangle_B \pm |m\rangle_A |n\rangle_B$ for dimensions $d = \{2, 3, 4\}$, displayed on the left column for each value of n and m. The fidelities are calculated from the population measurements (middle column) and the contrast of the parity scans (right column). The fidelity and population box plots represent the the fidelity and population measurements for different qudit levels which are represented by different column numbers of the boxes. The parity scans show the parity as we scan the relative phase between the analysis pulses on the two ions. The plots are all color coded to represent the same qudit levels. The parity oscillations are measured after an analysis $\pi/2$ pulse on each atom with a phase difference $\Delta\phi$ between them. The box diagram on the left read as follows: a given box at row/column:m/n denotes the results of the state $|n\rangle_A |m\rangle_B \pm |m\rangle_A |n\rangle_B$. All data includes state preparation and measurement errors.

Table 8.2: Qudit state results: Measured fidelities, populations, and contrasts for each entangled Bell state for qudit dimensions $d = \{2, 3, 4\}$.

Dimension $d = 2$

State	Fidelity	Populations	Contrast
$\|01\rangle + \|10\rangle$	0.950 (19)	0.986 (6)	0.909 (33)
$\|01\rangle - \|10\rangle$	0.941 (15)	0.988 (5)	0.891 (26)

Dimension $d = 3$

State	Fidelity	Populations	Contrast
$\|01\rangle + \|10\rangle$	0.950 (19)	0.984 (8)	0.909 (33)
$\|01\rangle - \|10\rangle$	0.941 (15)	0.987 (8)	0.891 (26)
$\|02\rangle + \|20\rangle$	0.959 (13)	0.993 (5)	0.925 (23)
$\|02\rangle - \|20\rangle$	0.943 (11)	0.984 (8)	0.893 (17)
$\|12\rangle + \|21\rangle$	0.917 (13)	0.992 (6)	0.857 (17)
$\|12\rangle - \|21\rangle$	0.927 (18)	0.993 (5)	0.881 (26)

Dimension $d = 4$

State	Fidelity	Populations	Contrast
$\|01\rangle + \|10\rangle$	0.950 (19)	0.991 (5)	0.909 (33)
$\|01\rangle - \|10\rangle$	0.941 (15)	0.992 (5)	0.891 (26)
$\|02\rangle + \|20\rangle$	0.959 (13)	0.993 (4)	0.925 (23)
$\|02\rangle - \|20\rangle$	0.943 (11)	0.992 (5)	0.893 (17)
$\|12\rangle + \|21\rangle$	0.917 (13)	0.977 (9)	0.857 (17)
$\|12\rangle - \|21\rangle$	0.927 (18)	0.973 (9)	0.881 (26)
$\|03\rangle + \|30\rangle$	0.901 (18)	0.966 (10)	0.836 (27)
$\|03\rangle - \|30\rangle$	0.864 (18)	0.953 (11)	0.774 (25)
$\|13\rangle + \|31\rangle$	0.987 (13)	0.988 (6)	0.987 (20)
$\|13\rangle - \|31\rangle$	0.971 (12)	0.985 (7)	0.958 (17)
$\|23\rangle + \|32\rangle$	0.862 (18)	0.982 (7)	0.741 (29)
$\|23\rangle - \|32\rangle$	0.849 (23)	0.993 (4)	0.706 (41)

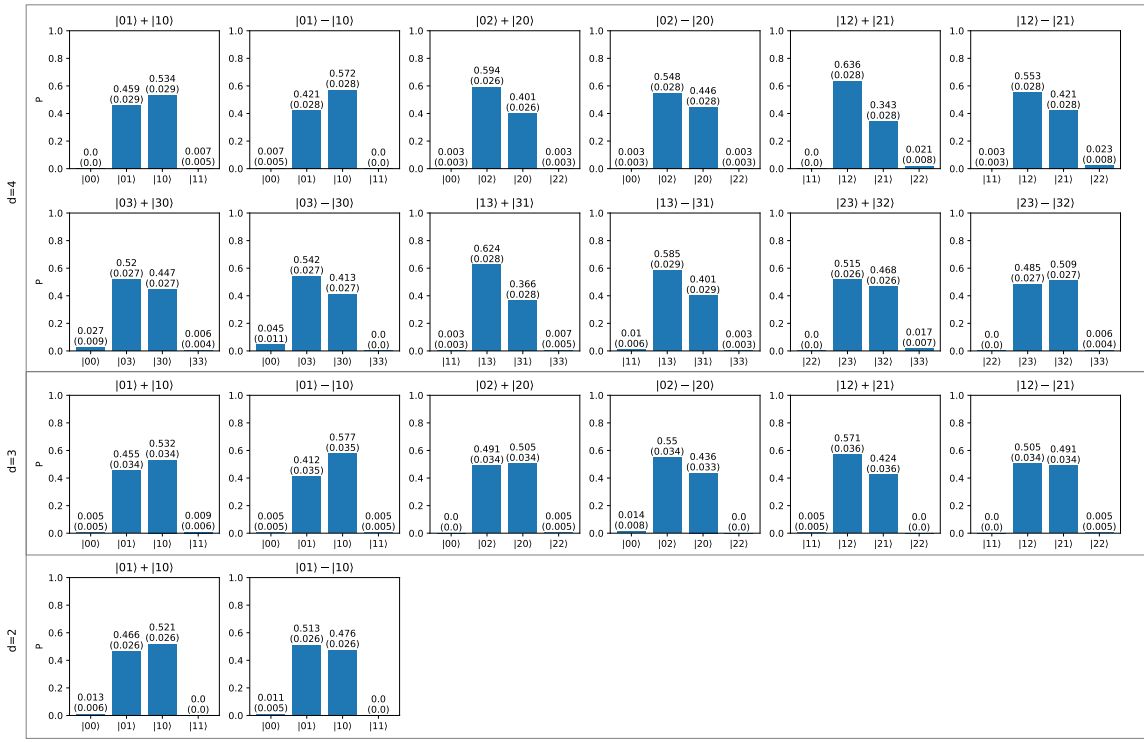

FIGURE 8.8: The states of atoms A and B after the entanglement heralding. Here, we plot the populations of specific qudit levels.

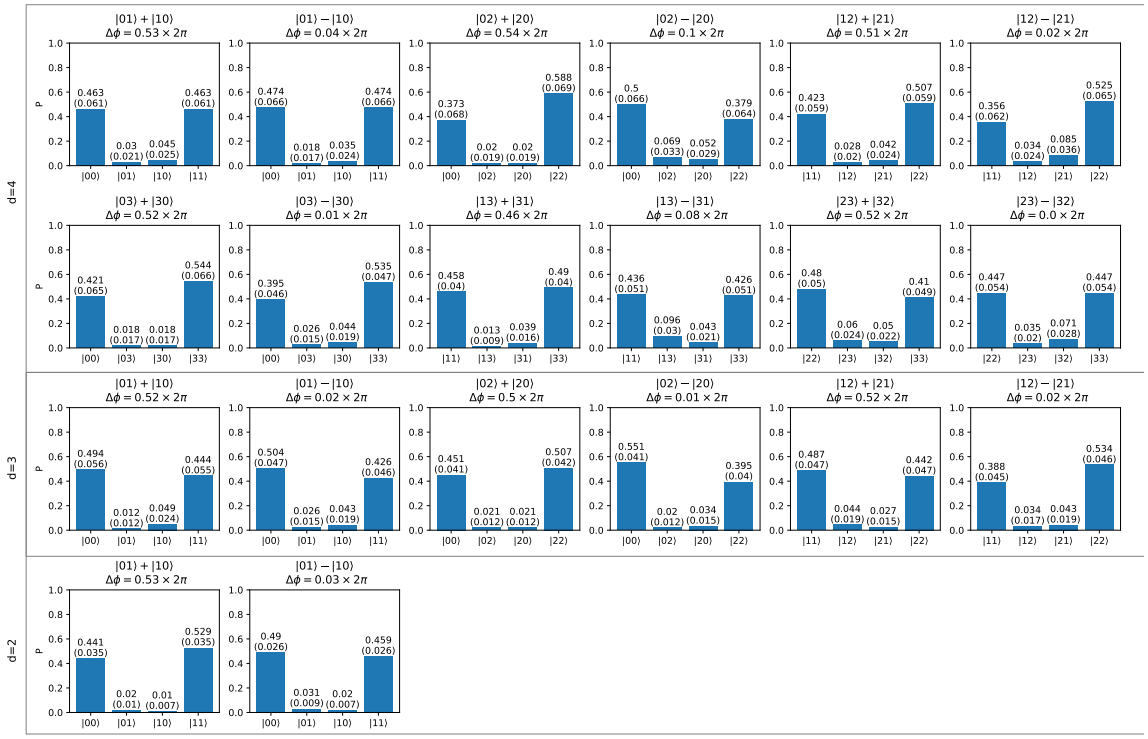

FIGURE 8.9: The states of atoms A and B after entanglement heralding followed by analysis $\pi/2$-rotation with the phase difference $\Delta\phi$. We again plot the populations of the different qudit levels after specific analysis sequence.

8.2.3 Experimental error sources

We observed the following error sources:

8.2.3.1 Magnetic field drift

Although the symmetric nature of our heralded Bell states makes them robust against common-mode magnetic field noise that affects both atoms equally, we found that slow, differential drifts in the magnetic field between the nodes were a dominant source of error. This differential field can cause the relative phase of the entangled state to drift over the duration that we take experimental data, causing our phase to gradually drift as well. We can write the heralded state at the time of analysis, T, as:

$$|\psi(T)\rangle = \frac{|n\rangle_A |m\rangle_B \pm e^{-i\phi} |m\rangle_A |n\rangle_B}{\sqrt{2}}. \tag{8.8}$$

Table 8.3: Bell state phase sensitivities to magnetic field for all heralded states and qudit dimension $d = \{2, 3, 4\}$. These are given by the magnetic g-factors of the relevant states along with dwell times for shelving and swapping operations for each protocol.

	Phase sensitivity (rads/mG), γ_{nm}		
Heralded Bell state	d=4	d=3	d=2
$\|10\rangle \pm \|01\rangle$	0.31	0.61	0.49
$\|20\rangle \pm \|02\rangle$	-1.24	-0.92	–
$\|30\rangle \pm \|03\rangle$	1.71	–	–
$\|12\rangle \pm \|21\rangle$	1.64	1.65	–
$\|13\rangle \pm \|31\rangle$	-0.50	–	–
$\|23\rangle \pm \|32\rangle$	-3.22	–	–

The accumulated phase, $\phi = \delta B \gamma_{nm} T$, depends directly on this field difference. Here δB is the average magnetic field difference between the two qudit positions A and B over the time T it takes for the analysis to fire after a heralding event.

The sensitivity factor, γ_{nm}, is unique to each heralded Bell state. It depends not only on the relative Zeeman shifts of the specific atomic levels $|n\rangle$ and $|m\rangle$ involved, but also on the entire sequence of shelving and swapping pulses and therefore the time that each of the qudit states spend in different magnetic field sensitive states. This results in a predictable effective magnetic field sensitivity γ_{nm} for each state, which we summarize in Table 8.3.

If left uncompensated, this slowly drifting phase would average out our parity measurements, over the long duration of a data run, lowering the fidelity. To bypass this issue, and extract the true fidelity of the entangled state (fidelity of the state at the instant they were heralded), we post process our data. We make a reasonable assumption that the magnetic field drifts on a timescale much slower than our entanglement generation rate. This allows us to treat δB as constant for a given data set but variable over the course of the entire experiment. For each point in time during our data acquisition, we determine the value of δB that best fits the ob-

served phase drifts across *all* measured Bell states simultaneously, using their known relative sensitivities from Table 8.3.

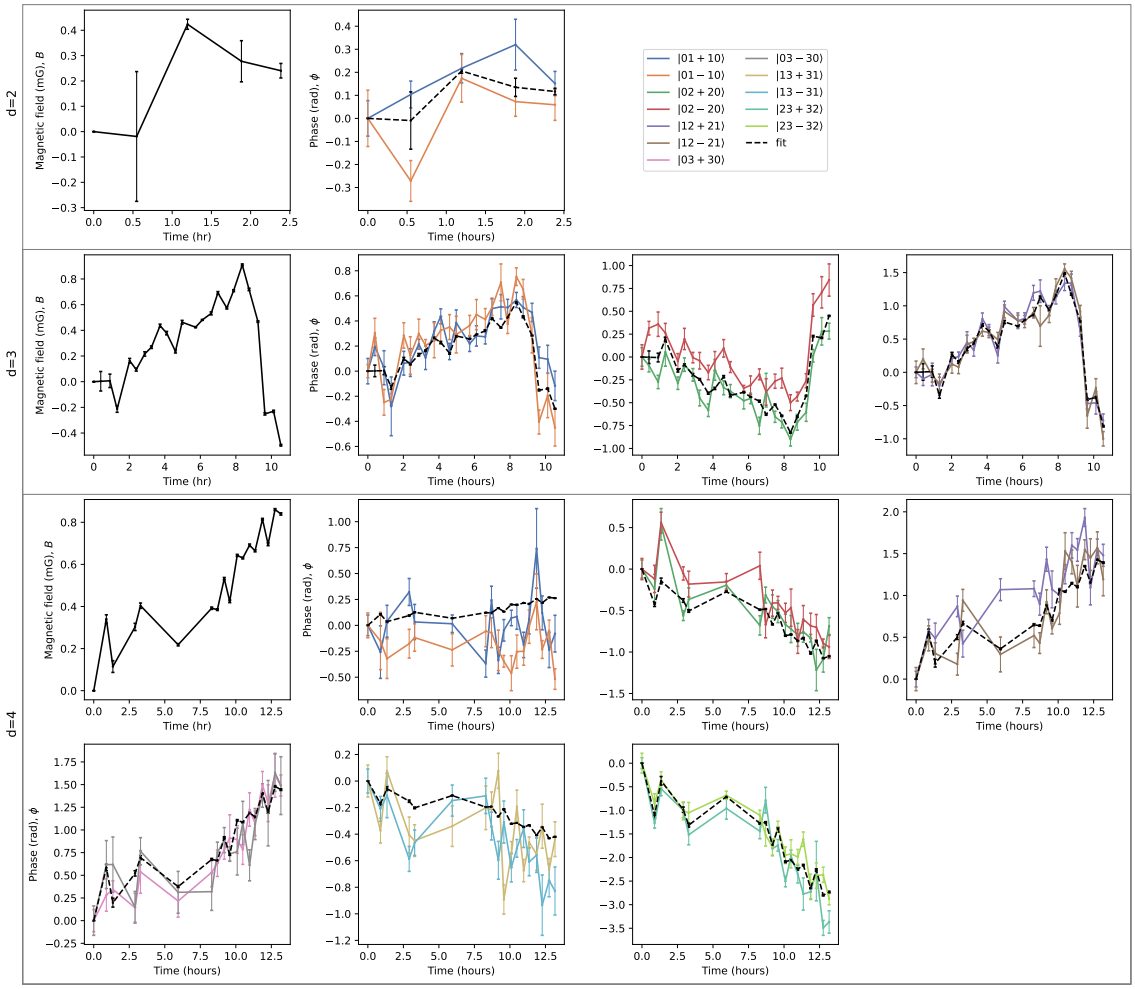

FIGURE 8.10: **Differential magnetic field drift and phase feed-forward.** Solid points are measured phase drifts of all entangled state coherences for qudit dimensions $d = 2, 3, 4$. Here we plot the estimated magnetic fields as it drifts in time. The dashed lines are fits of the state phases at each point in time to a particular differential magnetic field δB between the two systems that minimizes the deviation from the phase shift $\phi = \delta B \gamma_{nm}(d) T$ using the state sensitivities from Table 8.3. The fitted differential magnetic field is shown in the first plot of each family of plots.

This feedforward adjustment effectively re-phases the entangled states, allowing us to recover the true parity contrast, and therefore it's fidelity (at the time the state

was heralded). Fig. 8.10 shows the measured phase evolution for each Bell state over several hours. A single fitted differential magnetic field correctly captures the drift for all states, demonstrating the validity of our assumption. For the most magnetically sensitive state, this rephasing procedure improved the measured coherence contrast by approximately 22%.

Alternatively we can avoid this issue by having magnetic field insensitive qubits or active magnetic field stabilizing hardware. All of the fidelity results presented in this thesis, including the populations and contrasts shown in Table 8.2 and Fig. 8.9, have been applied with this correction. It should be noted that the error bars shown in Figs. 8.8 and 8.9 are calculated assuming the Central Limit Theorem, which differs slightly from the method used for the values in Table 8.2.

8.2.3.2 Erasure errors

Owing to polarization mixing, there is a small chance, that when a photon is collected, the population lands in the wrong ground state $|X\rangle$, due to incorrect polarization filtering. This may be due to inhomogeneous birefringence of optical components such as vacuum windows which mixes σ^+ and π polarizations.

Therefore, after a successful entanglement herald before the final state measurement, we apply a "shelving" pulse that moves any population that has erroneously ended up in $|X\rangle$ to the dark metastable state $|X'\rangle$. Then, during fluorescence detection of states n and m, if an atom appears dark, we know an error must have occurred. We can then simply discard those experimental trials. This technique allowed us to reject [11.5, 6.4, 9.1]% of our data for d=[2,3,4]. By converting a state error into an erasure, we were able to increase our final fidelities.

8.2.3.3 Other Error Sources

As we increase the dimension d of our qudit, the protocol requires more population swapping pulses, and the error from each pulse accumulates. There are also errors

due to decoherence from fast magnetic field fluctuations. This is why we see state specific fidelity reduction depending on it's magnetic field sensitivity γ_{nm}. States which have higher magnetic field sensitivity will be more vulnerable to fast magnetic field noise and consequently yield lower fidelities. We also noticed a double-excitation error when the detected time-bins are adjacent ($m - n = 1$), caused by imperfect swapping pulses leaving some population behind in the ground state to be excited a second time. Consequently for entangled states for which $m - n > 1$, have a higher fidelity because the subsequent swap pulses act as a shelving pulse for the erroneous 'leftover' population. We again remind the reader that the final atomic states are different from the heralded time bin detections because of the swap pulses.

Bell states such as $|01\rangle \pm |10\rangle$ or $|13\rangle \pm |31\rangle$ are less sensitive to the effects mentioned above and therefore are on par with the very best remote entanglement fidelity benchmarks [154]. State like $|23\rangle \pm |32\rangle$ have $m - n = 1$ making it prone to errors from double excitation, require additional shelving pulses, and suffer from decoherence due to high magnetic field sensitivity, and ultimately result in reduced fidelity.

A complete breakdown of the error budget can be found in Table 8.4. We split errors into two categories: errors that are common to all entangled states and those which are specific to states residing in certain Zeeman levels, as we have already described. Common error sources contribute approximately 1.51% to total infidelity in all measurements. 0.5% of the common error sources are due to state preparation and measurement (SPAM), which is limited by our 1762 nm shelving fidelity to the detection dark state. Our dark-state discrimination error is negligible.

Table 8.4: Error budget.

Common errors (%)

SPAM	0.5
Photon wavepacket overlap	0.2
Atom recoil, $\delta t = 50$ ns	0.3
Background counts	< 0.2
Atom recoil, ω_{qi} fluctuation	< 0.1
Beamsplitter imperfection	< 0.1
Residual erasure errors	< 0.1
Micromotion	< 0.01
TOTAL common errors (%)	**1.51**

Errors for individual Bell states (%)

$d = 4$			
Bell state	Decoherence	1762 error	**TOTAL**
$\|01\rangle \pm \|10\rangle$	0.1	0.98	**2.59**
$\|02\rangle \pm \|20\rangle$	0.9	2.61	**5.02**
$\|12\rangle \pm \|21\rangle$	1.6	7.68	**10.79**
$\|03\rangle \pm \|30\rangle$	1.7	7.1	**10.31**
$\|13\rangle \pm \|31\rangle$	0.2	1.19	**2.9**
$\|23\rangle \pm \|32\rangle$	5.9	6.23	**13.64**
$d = 3$			
Bell state	Decoherence	1762 error	**TOTAL**
$\|01\rangle \pm \|10\rangle$	0.2	0.98	**2.69**
$\|02\rangle \pm \|20\rangle$	0.5	10.76	**12.77**
$\|12\rangle \pm \|21\rangle$	1.6	7.12	**10.23**
$d = 2$			
Bell state	Decoherence	1762 error	**TOTAL**
$\|01\rangle \pm \|10\rangle$	0.1	8.6	**10.21**

8.2.4 Entanglement Rate and the Trade-off of Higher Dimensions Rate and Success Probability

For any given attempt, the probability of successfully generating an entangled state between our two atoms is $P_{\text{ent}} = \mathscr{F} p_{\text{A}} p_{\text{B}}$, where p_A and p_B are the single-photon detection efficiencies for each system, and $\mathscr{F}$ is the heralding success fraction.

It is a known fact in quantum networking that when using standard linear optics, the Bell-state measurement for two qubits ($d = 2$) can only unambiguously distinguish two of the four possible Bell states [192, 193]. This puts a hard cap on the success fraction at $\mathscr{F} = 1/2$. While schemes have been proposed to get around this limit using resources like "ancillary" photons or complex nonlinear optical elements, these can add significant experimental complexity and overhead [100, 104, 194–201]. Our high-dimensional approach, however, offers a much more direct way to increase this efficiency.

When we interfere two d-dimensional photons, there are d^2 possible combinations of arrival times. The measurement only fails if both photons arrive in the *same* time-bin (e.g., both in time-bin 0, or both in time-bin 1, etc.), as these events are indistinguishable and do not herald entanglement. There are exactly d such failure cases. This leaves $d^2 - d$ successful heralding events, giving a theoretical success fraction of:

$$\mathscr{F} = \frac{d^2 - d}{d^2} = 1 - \frac{1}{d}. \tag{8.9}$$

This simple relation shows that for $d = 2$, we recover the 50% limit, but for $d = 3$ the success fraction increases to 66.7%, and for $d = 4$ it reaches 75%.

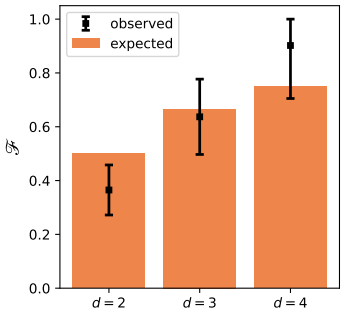

FIGURE 8.11: Measured Bell-state measurement (BSM) success fractions for qudit dimensions d=2,3,4 (black points and statistical error bars). The success fraction increases with dimension according to the theoretical scaling F = 1-1/d (orange bars), which reflects the fraction of distinguishable antisymmetric Bell states.

We directly verified this scaling in our experiment, with the results shown in Fig. 8.11. To extract the success fraction $\mathscr{F}$ from our data, we took our measured total success probability P_{ent} and divided out the independently measured efficiencies of our two systems, p_A and p_B (see Table 8.1, 8.5 for details). For $d = \{2, 3, 4\}$, we measured success fractions of $\mathscr{F} = \{0.37(11), 0.64(17), 0.90(24)\}$, respectively. These results agree well with the theoretical predictions and clearly demonstrate that our high-dimensional network surpasses the fundamental 50% limit.

While the success fraction $\mathscr{F}$ gets better with higher dimensions, there is a price to pay in the overall entanglement rate, R. Each additional time-bin we generate adds an overhead time, τ_{bin}, to our experimental cycle. The overall rate can be expressed as:

$$R = \frac{\mathscr{F} p_A p_B}{\tau_0 + \tau_{\text{bin}}(d-1)}, \tag{8.10}$$

where τ_0 is the base time for an entanglement attempt. This equation reveals a trade-off: as we increase d, the numerator gets larger, but so does the denominator. This means there is an optimal dimension that maximizes the entanglement rate, which depends on how quickly we can generate the extra time-bins.

In our setup, the entanglement rate is primarily limited by the speed of our population swap operations with the 1762 nm laser, and the need to keep our time-bin separation synchronized with the ion's motional periods to avoid decoherence. For $d = \{2, 3, 4\}$, our total entanglement cycle times were approximately $\tau_{\text{cycle}} \approx \{17.0, 22.7, 34.1\}$ μs, respectively. These times depend on the Rabi frequency of our 1762 nm laser, which we recalibrate regularly to ensure high-fidelity rotations. Further details on the rates and number of experimental trials can be found in Table 8.5.

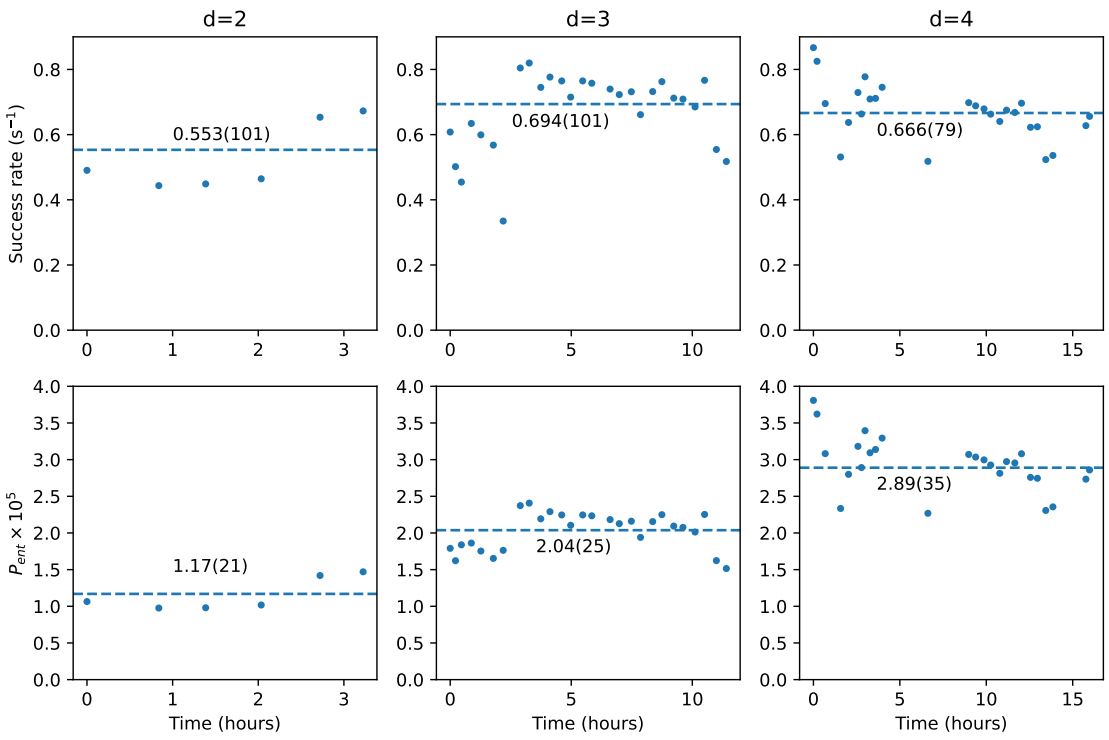

FIGURE 8.12: Remote entanglement rates and total entanglement success probabilities for dimensions $d = \{2, 3, 4\}$. Each point represents a separate data set collected over time. Dashed lines indicate the average entanglement rate for each qudit dimension.

Table 8.5: Experimental metrics for different qudit dimensions $d = \{2, 3, 4\}$. Attempt length increases with dimension due to the need for more swaps between levels. Wall-clock time and experimental entanglement rate are calculated with experimental overhead included. The entanglement generation success probability P_{ent} is computed from the number of successes and attempts.

d	Attempt length (µs)	Attempt rate (kHz)	Time (s)	Successes	Attempts	Experimental entanglement rate (s^{-1})	P_{ent} ($\times 10^{-5}$)
2	17	58	9,844	5,121	437,972,714	0.553	1.17
3	22.7	44	35,342	23,427	1,149,607,096	0.694	2.04
4	34.1	29	31,315	19,941	689,981,646	0.666	2.89

8.3 Outlook

The work presented in this chapter demonstrates that qudit memories and high-dimensional photons can expand the capabilities of quantum networks. We have shown a path to more efficient entanglement generation that is robust against the environmental noise. While we have focused on generating specific, two-level Bell-like states within our larger qudit space, the platform we have developed can be extended in several directions.

One straightforward extension is to generate entanglement that spans the entire d-dimensional space. This could be done, for example, by converting our time-bin photons into path encoded photons, which would allow for programmable, all-to-all interference that can herald the creation of arbitrary entangled qudit states [202].

Another promising avenue is to move away from two-photon interference altogether and use a "pitch-and-catch" scheme. In this approach, one atomic memory would emit a high-dimensional photon, which would then be directly absorbed by a second, remote memory. This would deterministically transfer the quantum state from one node to the other, offering a very different paradigm for state transfer [203–205].

Distributing these rich, high-dimensional entangled states across a network offers a powerful and resource-efficient toolkit for the future of scalable quantum information science. As we look ahead, these techniques may play an important role not only in building larger and more capable quantum computers, but also in enabling new forms of quantum communication and sensing.

9

Conclusion

In this thesis, we have explored the challenge of scaling quantum computing systems via photonic interconnects. We investigated two distinct schemes for heralding entanglement between spatially separated quantum computing nodes. By implementing these schemes in our quantum networking testbed using polarization-encoded photonic qubits, we achieved a proof-of-principle demonstration that set a new record for the entanglement rate between two quantum memories.

To mitigate the challenge of unpredictable polarization rotations in optical fibers, we transitioned to a time-bin encoding scheme. This implementation, however, faced unexpected limitations originating from the atomic recoil induced by photon emission—an effect not previously considered in heralding protocols. While typically negligible in non-time-bin schemes, these recoil effects become significant in our configuration, allowing us to derive fundamental limitations for such heralding processes. Despite this challenge, the time-bin scheme enabled us to herald Bell pairs with the highest fidelity reported to date, demonstrating a possible method for establishing high-fidelity remote entanglement.

Although our systems have independently set new benchmarks for both rate and fidelity, a significant gap remains before these protocols can be used to scale full-stack quantum computers. Achieving the required performance for fault-tolerant architectures necessitates reaching fidelities exceeding 99% while maintaining entanglement rates of several kilohertz. The following section outline a strategic path

toward achieving these goals.

9.1 Improving Fidelity: Frequency-Mediated Entanglement

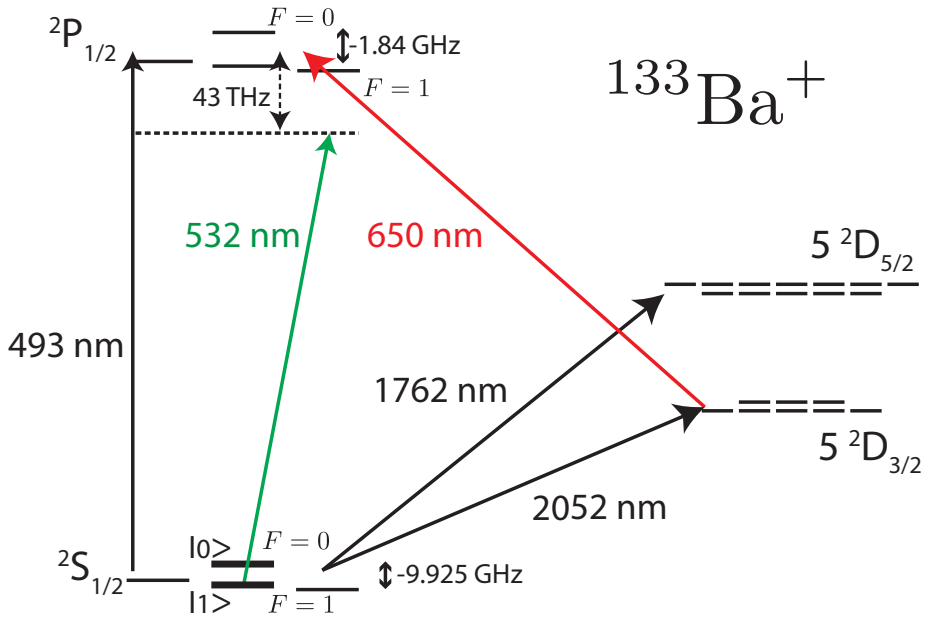

FIGURE 9.1: **Level diagram of** $^{133}Ba^+$

One way to enhance fidelity without compromising rate is to use frequency-binned photons. Similar to time-bin encoding, the frequency degree of freedom is robust against decoherence during transmission through optical components and fibers. This approach holds a distinct advantage over time-bin schemes as it does not require intermediate qubit swap pulses, which can slow down the entanglement generate rate.

Implementing a frequency-based scheme necessitates an atomic species which can generate photons with frequency differences large enough to be resolved by a high-finesse optical cavity or a diffraction grating. This resolvability is crucial to distinguish between different heralding outcomes. While heralding events where photons exit separate output ports of a beam splitter are readily identifiable, detecting events

where two photons of the same frequency exit the *same* port requires robust frequency separation. This has been experimentally demonstrated for frequency differences on the order of a few gigahertz. The isotopes Barium-137 ($^{137}Ba^{+}$) and Barium-133 ($^{133}Ba^{+}$) (see Fig. 9.1) are ideal candidates for such a scheme, as their ground-state hyperfine splittings of approximately 8 GHz and 10 GHz, respectively, are well-suited for high-fidelity photonic frequency-based entanglement.

A typical entanglement protocol would consider the qubit states as $|0\rangle \equiv |S_{1/2}, F = 0\rangle$ $|1\rangle \equiv |S_{1/2}, F = 1, m_F = 0\rangle$. We would initialize in $|0\rangle$ via frequency selective optical pumping, and excite with 493 nm σ^+ polarized light pulse to $|P_{1/2}, F = 1, m_F = 1\rangle$. Upon decay and collection of σ^+, σ^- polarized photons as H photons, we would get an entangled state where the two qubit states $|0\rangle, |1\rangle$ are entangled with photonic frequency qubits. We would simply interfere two of these photons (from two different atoms) on a beam splitter and perform appropriate detections to herald a Bell state between the two atoms. This scheme would not only use decoherence resistant frequency photons, but also avoid any of the motional syncing troubles required in time-bin schemes and at the same time herald Bell states in hyperfine qubits which already have superb coherence times.

9.2 Improving Rate: Cavity-Enhanced Repeater Nodes

The entanglement protocols discussed in this work have a success probability that scales as $P_{\text{success}} \propto R \cdot p^2$, where R is the entanglement attempt rate and p is the end-to-end probability of detecting a single emitted photon. For small p, this quadratic dependence severely limits the achievable entanglement rate. While alternative single-photon protocols can circumvent this, they typically do so by trading fidelity for rate.

A more effective architecture to overcome this limitation involves the introduction of a central quantum repeater node between the two computational nodes. The

purpose of this intermediary node, which must have a near-unity light collection and detection efficiency ($p \approx 1$), would be to mediate and distribute entanglement between any two nodes. By placing the most efficient node in the center, the overall success probability becomes linear in p, thereby dramatically increasing the net entanglement rate. The repeater node would be dedicated to generating entangled pairs between itself and another two nodes and would perform an entanglement swapping procedure in the end to leave the desired atoms entangled. Such an architecture would also simplify design challenges by physically seperating memory nodes and repeater(communication) nodes. A high-finesse optical cavity, which can efficiently couple photons from a quantum memory into a collection optic, would be necessary for such a high-efficiency repeater.

9.3 Future Work: GHZ State Preparation

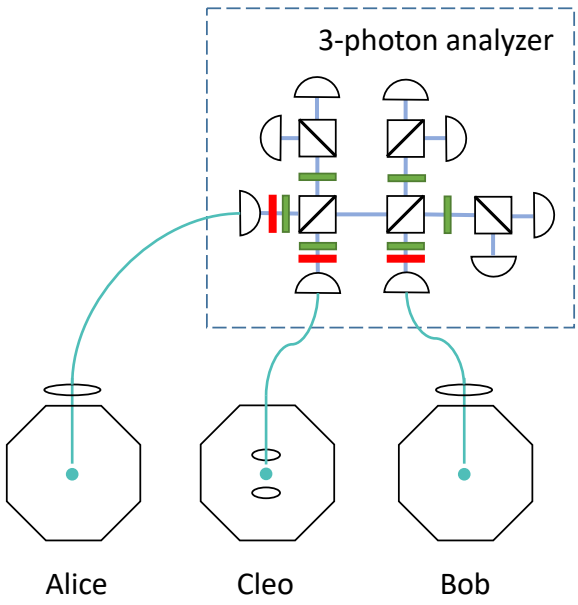

FIGURE 9.2: **Setup for GHZ state generation:** Single photons entangled with their parent atoms in their polarization degree of freedom are collected and sent to a 3-photon GHZ state analyzer via fibers. Upon a 3-photon coincidence and detection at the analyzer (in the correct pattern), the three atoms in three different chambers get projected into a GHZ state.

Our three-node quantum network is an ideal platform for pioneering experiments in distributed quantum information processing. A key near-term objective is the preparation and verification of a Greenberger-Horne-Zeilinger (GHZ) state across three atoms located in three separate modules. The protocol for this experiment builds upon the polarization-based entanglement scheme developed in this work. Photons entangled with the polarization state of their parent atom are collected from each of the three nodes and interfered on a sequence of two polarizing beam splitters. A successful three-photon coincidence detection event at specific output ports will project the three remote atomic qubits into a shared GHZ state, demonstrating a foundational capability for more complex quantum networks.

Bibliography

1. O'Reilly, J. *et al.* Fast Photon-Mediated Entanglement of Continuously Cooled Trapped Ions for Quantum Networking. *Phys. Rev. Lett.* **133,** 090802. https://link.aps.org/doi/10.1103/PhysRevLett.133.090802 (9 Aug. 2024).

2. Turing, A. On Computable Numbers, with an Application to the Entscheidungsproblem. *Proceedings of the London Mathematical Society* **42,** 230–265 (1936).

3. Church, A. An Unsolvable Problem of Elementary Number Theory. *American Journal of Mathematics* **58,** 345–363. https://www.jstor.org/stable/2371045 (1936).

4. Bardeen, J. & Brattain, W. H. Physical Principles Involved in Transistor Action. *Bell System Technical Journal* **28,** 239–277. https://archive.org/details/bstj28-2-239 (Apr. 1949).

5. Einstein, A., Podolsky, B. & Rosen, N. Can Quantum-Mechanical Description of Physical Reality Be Considered Complete? *Phys. Rev.* **47,** 777–780. https://link.aps.org/doi/10.1103/PhysRev.47.777 (10 May 1935).

6. Gerlach, W. & Stern, O. Der experimentelle Nachweis der Richtungsquantelung im Magnetfeld. *Zeitschrift für Physik* **9,** 349–352. https://doi.org/10.1007/BF01326983 (Dec. 1922).

7. Feynman, R. P. Simulating Physics with Computers. *International Journal of Theoretical Physics* **21,** 467–488. https://doi.org/10.1007/BF02650179 (1982).

8. Manin, Y. I. *Computable and Uncomputable* in Russian (Sovetskoye Radio, Moscow, 1980).

9. Deutsch, D. Quantum theory, the Church–Turing principle and the universal quantum computer. *Proceedings of the Royal Society of London. Series A, Mathematical and Physical Sciences* **400,** 97–117. https://doi.org/10.1098/rspa.1985.0070 (1985).

10. Shor, P. W. Polynomial-Time Algorithms for Prime Factorization and Discrete Logarithms on a Quantum Computer. *SIAM Journal on Computing* **26,** 1484–1509. eprint: https://doi.org/10.1137/S0097539795293172. https://doi.org/10.1137/S0097539795293172 (1997).

11. Cirac, J. I. & Zoller, P. Quantum Computations with Cold Trapped Ions. *Phys. Rev. Lett.* **74,** 4091–4094. https://link.aps.org/doi/10.1103/PhysRevLett.74.4091 (20 May 1995).

12. Monroe, C., Meekhof, D. M., King, B. E., Itano, W. M. & Wineland, D. J. Demonstration of a Fundamental Quantum Logic Gate. *Phys. Rev. Lett.* **75,** 4714–4717. https://link.aps.org/doi/10.1103/PhysRevLett.75.4714 (25 Dec. 1995).

13. Nakamura, Y., Pashkin, Y. A. & Tsai, J. S. Coherent control of macroscopic quantum states in a single-Cooper-pair box. *Nature* **398,** 786–788. https://doi.org/10.1038/19718 (Apr. 1999).

14. AI, G. Q. & Collaborators. Quantum error correction below the surface code threshold. *Nature* **638,** 920–926. https://doi.org/10.1038/s41586-024-08449-y (2025).

15. Barredo, D., de Léséleuc, S., Lienhard, V., Lahaye, T. & Browaeys, A. An atom-by-atom assembler of defect-free arbitrary two-dimensional atomic arrays. *Science* **354,** 1021–1023. eprint: https://www.science.org/doi/pdf/10.1126/science.aah3778. https://www.science.org/doi/abs/10.1126/science.aah3778 (2016).

16. Lukin, M. D. *et al.* Dipole Blockade and Quantum Information Processing in Mesoscopic Atomic Ensembles. *Phys. Rev. Lett.* **87,** 037901. https://link.aps.org/doi/10.1103/PhysRevLett.87.037901 (3 June 2001).

17. Bluvstein, D. *et al.* Logical quantum processor based on reconfigurable atom arrays. *Nature* **626,** 58–65. https://doi.org/10.1038/s41586-023-06927-3 (2024).

18. Loss, D. & DiVincenzo, D. P. Quantum computation with quantum dots. *Phys. Rev. A* **57,** 120–126. https://link.aps.org/doi/10.1103/PhysRevA.57.120 (1 Jan. 1998).

19. George, H. C. *et al. 12-spin-qubit arrays fabricated on a 300 mm semiconductor manufacturing line* 2024. arXiv: 2410.16583 [cond-mat.mes-hall]. https://arxiv.org/abs/2410.16583.

20. Press, D., Ladd, T. D., Zhang, B. & Yamamoto, Y. Complete quantum control of a single quantum dot spin using ultrafast optical pulses. *Nature* **456,** 218–221. https://doi.org/10.1038/nature07530 (Nov. 2008).

21. Chuang, I. L. & Yamamoto, Y. Simple quantum computer. *Phys. Rev. A* **52,** 3489–3496. https://link.aps.org/doi/10.1103/PhysRevA.52.3489 (5 Nov. 1995).

22. team, P. A manufacturable platform for photonic quantum computing. *Nature* **641,** 876–883. https://doi.org/10.1038/s41586-025-08820-7 (Feb. 2025).

23. Nayak, C., Simon, S. H., Stern, A., Freedman, M. & Das Sarma, S. Non-Abelian anyons and topological quantum computation. *Rev. Mod. Phys.* **80,** 1083–1159. https://link.aps.org/doi/10.1103/RevModPhys.80.1083 (3 Sept. 2008).

24. Kielpinski, D., Monroe, C. & Wineland, D. J. Architecture for a large-scale ion-trap quantum computer. *Nature* **417,** 709–711. https://doi.org/10.1038/nature00784 (June 2002).

25. Moses, S. A. *et al.* A Race-Track Trapped-Ion Quantum Processor. *Phys. Rev. X* **13,** 041052. https://link.aps.org/doi/10.1103/PhysRevX.13.041052 (4 Dec. 2023).

26. Nielsen, M. A. & Chuang, I. L. *Quantum Computation and Quantum Information: 10th Anniversary Edition* ISBN: 9781107002173 (Cambridge University Press, 2011).

27. González-Cuadra, D. *et al.* Observation of string breaking on a (2 + 1)D Rydberg quantum simulator. *Nature* **642,** 321–326. https://www.nature.com/articles/s41586-025-09051-6 (2025).

28. Manovitz, T. *et al.* Quantum coarsening and collective dynamics on a programmable simulator. *Nature* **638,** 86–92. https://www.nature.com/articles/s41586-024-08353-5 (2025).

29. Schuckert, A. *et al.* Observation of a finite-energy phase transition in a one-dimensional quantum simulator. *Nature Physics* **21,** 374–379 (2025).

30. Sompet, P. *et al.* Realizing the symmetry-protected Haldane phase in Fermi–Hubbard ladders. *Nature* **606,** 484–488 (2022).

31. Haghshenas, R. *et al. Digital quantum magnetism at the frontier of classical simulations* 2025. arXiv: 2503.20870 [quant-ph]. https://arxiv.org/abs/2503.20870.

32. Evered, S. J. *et al. Probing topological matter and fermion dynamics on a neutral-atom quantum computer* 2025. arXiv: 2501.18554 [quant-ph]. https://arxiv.org/abs/2501.18554.

33. Whitlow, J. *et al.* Quantum simulation of conical intersections using trapped ions. *Nature Chemistry* **15,** 1509–1514. https://www.nature.com/articles/s41557-023-01303-0 (2023).

34. Dobrautz, W. *et al. Ab Initio Transcorrelated Method enabling accurate Quantum Chemistry on near-term Quantum Hardware* 2024. arXiv: 2303.02007 [quant-ph]. https://arxiv.org/abs/2303.02007.

35. Luo, M. & Cirac, J. I. Efficient Simulation of Quantum Chemistry Problems in an Enlarged Basis Set. *PRX Quantum* **6,** 010355. https://link.aps.org/doi/10.1103/PRXQuantum.6.010355 (1 Mar. 2025).

36. Semeghini, G. *et al.* Probing topological spin liquids on a programmable quantum simulator. *Science* **374,** 1242–1247. eprint: https://www.science.org/doi/pdf/10.1126/science.abi8794. https://www.science.org/doi/abs/10.1126/science.abi8794 (2021).

37. Yoshioka, N., Okubo, T., Suzuki, Y., Koizumi, Y. & Mizukami, W. Hunting for quantum-classical crossover in condensed matter problems. *npj Quantum Information* **10,** 45 (2024).

38. Di Meglio, A. *et al.* Quantum Computing for High-Energy Physics: State of the Art and Challenges. *PRX Quantum* **5,** 037001. https://link.aps.org/doi/10.1103/PRXQuantum.5.037001 (3 Aug. 2024).

39. Bennewitz, E. R. *et al.* Simulating Meson Scattering on Spin Quantum Simulators. *Quantum* **9,** 1773. ISSN: 2521-327X. https://doi.org/10.22331/q-2025-06-17-1773 (June 2025).

40. Beckman, D., Chari, A. N., Devabhaktuni, S. & Preskill, J. Efficient networks for quantum factoring. *Phys. Rev. A* **54,** 1034–1063. https://link.aps.org/doi/10.1103/PhysRevA.54.1034 (2 Aug. 1996).

41. Gidney, C. *How to factor 2048 bit RSA integers with less than a million noisy qubits* 2025. arXiv: 2505.15917 [quant-ph]. https://arxiv.org/abs/2505.15917.

42. Zhou, H. *et al. Resource Analysis of Low-Overhead Transversal Architectures for Reconfigurable Atom Arrays* arXiv:2505.15907 [quant-ph]. May 2025. http://arxiv.org/abs/2505.15907 (2025).

43. Meth, M. *et al.* Simulating two-dimensional lattice gauge theories on a qudit quantum computer. *Nature Phys.* ISSN: 1745-2481. https://doi.org/10.1038/s41567-025-02797-w (2025).

44. DeCross, M. *et al.* Computational Power of Random Quantum Circuits in Arbitrary Geometries. *Physical Review X* **15.** Publisher: American Physical Society, 021052. https://link.aps.org/doi/10.1103/PhysRevX.15.021052 (2025) (May 2025).

45. Kielpinski, D., Monroe, C. & Wineland, D. J. Architecture for a large-scale ion-trap quantum computer. *Nature* **417,** 709–711. ISSN: 00280836 (6890 June 2002).

46. Awschalom, D. *et al.* Development of Quantum Interconnects (QuICs) for Next-Generation Information Technologies. *PRX Quantum* **2,** 017002. https://link.aps.org/doi/10.1103/PRXQuantum.2.017002 (1 Feb. 2021).

47. Żukowski, M., Zeilinger, A., Horne, M. A. & Ekert, A. K. "Event-ready-detectors" Bell experiment via entanglement swapping. *Phys. Rev. Lett.* **71,** 4287–4290. https://link.aps.org/doi/10.1103/PhysRevLett.71.4287 (26 Dec. 1993).

48. Barrett, S. D. & Kok, P. Efficient high-fidelity quantum computation using matter qubits and linear optics. en. *Phys. Rev. A* **71,** 060310. ISSN: 1050-2947, 1094-1622. https://link.aps.org/doi/10.1103/PhysRevA.71.060310 (2024) (June 2005).

49. Moehring, D. L. *et al.* Quantum networking with photons and trapped atoms (Invited). en. *J. Opt. Soc. Am. B* **24,** 300. ISSN: 0740-3224, 1520-8540. https://opg.optica.org/abstract.cfm?URI=josab-24-2-300 (2024) (Feb. 2007).

50. Duan, L.-M. & Monroe, C. Colloquium: Quantum networks with trapped ions. *Rev. Mod. Phys.* **82,** 1209–1224. https://link.aps.org/doi/10.1103/RevModPhys.82.1209 (2 Apr. 2010).

51. Moehring, D. L. *et al.* Entanglement of single-atom quantum bits at a distance. *Nature* **449,** 68–71. ISSN: 1476-4687. https://doi.org/10.1038/nature06118 (Sept. 2007).

52. Hucul, D. *et al.* Modular entanglement of atomic qubits using photons and phonons. *Nature Physics* **11,** 37–42. ISSN: 17452481 (1 2015).

53. Stephenson, L. J. *et al.* High-Rate, High-Fidelity Entanglement of Qubits Across an Elementary Quantum Network. *Phys. Rev. Lett.* **124,** 110501. https://link.aps.org/doi/10.1103/PhysRevLett.124.110501 (11 Mar. 2020).

54. Osman, A. *et al.* Mitigation of frequency collisions in superconducting quantum processors. *Phys. Rev. Res.* **5,** 043001. https://link.aps.org/doi/10.1103/PhysRevResearch.5.043001 (4 Oct. 2023).

55. Kennedy, O. W., Crawford, K. G., Shahbazi, K. & Shelly, C. D. *Analysis of Josephson Junction Barrier Variation – a Combined STEM, Breakdown and Monte-Carlo Approach* 2025. arXiv: 2502.13072 [quant-ph]. https://arxiv.org/abs/2502.13072.

56. Knauer, S., Hadden, J. P. & Rarity, J. G. In-situ measurements of fabrication induced strain in diamond photonic-structures using intrinsic colour centres. *npj Quantum Information* **6,** 50 (2020).

57. Olivero, P. *et al.* Splitting of photo-luminescent emission from nitrogen-vacancy centers in diamond induced by ion-damage-induced stress. *New Journal of Physics* **15,** 043027 (2013).

58. Dalton, J. *A New System of Chemical Philosophy* Part I (Manchester, 1808).

59. Thomson, J. J. XL. Cathode Rays. *Philosophical Magazine (Series 5). 5* **44,** 293–316. https://doi.org/10.1080/14786449708621070 (1897).

60. Rutherford, E. The scattering of α and β particles by matter and the structure of the atom. *Philosophical Magazine (Series 6). 6* **21,** 669–688. https://doi.org/10.1080/14786440508637080 (1911).

61. Bohr, N. On the Constitution of Atoms and Molecules. *The London, Edinburgh, and Dublin Philosophical Magazine and Journal of Science. 6* **26,** 1–25. https://doi.org/10.1080/14786441308634955 (1913).

62. Planck, M. On the Law of Distribution of Energy in the Normal Spectrum. *Annalen der Physik* **309,** 553–563 (1901).

63. Einstein, A. On a Heuristic Viewpoint Concerning the Production and Transformation of Light. *Annalen der Physik* **322,** 132–148 (1905).

64. De Broglie, L. XXXV. A tentative theory of light quanta. *Philosophical Magazine (Series 6). 6* **47,** 446–458. https://doi.org/10.1080/14786442408634378 (1924).

65. Schrödinger, E. Quantisierung als Eigenwertproblem. *Annalen der Physik* **79,** 361–376 (1926).

66. Heisenberg, W. Über quantentheoretische Umdeutung kinematischer und mechanischer Beziehungen. *Zeitschrift für Physik* **33,** 879–893. https://doi.org/10.1007/BF01328377 (Dec. 1925).

67. Gaillard, M. K., Grannis, P. D. & Sciulli, F. J. The standard model of particle physics. *Rev. Mod. Phys.* **71,** S96–S111. https://link.aps.org/doi/10.1103/RevModPhys.71.S96 (2 Mar. 1999).

68. Politzer, H. D. Reliable Perturbative Results for Strong Interactions? *Physical Review Letters* **30,** 1346–1349 (1973).

69. Weinberg, S. A Model of Leptons. *Physical Review Letters* **19,** 1264–1266 (1967).

70. Glashow, S. L. Partial-Symmetries of Weak Interactions. *Nuclear Physics* **22,** 579–588 (1961).

71. Feynman, R. P. *Quantum Electrodynamics* Reprinted by Westview Press, 1998 (W. A. Benjamin, 1961).

72. Paul, W. Electromagnetic traps for charged and neutral particles. *Angewandte Chemie International Edition* **29,** 739–748. https://doi.org/10.1002/anie.199007391 (1990).

73. Ashkin, A. Optical Trapping and Manipulation of Neutral Particles Using Lasers. *Proceedings of the National Academy of Sciences* **94,** 4853–4860 (1997).

74. Chu, S., Bjorkholm, J. E., Ashkin, A. & Cable, A. Experimental Observation of Optically Trapped Atoms. *Physical Review Letters* **57,** 314–317 (1986).

75. Wineland, D. J. & Itano, W. M. Laser cooling of atoms. *Phys. Rev. A* **20,** 1521–1540. https://link.aps.org/doi/10.1103/PhysRevA.20.1521 (4 Oct. 1979).

76. Phillips, W. D. Laser Cooling and Trapping of Neutral Atoms. *Reviews of Modern Physics* **70,** 721–741 (1998).

77. Hänsch, T. W. & Schawlow, A. L. Cooling of gases by laser radiation. *Optics Communications* **13,** 68–69 (1975).

78. Smith, M. C., Leu, A. D., Miyanishi, K., Gely, M. F. & Lucas, D. M. Single-Qubit Gates with Errors at the 10^{-7} Level. *Phys. Rev. Lett.* **134,** 230601. https://link.aps.org/doi/10.1103/42w2-6ccy (23 June 2025).

79. Sotirova, A. S. *et al. High-fidelity heralded quantum state preparation and measurement* 2024. arXiv: 2409.05805 [quant-ph]. https://arxiv.org/abs/2409.05805.

80. Löschnauer, C. M. *et al. Scalable, high-fidelity all-electronic control of trapped-ion qubits* 2024. arXiv: 2407.07694 [quant-ph]. https://arxiv.org/abs/2407.07694.

81. Evered, S. J. *et al.* High-fidelity parallel entangling gates on a neutral-atom quantum computer. *Nature* **622,** 268–272. https://www.nature.com/articles/s41586-023-06481-y (2023).

82. Malinowski, M., Allcock, D. & Ballance, C. How to Wire a 1000-Qubit Trapped-Ion Quantum Computer. *PRX Quantum* **4,** 040313. https://link.aps.org/doi/10.1103/PRXQuantum.4.040313 (4 Oct. 2023).

83. Delaney, R. D. *et al.* Scalable Multispecies Ion Transport in a Grid-Based Surface-Electrode Trap. *Phys. Rev. X* **14,** 041028. https://link.aps.org/doi/10.1103/PhysRevX.14.041028 (4 Nov. 2024).

84. Krutyanskiy, V. *et al.* Entanglement of Trapped-Ion Qubits Separated by 230 Meters. *Phys. Rev. Lett.* **130,** 050803. https://link.aps.org/doi/10.1103/PhysRevLett.130.050803 (5 Feb. 2023).

85. Van Leent, T. *et al.* Entangling single atoms over 33 km telecom fibre. *Nature* **607,** 69–73. ISSN: 1476-4687. https://doi.org/10.1038/s41586-022-04764-4 (July 2022).

86. Wang, P. *et al.* Single ion qubit with estimated coherence time exceeding one hour. *Nature Comm.* **12,** 233. ISSN: 2041-1723. https://doi.org/10.1038/s41467-020-20330-w (Jan. 2021).

87. Obšil, P. *et al.* A room-temperature ion trapping apparatus with hydrogen partial pressure below $\$10^{-11}\$$ *mbar*. *Review of Scientific Instruments* **90,** 083201. https://doi.org/10.1063/1.5104346 (Aug. 2019).

88. Christensen, J. E., Hucul, D., Campbell, W. C. & Hudson, E. R. High-fidelity manipulation of a qubit enabled by a manufactured nucleus. *npj Quantum Information* **6.** ISSN: 20566387 (1 Dec. 2020).

89. Kramida, A., Ralchenko, Y. & Team, N. A. *NIST Atomic Spectra Database (version 5.12)* [Online]. Available: https://physics.nist.gov/asd. National Institute of Standards and Technology, Gaithersburg, MD. Accessed: 2025-06-24. 2024.

90. Group, D. T. I. Q. C. *Trapped Ion Periodic Table* Web image adapted and cropped. https://iontrap.duke.edu/resources/ion-periodic-table/ (2025).

91. Kuske, P., Kirchner, N., Wittmann, W., Andrä, H. & Kaiser, D. Lifetime measurements by pulsed laser excitation of fast ion beams. *Physics Letters A* **64,** 377–380. ISSN: 0375-9601. https://www.sciencedirect.com/science/article/pii/0375960178902712 (1978).

92. Arnold, K. J. *et al.* Measurements of the branching ratios for $6P_{1/2}$ decays in $^{138}Ba^{+}$. *Phys. Rev. A* **100,** 032503. https://link.aps.org/doi/10.1103/PhysRevA.100.032503 (3 Sept. 2019).

93. Olmschenk, S. *et al.* Manipulation and detection of a trapped Yb^{+} hyperfine qubit. *Phys. Rev. A* **76,** 052314. https://link.aps.org/doi/10.1103/PhysRevA.76.052314 (5 Nov. 2007).

94. Klein, H. A., Bell, A. S., Barwood, G. P. & Gill, P. Laser cooling of trapped Yb+. en. *Applied Physics B Photophysics and Laser Chemistry* **50,** 13–17. ISSN: 0721-7269, 1432-0649. http://link.springer.com/10.1007/BF00330086 (2025) (Jan. 1990).

95. Bell, A. S. *et al.* Laser cooling of trapped ytterbium ions using a four-level optical-excitation scheme. en. *Physical Review A* **44,** R20–R23. ISSN: 1050-2947, 1094-1622. https://link.aps.org/doi/10.1103/PhysRevA.44.R20 (2025) (July 1991).

96. Yu, N. & Maleki, L. Lifetime measurements of the $4f^{14}5d$ metastable states in single ytterbium ions. *Phys. Rev. A* **61,** 022507. https://link.aps.org/doi/10.1103/PhysRevA.61.022507 (2 Jan. 2000).

97. Olmschenk, S. *et al.* Measurement of the lifetime of the $6p\ ^2P^o_{1/2}$ level of Yb^{+}. *Phys. Rev. A* **80,** 022502. https://link.aps.org/doi/10.1103/PhysRevA.80.022502 (2 Aug. 2009).

98. Low, P. J., White, B. & Senko, C. Control and Readout of a 13-level Trapped Ion Qudit. arXiv: 2306.03340 [quant-ph]. https://arxiv.org/abs/2306.03340 (2023).

99. Ruster, T. *et al.* A long-lived Zeeman trapped-ion qubit. *Applied Physics B: Lasers and Optics* **122.** ISSN: 09462171 (10 Oct. 2016).

100. Wang, Y., Hu, Z., Sanders, B. C. & Kais, S. Qudits and High-Dimensional Quantum Computing. *Frontiers in Physics* **8.** ISSN: 2296-424X. https://www.frontiersin.org/articles/10.3389/fphy.2020.589504 (2020).

101. Yum, D., Munshi, D. D., Dutta, T. & Mukherjee, M. Optical barium ion qubit. *J. Opt. Soc. Am. B* **34,** 1632–1636. https://opg.optica.org/josab/abstract.cfm?URI=josab-34-8-1632 (Aug. 2017).

102. Allcock, D. T. C. *et al.* omg Blueprint for trapped ion quantum computing with metastable states. *Applied Physics Letters* **119,** 1–6 (214002 2021).

103. Ralph, T. C., Langford, N. K., Bell, T. B. & Munro, W. J. Linear optical controlled-NOT gate in the single-rail photonic scheme. *Physical Review A* **65,** 012314 (2002).

104. Knill, E., Laflamme, R. & Milburn, G. J. A scheme for efficient quantum computation with linear optics. *Nature* **409,** 46–52 (2001).

105. Los, J. W. N. *et al.* High-performance photon number resolving detectors for 850–950 nm wavelength range. *APL Photonics* **9,** 066101. ISSN: 2378-0967. https://doi.org/10.1063/5.0204340 (2025) (June 2024).

106. Leong, W. S., Xin, M., Huang, C., Chen, Z. & Lan, S.-Y. Long light storage time in an optical fiber. *Physical Review Research* **2.** Publisher: American Physical Society, 033320. https://link.aps.org/doi/10.1103/PhysRevResearch.2.033320 (2025) (Aug. 2020).

107. Phillips, D. F., Fleischhauer, A., Mair, A., Walsworth, R. L. & Lukin, M. D. Storage of Light in Atomic Vapor. *Physical Review Letters* **86.** Publisher: American Physical Society, 783–786. https://link.aps.org/doi/10.1103/PhysRevLett.86.783 (2025) (Jan. 2001).

108. Knaut, C. M. *et al.* Entanglement of nanophotonic quantum memory nodes in a telecom network. *Nature* **629,** 573–578. https://doi.org/10.1038/s41586-024-07252-z (May 2024).

109. Yin, J. *et al.* Quantum teleportation and entanglement distribution over 100-kilometre free-space channels. en. *Nature* **488.** Publisher: Nature Publishing Group, 185–188. ISSN: 1476-4687. https://www.nature.com/articles/nature11332 (2025) (Aug. 2012).

110. Storz, S. *et al.* Loophole-free Bell inequality violation with superconducting circuits. en. *Nature* **617.** Publisher: Nature Publishing Group, 265–270. ISSN: 1476-4687. https://www.nature.com/articles/s41586-023-05885-0 (2025) (May 2023).

111. Bennett, C. H. & Brassard, G. Quantum cryptography: Public key distribution and coin tossing. *Theoretical Computer Science. Theoretical Aspects of Quantum Cryptography – celebrating 30 years of BB84* **560,** 7–11. ISSN: 0304-3975. https://www.sciencedirect.com/science/article/pii/S0304397514004241 (2025) (Dec. 2014).

112. Lukens, J. M. & Lougovski, P. Frequency-encoded photonic qubits for scalable quantum information processing. EN. *Optica* **4.** Publisher: Optica Publishing Group, 8–16. ISSN: 2334-2536. https://opg.optica.org/optica/abstract.cfm?uri=optica-4-1-8 (2025) (Jan. 2017).

113. Erhard, M., Krenn, M. & Zeilinger, A. Advances in high-dimensional quantum entanglement. *Nature Reviews Physics* **2,** 365–381. https://www.nature.com/articles/s42254-020-0193-5 (2020).

114. Marcikic, I. *et al.* Distribution of Time-Bin Entangled Qubits over 50 km of Optical Fiber. *Physical Review Letters* **93.** Publisher: American Physical Society, 180502. https://link.aps.org/doi/10.1103/PhysRevLett.93.180502 (2025) (Oct. 2004).

115. Barredo, D., de Léséleuc, S., Lienhard, V., Lahaye, T. & Browaeys, A. An atom-by-atom assembler of defect-free arbitrary two-dimensional atomic arrays. *Science* **354,** 1021–1023. eprint: https://www.science.org/doi/pdf/10.1126/science.aah3778. https://www.science.org/doi/abs/10.1126/science.aah3778 (2016).

116. Endres, M. *et al.* Atom-by-atom assembly of defect-free one-dimensional cold atom arrays. *Science* **354,** 1024–1027. eprint: https://www.science.org/doi/pdf/10.1126/science.aah3752. https://www.science.org/doi/abs/10.1126/science.aah3752 (2016).

117. Schlosser, N., Reymond, G., Protsenko, I. & Grangier, P. Sub-Poissonian loading of single atoms in a microscopic dipole trap. *Nature* **411,** 1024–1027 (2001).

118. Earnshaw, S. On the Nature of the Molecular Forces which Regulate the Constitution of the Luminiferous Ether. *Transactions of the Cambridge Philosophical Society* **7,** 97 (Jan. 1848).

119. Paul, W. & Steinwedel, H. *Zeitschrift für Naturforschung A* **8,** 448–450. https://doi.org/10.1515/zna-1953-0710 (1953).

120. Paul, W. Electromagnetic Traps for Charged and Neutral Particles (Nobel Lecture). *Angewandte Chemie International Edition in English* **29,** 739–748. eprint: https://onlinelibrary.wiley.com/doi/pdf/10.1002/anie.199007391. https://onlinelibrary.wiley.com/doi/abs/10.1002/anie.199007391 (1990).

121. Leibfried, D., Blatt, R., Monroe, C. & Wineland, D. Quantum dynamics of single trapped ions. *Rev. Mod. Phys.* **75,** 281–324. https://link.aps.org/doi/10.1103/RevModPhys.75.281 (1 Mar. 2003).

122. March, R. E. Quadrupole ion traps. *Mass Spectrometry Reviews* **28,** 961–989. eprint: https://analyticalsciencejournals.onlinelibrary.wiley.com/doi/pdf/10.1002/mas.20250. https://analyticalsciencejournals.onlinelibrary.wiley.com/doi/abs/10.1002/mas.20250 (2009).

123. Malinowski, M. *Ion traps you never knew existed* Blog post, *Reading the quantum*. Feb. 2022. https://m-malinowski.github.io/2022/02/21/all-kinds-of-ion-traps.html.

124. Leibfried, D., Blatt, R., Monroe, C. & Wineland, D. Quantum dynamics of single trapped ions. en. *Reviews of Modern Physics* **75,** 281–324. ISSN: 0034-6861, 1539-0756. https://link.aps.org/doi/10.1103/RevModPhys.75.281 (2024) (Mar. 2003).

125. Berkeland, D. J., Miller, J. D., Bergquist, J. C., Itano, W. M. & Wineland, D. J. Minimization of ion micromotion in a Paul trap. *Journal of Applied Physics* **83,** 5025–5033. ISSN: 0021-8979. https://doi.org/10.1063/1.367318 (May 1998).

126. Sorensen, A. & Molmer, K. Entanglement and quantum computation with ions in thermal motion. *Phys. Rev. A* **62** (022311 2000).

127. Matsos, V. G. *et al.* Robust and Deterministic Preparation of Bosonic Logical States in a Trapped Ion. *Phys. Rev. Lett.* **133,** 050602. https://link.aps.org/doi/10.1103/PhysRevLett.133.050602 (5 July 2024).

128. Sturges, T. J. *et al.* Quantum simulations with multiphoton Fock states. *NPJ Quantum Information* **7,** 91 (2021).

129. Deslauriers, L. *et al.* Scaling and Suppression of Anomalous Heating in Ion Traps. en. *Physical Review Letters* **97,** 103007. ISSN: 0031-9007, 1079-7114. https://link.aps.org/doi/10.1103/PhysRevLett.97.103007 (2025) (Sept. 2006).

130. Turchette, Q. A. *et al.* Heating of trapped ions from the quantum ground state. *Phys. Rev. A* **61,** 063418. https://link.aps.org/doi/10.1103/PhysRevA.61.063418 (6 May 2000).

131. Brown, K. R. *et al.* Materials challenges for trapped-ion quantum computers. *Nature Reviews Materials* **6,** 892–905 (2021).

132. Brownnutt, M., Kumph, M., Rabl, P. & Blatt, R. Ion-trap measurements of electric-field noise near surfaces. *Rev. Mod. Phys.* **87,** 1419–1482. https://link.aps.org/doi/10.1103/RevModPhys.87.1419 (4 Dec. 2015).

133. Labaziewicz, J. *et al.* Suppression of Heating Rates in Cryogenic Surface-Electrode Ion Traps. *Phys. Rev. Lett.* **100,** 013001. https://link.aps.org/doi/10.1103/PhysRevLett.100.013001 (1 Jan. 2008).

134. Lin, K.-Y., Low, G. H. & Chuang, I. L. Effects of electrode surface roughness on motional heating of trapped ions. *Phys. Rev. A* **94,** 013418. https://link.aps.org/doi/10.1103/PhysRevA.94.013418 (1 July 2016).

135. Wineland, D. *et al.* Experimental Issues in Coherent Quantum-State Manipulation of Trapped Atomic Ions. *Journal of Research of the National Institute of Standards and Technology* **103** (1998).

136. Rei§, D., Lindner, A. & Blatt, R. Cooling of trapped multilevel ions: A numerical analysis. *Phys. Rev. A* **54,** 5133–5140. https://link.aps.org/doi/10.1103/PhysRevA.54.5133 (6 Dec. 1996).

137. Ludlow, A. D., Boyd, M. M., Ye, J., Peik, E. & Schmidt, P. O. Optical atomic clocks. *Rev. Mod. Phys.* **87,** 637–701. https://link.aps.org/doi/10.1103/RevModPhys.87.637 (2 June 2015).

138. Matsubara, K. *et al.* Direct comparison of a Caˆ+ single-ion clock against a Sr lattice clock to verify the absolute frequency measurement. *Optics Express* **20,** 22034–22041 (2012).

139. Leupold, F. M. *Bang-bang Control of a Trapped-Ion Oscillator* DISS. ETH NO. 22892. Doctoral Thesis (ETH Zürich, Zurich, Switzerland, 2016). https://ethz.ch/content/dam/ethz/special-interest/phys/quantum-electronics/tiqi-dam/documents/phd_theses/thesis_florian_leupold_20160405.pdf.

140. James, D. Quantum dynamics of cold trapped ions with application to quantum computation. *Appl. Phys. B* **66,** 181–190 (1998).

141. Chanu, S. R. *et al.* Magic wavelength of the $^{138}Ba^{+}$ $6s\ ^2S_{1/2} - -5d\ ^2D_{5/2}$ clock transition. *Phys. Rev. A* **101,** 042507. https://link.aps.org/doi/10.1103/PhysRevA.101.042507 (4 Apr. 2020).

142. Chen, Z.-Y. *et al. Non-invasive mid-circuit measurement and reset on atomic qubits* 2025. arXiv: 2504.12538 [quant-ph]. https://arxiv.org/abs/2504.12538.

143. O'Reilly, J. *New Techniques for Fast and High-Fidelity Trapped Ion Photonic Interconnects* Advisor: Christopher Monroe. Doctoral Dissertation (Duke University, Durham, North Carolina, USA, 2024). https://duke.app.box.com/s/f38wa1pf8ukgn0bnxuztmdbddbve5j0t.

144. Monroe, C. & Kim, J. ' ion trap quantum processor. *Science* **339,** 1164–1169. ISSN: 10959203 (6124 2013).

145. Hong, C. K., Ou, Z. Y. & Mandel, L. Measurement of subpicosecond time intervals between two photons by interference. *Phys. Rev. Lett.* **59,** 2044–2046. https://link.aps.org/doi/10.1103/PhysRevLett.59.2044 (18 Nov. 1987).

146. Crocker, C. *et al.* High Purity Single Photons Entangled with an Atomic Memory. *Optics Express* **27,** 28143–28149. http://arxiv.org/abs/1812.01749 (20 2019).

147. Stephenson, L. J. *Entanglement between nodes of a quantum network* en. PhD thesis ().

148. Carter, A. L. *et al.* Ion trap with in-vacuum high numerical aperture imaging for a dual-species modular quantum computer. *Rev. Sci. Instrum.* **95,** 033201. ISSN: 0034-6748. https://doi.org/10.1063/5.0180732 (Mar. 2024).

149. O'Reilly, J. *New Techniques for Fast and High-Fidelity Trapped Ion Photonic Interconnects* en. PhD thesis (2024).

150. Steffen, A. *et al.* Note: *In situ* measurement of vacuum window birefringence by atomic spectroscopy. en. *Review of Scientific Instruments* **84.** Publisher: AIP Publishing. ISSN: 0034-6748, 1089-7623. https://pubs.aip.org/rsi/article/84/12/126103/355390/Note-In-situ-measurement-of-vacuum-window (2025) (Dec. 2013).

151. Li, S. *et al.* Metasurface Polarization Optics: Phase Manipulation for Arbitrary Polarization Conversion Condition. *Phys. Rev. Lett.* **134,** 023803. https://link.aps.org/doi/10.1103/PhysRevLett.134.023803 (2 Jan. 2025).

152. Brakhane, S. *et al.* Note: Ultra-low birefringence dodecagonal vacuum glass cell. *Review of Scientific Instruments* **86,** 126108 (2015).

153. Van Leent, T. *et al.* Entangling single atoms over 33 km telecom fibre. *Nature* **607,** 69–73 (July 2022).

154. Saha, S. *et al.* High-fidelity remote entanglement of trapped atoms mediated by time-bin photons. *Nature Communications* **16,** 2533. ISSN: 2041-1723. https://doi.org/10.1038/s41467-025-57557-4 (2025).

155. Yu, Y. *et al.* Entanglement fidelity limits of photonically-networked atomic qubits due to recoil and timing. *in preparation* (2024).

156. Bernien, H. *et al.* Heralded entanglement between solid-state qubits separated by three metres. *Nature* **497,** 86–90. ISSN: 1476-4687. https://doi.org/10.1038/nature12016 (May 2013).

157. Bhaskar, M. K. *et al.* Experimental Demonstration of Memory-Enhanced Quantum Communication. *Nature* **580,** 60–64. https://www.nature.com/articles/s41586-020-2103-5 (2020).

158. Apolín, J. & Nadlinger, D. P. *Recoil-induced errors and their correction in photon-mediated entanglement between atom qubits* 2025. arXiv: 2503.16837 [quant-ph]. https://arxiv.org/abs/2503.16837.

159. Dietrich, M. R., Kurz, N., Noel, T., Shu, G. & Blinov, B. B. Hyperfine and optical barium ion qubits. *Phys. Rev. A.* ISSN: 10502947 (2010).

160. Dietrich, M. R., Kurz, N., Noel, T., Shu, G. & Blinov, B. B. Hyperfine and optical barium ion qubits. *Phys. Rev. A* **81,** 052328. https://link.aps.org/doi/10.1103/PhysRevA.81.052328 (5 May 2010).

161. Arnold, K. J. *et al.* Measurements of the branching ratios for $6P_{1/2}$ decays in $^{138}Ba^{+}$. *Phys. Rev. A* **100,** 032503. https://link.aps.org/doi/10.1103/PhysRevA.100.032503 (3 Sept. 2019).

162. Glauber, R. J. Coherent and Incoherent States of the Radiation Field. *Phys. Rev.* **131,** 2766–2788. https://link.aps.org/doi/10.1103/PhysRev.131.2766 (6 Sept. 1963).

163. Monroe, C., Meekhof, D. M., King, B. E. & Wineland, D. J. A "Schrödinger Cat" Superposition State of an Atom. *Science* **272,** 1131–1136. eprint: https://www.science.org/doi/pdf/10.1126/science.272.5265.1131. https://www.science.org/doi/abs/10.1126/science.272.5265.1131 (1996).

164. Ritter, S. *et al.* An elementary quantum network of single atoms in optical cavities. *Nature* **484,** 195–200. ISSN: 00280836 (7393 2012).

165. Covey, J. P., Weinfurter, H. & Bernien, H. Quantum networks with neutral atom processing nodes. *npj Quantum Information* **9,** 90. ISSN: 2056-6387. https://doi.org/10.1038/s41534-023-00759-9 (Sept. 2023).

166. Sackett, C. A. *et al.* Experimental entanglement of four particles. *Nature* **404,** 256–259. ISSN: 00280836 (6775 2000).

167. Chwalla, M. *et al.* Precision spectroscopy with two correlated atoms. *Applied Physics B* **89,** 483–488. ISSN: 1432-0649. https://doi.org/10.1007/s00340-007-2867-4 (2007).

168. Kim, T., Maunz, P. & Kim, J. Efficient collection of single photons emitted from a trapped ion into a single-mode fiber for scalable quantum-information processing. *Phys. Rev. A* **84,** 063423. https://link.aps.org/doi/10.1103/PhysRevA.84.063423 (6 Dec. 2011).

169. Wu, Y., Kolkowitz, S., Puri, S. & Thompson, J. D. Erasure conversion for fault-tolerant quantum computing in alkaline earth Rydberg atom arrays. *Nature Comm.* **13,** 4657. ISSN: 2041-1723. https://doi.org/10.1038/s41467-022-32094-6 (Aug. 2022).

170. Bersin, E. *et al.* Development of a Boston-area 50-km fiber quantum network testbed. *Phys. Rev. Appl.* **21,** 014024. https://link.aps.org/doi/10.1103/PhysRevApplied.21.014024 (1 Jan. 2024).

171. Ramette, J., Sinclair, J., Breuckmann, N. P. & Vuletić, V. Fault-tolerant connection of error-corrected qubits with noisy links. *npj Quantum Information*

10, 58. ISSN: 2056-6387. https://doi.org/10.1038/s41534-024-00855-4 (June 2024).

172. Low, P. J., White, B. M., Cox, A. A., Day, M. L. & Senko, C. Practical trapped-ion protocols for universal qudit-based quantum computing. *Phys. Rev. Res.* **2,** 033128. https://link.aps.org/doi/10.1103/PhysRevResearch.2.033128 (3 July 2020).

173. Islam, N. T., Lim, C. C. W., Cahall, C., Kim, J. & Gauthier, D. J. Provably secure and high-rate quantum key distribution with time-bin qudits. *Science Advances* **3,** e1701491. https://www.science.org/doi/abs/10.1126/sciadv.1701491 (2017).

174. Sun, K. *et al.* Quantum Simulation of Polarized Light-Induced Electron Transfer with a Trapped-Ion Qutrit System. *J. Phys. Chem. Lett.* **14,** 6071–6077. https://doi.org/10.1021/acs.jpclett.3c01166 (2023).

175. Shalaev, M. *et al.* Photonic Networking of Quantum Memories in High-Dimensions. en.

176. Main, D. *et al.* Distributed quantum computing across an optical network link. *Nature* **638,** 383–388. https://doi.org/10.1038/s41586-024-08404-x (2025).

177. Chi, Y. *et al.* A programmable qudit-based quantum processor. *Nature Communications* **13.** https://doi.org/10.1038/s41467-022-28767-x (2022).

178. Ringbauer, M. *et al.* A universal qudit quantum processor with trapped ions. *Nature Phys.* **18,** 1053–1059. ISSN: 1745-2473. https://www.nature.com/articles/s41567-022-01658-0 (2022).

179. Hrmo, P. *et al.* Native qudit entanglement in a trapped ion quantum processor. *Nature Communications* **14,** 2242. ISSN: 2041-1723. https://doi.org/10.1038/s41467-023-37375-2 (2023).

180. Yamazaki, T. & Azuma, K. Linear-optical fusion boosted by high-dimensional entanglement. *arXiv:2407.10893.* https://arxiv.org/abs/2407.10893 (2024).

181. Cerf, N. J., Bourennane, M., Karlsson, A. & Gisin, N. Security of quantum key distribution using d-level systems. *Phys. Rev. Letters* **88,** 127902 (2002).

182. Bacco, D. *et al.* Practical high-dimensional quantum key distribution protocol over deployed multicore fiber. *Nature Communications* **15,** 45876 (2024).

183. Morvan, A. *et al.* Qutrit Randomized Benchmarking. *Phys. Rev. Lett.* **126,** 210504. https://link.aps.org/doi/10.1103/PhysRevLett.126.210504 (21 May 2021).

184. Blok, M. S. *et al.* Quantum Information Scrambling on a Superconducting Qutrit Processor. *Phys. Rev. X* **11,** 021010. https://link.aps.org/doi/10.1103/PhysRevX.11.021010 (2 Apr. 2021).

185. Mirhosseini, M., Sipahigil, A., Kalaee, M. & Painter, O. Superconducting qubit to optical photon transduction. *Nature* **588,** 599–603. ISSN: 1476-4687. https://doi.org/10.1038/s41586-020-3038-6 (2020).

186. Krastanov, S. *et al.* Optically Heralded Entanglement of Superconducting Systems in Quantum Networks. *Phys. Rev. Lett.* **127,** 040503. https://link.aps.org/doi/10.1103/PhysRevLett.127.040503 (4 July 2021).

187. Zhang, W. *et al.* Experimental realization of entanglement in multiple degrees of freedom between two quantum memories. *Nature Communications* **7,** 13514. https://doi.org/10.1038/ncomms13514 (2016).

188. Krenn, M. *et al.* Generation and confirmation of a (100 x 100)-dimensional entangled quantum system. *Proc. Nat. Acad. Sci.* **111,** 6243–6247. https://www.pnas.org/content/111/17/6243 (2014).

189. Yu, Y. *et al.* Entanglement fidelity limits of photonically-networked atomic qubits from recoil and timing. *arXiv: 2503.19818.* https://arxiv.org/abs/2503.19818 (2025).

190. Kikura, S., Inoue, R., Yamasaki, H., Goban, A. & Sunami, S. Taming Recoil Effect in Cavity-Assisted Quantum Interconnects. *arXiv: 2502.14859.* eprint: 2502.14859. https://arxiv.org/abs/2502.14859 (2025).

191. Audenaert, K. M. R. & Plenio, M. B. When are correlations quantum?—verification and quantification of entanglement by simple measurements. *New Journal of Physics* **8,** 266. https://dx.doi.org/10.1088/1367-2630/8/11/266 (Nov. 2006).

192. Calsamiglia, J. & Lütkenhaus, N. Maximum efficiency of a linear-optical Bell-state analyzer. *Applied Physics B-Lasers and Optics* **72,** 67–71. ISSN: 0946-2171. %3CGo%20to%20ISI%3E://WOS:000166251400009 (2001).

193. Ghosh, S., Kar, G., Roy, A., Sen(De), A. & Sen, U. Distinguishability of Bell States. *Phys. Rev. Lett.* **87,** 277902. https://link.aps.org/doi/10.1103/PhysRevLett.87.277902 (27 Dec. 2001).

194. Bayerbach, M. J., D'Aurelio, S. E., van Loock, P. & Barz, S. Bell-state measurement exceeding 50% success probability with linear optics. *Science Advances* **9,** eadf4080. https://www.science.org/doi/abs/10.1126/sciadv.adf4080 (2023).

195. Grice, W. P. Arbitrarily complete Bell-state measurement using only linear optical elements. *Phys. Rev. A* **84,** 042331. https://link.aps.org/doi/10.1103/PhysRevA.84.042331 (4 Oct. 2011).

196. Kwiat, P. G. & Weinfurter, H. Embedded Bell-state analysis. *Phys. Rev. A* **58,** R2623–R2626 (1998).

197. Schuck, C., Huber, G., Kurtsiefer, C. & Weinfurter, H. Complete Deterministic Linear Optics Bell State Analysis. *Phys. Rev. Lett.* **96,** 190501. https://link.aps.org/doi/10.1103/PhysRevLett.96.190501 (19 May 2006).

198. Barbieri, M., De Martini, F., Mataloni, P., Vallone, G. & Cabello, A. Enhancing the Violation of the Einstein-Podolsky-Rosen Local Realism by Quantum Hyperentanglement. *Phys. Rev. Lett.* **97,** 140407. https://link.aps.org/doi/10.1103/PhysRevLett.97.140407 (14 Oct. 2006).

199. Li, L. *et al.* Parallelized telecom quantum networking with a ytterbium-171 atom array. *arXiv: 2502.17406.* https://arxiv.org/abs/2502.17406 (2025).

200. Aghaee Rad, H. *et al.* Scaling and networking a modular photonic quantum computer. *Nature* **638,** 912–919. ISSN: 1476-4687. https://doi.org/10.1038/s41586-024-08406-9 (2025).

201. Bartolucci, S. *et al.* Fusion-based quantum computation. *Nature Communications* **14.** https://www.nature.com/articles/s41467-023-36493-1 (2023).

202. Erhard, M., Malik, M., Krenn, M. & Zeilinger, A. Experimental Greenberger–Horne–Zeilinger entanglement beyond qubits. *Nature Photonics* **12,** 759–764. https://www.nature.com/articles/s41566-018-0257-6 (2018).

203. Cirac, J. I., Zoller, P., Kimble, H. J. & Mabuchi, H. Quantum State Transfer and Entanglement Distribution among Distant Nodes in a Quantum Network.

Phys. Rev. Lett. **78,** 3221–3224. https://link.aps.org/doi/10.1103/PhysRevLett.78.3221 (16 Apr. 1997).

204. Wilk, T., Webster, S. C., Kuhn, A. & Rempe, G. Single-Atom Single-Photon Quantum Interface. *Science* **317,** 488–490. https://www.science.org/doi/abs/10.1126/science.1143835 (2007).

205. Kurz, C. *et al.* Experimental protocol for high-fidelity heralded photon-to-atom quantum state transfer. *Nature Communications* **5,** 5527. ISSN: 2041-1723. https://www.nature.com/articles/ncomms6527.pdf (2014).